UNIVERSITY OF CALGARY

Nonstationary wavelet simulation and estimation

by

Linping Dong

A THESIS
SUBMITTED TO THE FACULTY OF GRADUATE STUDIES
IN PARTIAL FULFILMENT OF THE REQUIREMENTS FOR THE
DEGREE OF MASTER OF SCIENCE

DEPARTMENT OF GEOLOGY AND GEOPHYSICS

CALGARY, ALBERTA

APRIL, 2004

ABSTRACT

Nonstationary wavelet simulation and estimation methods are closely related to nonstationary seismic modeling and nonstationary deconvolution. Conventional wavelet estimation and deconvolution do not deal with the nonstationarity of the wavelet. This thesis begins with an investigation of the methods for nonstationary wavelet simulation that can be used to generate realistic synthetic seismograms. Then this thesis examines methods of wavelet estimation using 1-D attenuated synthetic data and real data. These estimation approaches are the basis for Wiener deconvolution (time domain), Wiener deconvolution (frequency domain), and Gabor deconvolution. For comparison, the wavelet is also estimated from downgoing waves isolated from a VSP experiment which gives direct recordings of the nonstationary wavelet. Finally, a new approach is provided for evaluating the accuracy of the nonstationary wavelet estimates by the VSP downgoing wavelets. This result shows that the wavelets estimated from Gabor deconvolution are more stable and closer to the wavelet estimates from VSP data than those from multi-window Wiener and frequency-domain spiking deconvolution.

ACKNOWLEDGEMENTS

First, I would like to thank my respectable supervisor, Dr. Gary Margrave, for his guidance and support throughout my work. His patience and encouragement have been and will be a source of inspiration to me. I would also like to thank the sponsors of the CREWES project. Without their financial support, I could not even come to Canada and pursue my advanced study. Special thanks to Dr. Edward Krebes, Mr. Kevin Hall and Mr. Larry Mewhort for sharing their knowledge with me. Many thanks also to my fellow students.

Finally, I am very grateful to Guofeng Lu, my wife, who has been a mother and a father to our daughter during my long, study-related absences.

DEDICATION

This thesis is dedicated to my beloved parents.

TABLE OF CONTENTS

LIST OF TABLES

LIST OF FIGURES

CHAPTER 1 INTRODUCTION

1.1 Why revisit wavelet estimation

Currently, demands of amplitude control and accuracy are drastically increasing to face new challenges in classical topics such as wavelet estimation (Tygel and Bleistein, 2000). Amplitude control and accuracy improvement are fundamental requirements for the processes such as AVO attribute extraction, seismic inversion and reservoir characterization. In all cases, we hope the amplitude variation is consistent with real reflectivity. This objective can be reached only after the wavelet embedded in the seismic trace can be accurately estimated. The more accurate the wavelet estimate, the closer the reflectivity estimate is to the real one.

A seismic wavelet whose Fourier spectrum does not change as it propagates is said to be stationary. In all other cases, the wavelet is said to be nonstationary. There are two common assumptions about the wavelet in the deconvolution of seismic data. One is the assumption of minimum phase for impulsive sources and the other one is that of stationarity. The first assumption has been frequently challenged and many alternatives to non-minimum phase wavelet estimation and deconvolution have been suggested (Foster at el., 1997, Porsani and Ursin, 1998). Many authors recognized the second assumption would cause problems in deconvolution and then proposed several different inverse-Q filters to correct wavelet variation caused by attenuation (Hale, 1981; Bickel and Natarajan, 1985; Hargreave and Calvert, 1991, Wang, 2002). Alternatively, the nonstationarity of the wavelet can be addressed in the deconvolution algorithm. Nonstationary deconvolution (Margrave, 1998, Schoepp and Margrave, 1998; Grossman et al., 2002) provides a new approach based on a nonstationary convolution model of the seismic trace. Nonstationary deconvolution, specifically Gabor deconvolution, has been compared with those of the Wiener and inverse-Q filtering and the former shows improved vertical resolution and a better reflectivity character (Margrave el al, 2003). However, the accuracy of the nonstationary wavelet estimate needs further validation. The objective of this thesis is to validate the wavelet estimates from the surface data by the wavelets measured in VSPs based on the fact that both of them are nonstationary.

1.2 Wavelet estimation

In its broadest sense, the wavelet-estimation problem means the determination (and removal) of the effects of the source signature and receiver response from the seismic trace, as well as all undesired propagation effects that are not related to the reflectivity series of the target reflectors. The basic framework is the convolutional model (as described in Sheriff and Geldart, 1982), in which a seismic trace consists of a wavelet convolved with the impulse response (or reflectivity) plus additive noise. If the wavelet is known, the reflectivity can be inverted for. Wavelet estimation approaches are classified into two categories: deterministic and statistical methods.

A deterministic approach may be taken by measuring the source signature when it is effectively free of the earth response. Ziolkowski (1991) suggested a method for the extraction and removal of the source wavelet from the surface seismic recordings by a source-scaling law. However, Ziolkowski's method requires a fundamental change in field technique and does not address nonstationary. A more useful method is to extract wavelets from VSP data. A VSP experiment can actually measure the seismic wavelet at different depths. The deterministic approaches make few assumptions about the wavelet properties. The measured wavelet usually is more realistic than that from the statistical method. The shortcoming of the wavelet estimates from VSP data is that they only represent the wavelet change in a limited zone since we can not drill wells everywhere.

Statistical wavelet estimation has both stationary and nonstationary approaches. The stationary wavelet estimation involves making the assumption that the data are the result of convolving a wavelet (whose shape does not change with propagation) with a random reflectivity. More specifically, the impulse response of the earth is usually assumed to be white, random and stationary (Robinson and Treitel, 1980). Nonstationary wavelet estimation is based on a nonstationary trace model in which the trace is the result of nonstationary convolution between a time-variant wavelet and a random reflectivity. Nonstationary wavelet estimation is the framework for nonstationary deconvolution and also is helpful in AVO analysis and reservoir characterization.

1.3 Nonstationary wavelet models

In this thesis, a seismic wavelet will be called stationary if its Fourier spectrum (both amplitude and phase) does not change as the wavelet propagates. We specifically include constant scaling as a stationary effect. Conversely, a seismic wavelet whose Fourier spectrum changes as it propagates will be called nonstationary. These definitions are based on physical considerations and are appropriate for the deconvolution problem. The stationary wavelet is a convenient model in deconvolution but it is not physically realistic because the real wavelet changes shape continually due to the existence of factors such as noise, source signature inconsistency, reflection/transmission, anelastic attenuation and multiples. Wavefront divergence (geometrical spreading) is a simple frequency-independent scaling of the wavelet and is considered as a stationary effect in this thesis.

1.3.1 Inhomogeneous and homogenous nonstationary wavelet

This theory is adapted from Aki and Richards (1980). Assume that a plane wave $w(\vec{x},t)$ propagates in the direction of increasing $\vec{x}$ and that the wavefront for anelastic media first arrives at position $\vec{x}=0$ at time $t=0$. At $\vec{x}>0$, each Fourier components of $w(\vec{x},t)$ can be factored as

$$\hat{w}(\vec{x},\omega)=\hat{w}(\omega)\exp\left(-i\vec{K}\cdot\vec{x}\right), \tag{1.1}$$

where $\hat{w}(\omega)$ is spectrum of the source signature and $\hat{w}(\vec{x},\omega)$ represents the nonstationary wavelet in the space-frequency domain. $\vec{K}$ is a complex valued wavenumber that can be written as

$$\vec{K} = \vec{P} - i\vec{A}\,, \tag{1.2}$$

with $\vec{P}$ being the *propagation vector* and $\vec{A}$ being the *attenuation vector*. From equation (1.2), we also can derive

$$\left|\vec{K}\right|^2 = \left|\vec{P}\right|^2 - \left|\vec{A}\right|^2 - 2i\left|\vec{P}\right| \cdot \left|\vec{A}\right| \cos\gamma\,, \tag{1.3}$$

where γ is the angle between $\vec{P}$ and $\vec{A}$. If the direction of propagation is different from that of the attenuation, which means $\gamma \neq 0$, the wavelet is called inhomogeneous. If $\gamma = 0$, the wavelet is called homogenous and the wavenumber can be written as

$$\vec{K} = \left[\ \frac{\omega}{v_H(\omega)} - ia(\omega)\ \right]\vec{b} = \frac{\omega}{v_C(\omega)}\vec{b}\,, \tag{1.4}$$

where $v_C(\omega)$ and $v_H(\omega)$ are called *complex velocity* and phase velocity. $\vec{b}$ denotes a unit vector of direction. $a(\omega)$ is called attenuation coefficient that can be calculated by (Aki and Richards, 1980)

$$a(\omega) = \frac{\omega}{2v_H(\omega)Q}\,, \tag{1.5}$$

where Q is the quality factor of rocks, which is the ratio of 2π times the power stored to the power dissipated (O'Connell and Budiansky, 1978). Here we assume that Q is exactly independent of frequency, which is called constant Q model (Kjartansson, 1979). The relation between $v_C(\omega)$ and $v_H(\omega)$ can be derived from equations (1.4) and (1.5)

$$\frac{1}{v_C(\omega)} = \frac{1}{v_H(\omega)}\left(1 - \frac{i}{2Q}\right). \tag{1.6}$$

Substituting equations (1.4) and (1.6) into equation (1.1), the Fourier spectrum of the wavelet at location $\vec{x}$ is

$$\hat{w}\left(\vec{x}, \omega\right) = \hat{w}(\omega)\,\exp\left[-\frac{\omega}{2Qv_H(\omega)}\vec{b}\cdot\vec{x}\right]\exp\left(-i\frac{\omega}{v_H(\omega)}\vec{b}\cdot\vec{x}\right), \tag{1.7}$$

where the phase velocity is expressed by (Futterman, 1962)

$$v_H(\omega) = v_{ref}\left(1 + \frac{1}{\pi Q}\ln\left|\frac{\omega}{\omega_{ref}}\right|\right), \tag{1.8}$$

where ω_{ref} and v_{ref} are reference frequency and the velocity at this frequency. Substituting equation (1.8) into (1.7) and dropping the term of the second power of $1/Q$, equation (1.7) becomes

$$\hat{w}(\vec{x},\omega) = \hat{w}(\omega)\exp\left\{-\frac{\vec{b}\cdot\vec{x}\omega}{v_{ref}}\left[\frac{\operatorname{sgn}(\omega)}{2Q} - \frac{i}{\pi Q}\ln\left|\frac{\omega}{\omega_{ref}}\right|\right]\right\}\exp\left(-i\frac{\vec{b}\cdot\vec{x}\omega}{v_{ref}}\right), \tag{1.9}$$

which represents a homogenous nonstationary wavelet by a constant-Q model in which the frequency-independent Q can change with the traveltime or the position of the waves. In equation (1.9), the first term on the right is the Fourier spectrum of the stationary source signature, the second term describes the amplitude dissipation and phase delay caused by attenuation and the third term determines the position of the wavelet propagation in the space.

1.3.2 1-D nonstationary wavelet

On the other hand, the relation between the real and imaginary parts of the wavenumber can be expressed by (Aki and Richards, 1980)

$$\frac{\omega}{v_H(\omega)} = \frac{\omega}{v_\infty} - H(a(\omega)), \tag{1.10}$$

where v_∞, the limit of $v_H(\omega)$ as $\omega \to \infty$, is identified in terms of the elastic modulus, $M\mu$, and density, ρ ,via $v_\infty = (M\mu/\rho)^{1/2}$. H denotes the Hilbert transform. When the propagating wavelet only depends on its traveltime or the distance traveled, we can replace the vectors $\vec{b}$ and $\vec{x}$ by 1 and x. Substituting equation (1.10) into equations (1.4) and (1.1) yields

$$\hat{w}(x,\omega) = \hat{w}(\omega)\exp\left[-a(\omega) + iH(a(\omega)) - i\frac{\omega}{v_\infty}\right]x. \tag{1.11}$$

By substituting equation (1.5) into (1.11), we have

$$\hat{w}(x,\omega) = \hat{w}(\omega)\exp\left[-\frac{|\omega| x}{2Qv_H(\omega)} + iH\left(\frac{x|\omega|}{2Qv_H(\omega)}\right)\right]\exp\left(-i\frac{\omega x}{v_\infty}\right), \tag{1.12}$$

which is called the 1-D nonstationary wavelet. For each Fourier component, the traveltime is

$$\tau = \frac{x}{v_H(\omega)}. \tag{1.13}$$

Substituting equation (1.13) into (1.12) yields

$$\hat{w}(x,\omega) = \hat{w}(\omega)\exp\left[-\frac{|\omega|}{2Q}\tau + i\frac{\tau}{2Q}H(|\omega|)\right]\exp\left(-i\frac{\omega x}{v_\infty}\right). \tag{1.14}$$

In equation (1.14), the second term on the right hand is an attenuation transfer function. By dropping the third term representing the position of the wavelet, Margrave and Lamoureux (2001) defined a nonstationary wavelet as

$$\hat{w}_\alpha(\tau,\omega) = \hat{w}(\omega)\alpha(\tau,\omega) = \hat{w}(\omega)\exp\left[-\frac{|\omega|}{2Q}\tau + i\frac{\tau}{2Q}H(|\omega|)\right], \tag{1.15}$$

where α represents the attenuation transfer function. Thus, the nonstationary wavelet is defined as the product of the Fourier spectrum of the source signature and the attenuation transfer function. In the time domain, the nonstationary wavelet is written as

$$w_\alpha(\tau,t) = \frac{1}{2\pi}\int \hat{w}_\alpha(\tau,\omega)\exp(i\omega t)d\omega. \tag{1.16}$$

If $Q \to \infty$, $w_\alpha(\tau,t)$ will not change with traveltime, τ. That means the wavelet is stationary.

Equations (1.1), (1.9), (1.12) and (1.14) all represent the nonstationary wavelet with different assumptions. At the same time, all of them are wavefield extrapolators for a plane wave traveling in an anelastic medium, but corresponding to inhomogeneous, 3-D homogeneous and 1-D homogeneous waves respectively. They also can be used as forward or inverse-Q filters. The inverse-Q filter can be implemented in the same way as wavefield extrapolation (Hargreave and Calvert, 1991; Wang, 2002)

1.4 Brief review of the nonstationary problem

Lines and Ulrych (1977) shown that seismic wavelets and deconvolution operators should be estimated in a time-adaptive sense due to the nonstationarity of seismic trace. They concluded that the maximum-entropy approach is preferred for time-adaptive deconvolution. The usual approaches to reduce the nonstationarity of seismic data are inverse-Q filtering (Bickel and Natarajan, 1985; Hale 1981) before deconvolution and TVSW (Yilmaz, 1987) after stacking. The effectiveness of the inverse-Q filtering depends on the accuracy of the Q estimation. In most cases, a Q estimate from surface data is problematic (White, 1992). TVSW can reduce the nonstationarity by designing and applying the time-variant whitening operator in frequency domain, but can not accurately compensate the constant-Q attenuation because it loses a phase correction. Margrave (1998) provided the concept of a nonstationary filter and gave a nonstationary convolution and combination model. This framework made a foundation for nonstationary deconvolution and wavelet estimation. In nonstationary deconvolution the attenuation effect is incorporated into the deconvolution operator and can be implemented with or without knowledge of Q (Schoepp, 1998). The performance of nonstationary deconvolution depends on the accuracy of the wavelet estimates. Usually people verify the accuracy of the wavelet estimates by comparing the result of deconvolution to the convolution of a stationary wavelet and a reflectivity from log data. This wavelet is often supposed to be zero-phase Ricker wavelet. Another approach for verifying the wavelet estimates is to compare the nonstationary wavelet estimates from the surface data to the windowed VSP downgoing waves which are direct measurements of the nonstationary wavelets.

1.5 Original contribution in this thesis

The original contribution in this thesis is described as follows:

1. The several nonstationary wavelet models were provided and the nonstationary wavelet model proposed by Margrave and Lamoureux (2001) is theoretically verified.

2. the synthetic offset VSP downgoing wavelets were generated in horizontally layered anelastic media by complex ray tracing, and also the Ganley's method (1981) for VSP synthetic seismograms with attenuation was extended to generate the zero-offset VSP synthetic seismograms for a many-layered model derived from a real sonic and density log.

3. It is first shown that the wavelet estimate by Gabor deconvolution on a synthetic nonstationary trace is quite close to the input nonstationary wavelet.

4. The nonstationary wavelets were estimated from the seismic data obtained via a joint VSP and surface seismic acquisition. The VSP wavelets were extracted from the separated downgoing waves and the surface wavelets were estimated by Gabor deconvolution on the pre-processed surface data.

5. Nonstationary wavelets were also estimated by time-domain and frequency-domain Wiener methods on gained data in temporally short analysis window that were moved down the traces in increments.

6. The phase of the nonstationary wavelet with a vibroseis source was examined on both synthetic and real data, and was found to be close to minimum phase.

7. A novel method for evaluating nonstationary wavelet estimates was developed. This method verified the wavelet estimates from surface data by the wavelet estimates from VSP data based on the fact that both of them are nonstationary and the latter are directly recorded in the downgoing waves.

8. It is verified that Gabor deconvolution can accurately estimate the nonstationary wavelet embedded in real seismic records. Therefore, the accuracy of Gabor deconvolution was validated.

9. The result also shows that Gabor deconvolution is superior to Wiener methods in wavelet estimation.

CHAPTER 2 NONSTATIONARY WAVELET SIMULATION

Synthetic seismograms in an anelastic medium can be generated by ray tracing or finite difference approaches (Kjartannson, 1979; Ganley, 1981; Ursin and Arntsen, 1985; Hearn and Krebes, 1990; Carcione, 1993). Nonstationary wavelet simulation is different from the creation of synthetic seismograms in that it only deals with the attenuation effect on the wavelet when it travels through the medium. This attenuation may or may not be associated with the direction of wavelet propagation depending on the purpose of the simulation. For the comparison of the simulated wavelets received in the well and those recorded on the surface at the far horizontal offset, the difference in the direction of attenuation and propagation should be considered. This means we need to simulate an inhomogeneous wavelet. The complex ray tracing method is chosen for the wavelet comparison since it can handle the attenuation angle and propagation angle by the *stationary ray approach* (Hearn and Krebes, 1990). There are many approaches for simulating homogeneous wave propagation. The investigation of homogeneous VSPs and surface wavefields in a constant-Q medium is also presented in this Chapter.

2.1 Nonstationary wavelet simulation using complex rays

Unlike conventional ray tracing methods, the complex ray method traces the seismic ray in attenuating media with the complex velocity. Therefore the factors associated with the complex velocity, such as ray parameter, wavenumber and traveltime, are complex also. The original code for calculating synthetic seismograms using the complex ray was kindly provided by Dr. Krebes. It was modified in this research to perform the nonstationary wavelet simulation measured on the surface and in the borehole. Comparison of the simulated VSP wavelets and surface wavelets will be discussed in Chapter 5.

2.1.1 Simulating nonstationary wavelets recorded on surface

When a wavelet passes through a sequence of anelastic horizontal layers, it is inhomogeneous and nonstationary. Thus equation (1.1) should be used for this wavelet simulation. This equation can also be expressed as (Hearn and Krebes, 1990)

$$\hat{w}(\tau_C, \omega) = \hat{w}(\omega)\exp(-i\omega\tau_C), \tag{2.1}$$

where complex traveltime is

$$\tau_C = \frac{\vec{K} \cdot \vec{x}}{\omega} = px + \left(\frac{1}{v_C^2(\omega)} - p^2\right)^{1/2} z \ , \tag{2.2}$$

with $v_C(\omega)$ being complex velocity expressed by equation (1.6) and p being complex ray parameter expressed as

$$p = \frac{\sin\theta}{v_C(\omega)}, \tag{2.3}$$

where θ is complex angle. The complex ray parameter is solved as an independent parameter in ray tracing. With the assumption of linear superposition, the nonstationary wavelet, passing through a sequence of anelastic horizontal layers, can be simulated by

$$w_\alpha(\tau_R, t - \tau_R) = \frac{1}{2\pi}\int_{-\infty}^{\infty} \hat{w}(\omega)\exp[i\omega(t - \tau_C)]d\omega \tag{2.4}$$

where τ_R is real part of τ_C, which represents the traveltime of nonstationary wavelet. By summation over m layers, τ_C is expressed as

$$\tau_C = pX + \sum_{j=1}^{m} h_j\left(\frac{1}{v_{Cj}^2(\omega)} - p^2\right)^{1/2}, \tag{2.5}$$

where h_j and $v_{Cj}(\omega)$ are the thickness and complex velocity of the j^{th} layer. m is the total number of layers and X is the half horizontal offset between the source and the receiver. To find minimum traveltime, let $d\tau_C/dp = 0$, and then X can be written as

$$X = \sum_{j=1}^{m} pv_{Cj}h_j\left(1 - p^2v_{Cj}^2\right)^{-1/2}. \tag{2.6}$$

To simulate the wavelet, we first give X, h_j, Q_j, $v_{ref}(j)$ and calculate $v_{Cj}(\omega)$ by equation (1.6). Then solve for p from

$$X - \sum_{j=1}^{m} p v_{Cj} h_j \left(1 - p^2 v_{Cj}^2\right)^{-1/2} = 0. \qquad (2.7)$$

and substitute p into equation (2.5) to compute complex traveltime, τ_C. Finally we simulate the wavelet, $w_\alpha(\tau_R, t - \tau_R)$, by equation (2.4) from given source signature, $\hat{s}(\omega)$.

2.1.1.1 An example of a three-layered model

By solving equation (2.7) using Newton-Raphson method (Hearn and Krebes, 1990), we can create an ideal nonstationary wavelet section without the effect of reflection, transmission and geometrical spreading. Table 2.1 shows the parameters of the anelastic model where h, v, ρ and Q are the thickness, reference interval velocity, interval density and interval Q values. Figure 2.1 shows the zero-phase source signature and its spectrum with bandwidth ranging from 10 to 90 Hz. Horizontal offsets between source and receivers are from 60 to 900 m at 60 m spacing.

Layer	h(m)	v(m/s)	$\rho\left(g / cm^3\right)$	Q
1	500	1800	2.0	40
2	1000	2300	2.1	50
3	1000	3000	2.2	60

Table 2.1 The subsurface model parameters.

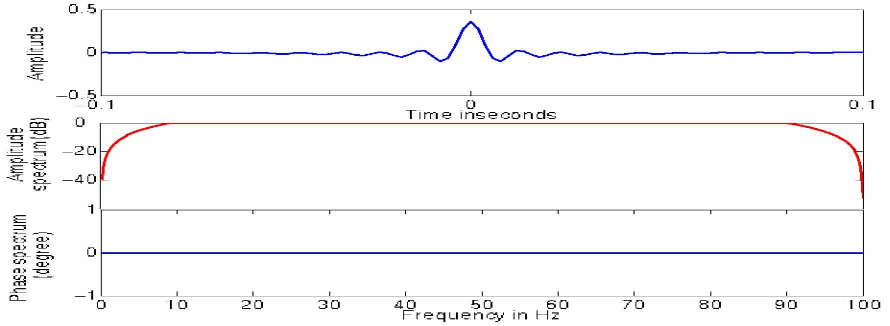

Figure 2.1 The source signature and its spectrum which is a zero-phase sinc function with two tapers added at the ends of the spectrum.

Figure 2.2 (a) shows the nonstationary wavelet (total response) on which the waveform variation is caused only by constant-Q attenuation. Although the source signature is zero-phase, the propagating wavelet is gradually close to the minimum phase with increasing traveltime. This phenomenon will be further verified in Chapters 3 and 4. Figure 2.2 (b) shows the vertical components of the nonstationary wavelet. Figure 2.2 (c) shows the vertical components of the nonstationary wavelet with the geometrical spreading and Figure 2.2 (d) shows the vertical components of the nonstationary wavelet including the geometrical spreading and transmission/reflection effects, which is actually the synthetic seismogram in the attenuating media. In wavelet estimation we need to transform the traces shown in Figure 2.2 (d) into the nonstationary wavelet shown in Figure 2.2 (a). The amplitude spectra of wavelets along the first and the second events as well as that of the source signature are shown in Figure 2.3. The slope of the amplitude spectrum becomes higher and higher with increasing horizontal offset and traveltime. This is the result of the constant-Q attenuation. The amplitude decay along the first event is more severe compared to the attenuation along the second event. This decay increases directly with increasing traveltime.

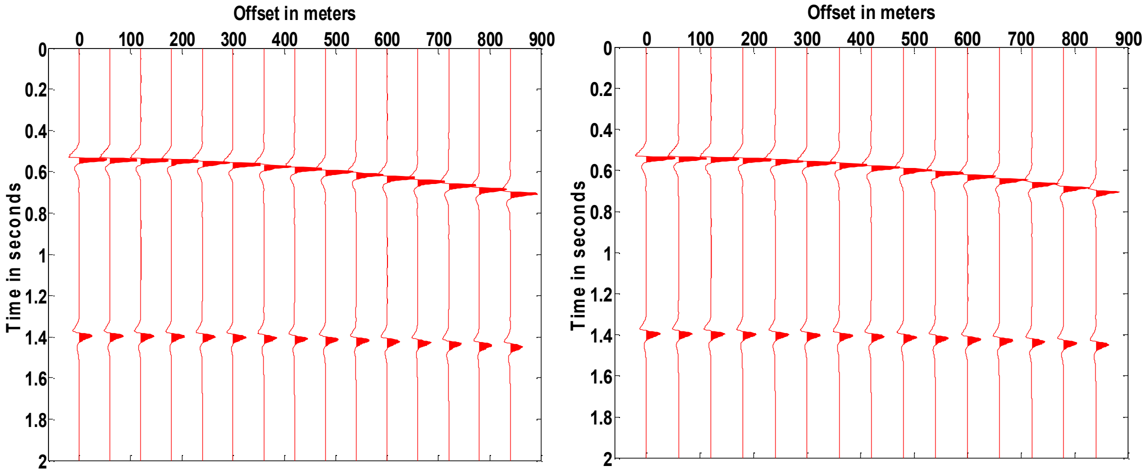

(a) (b)

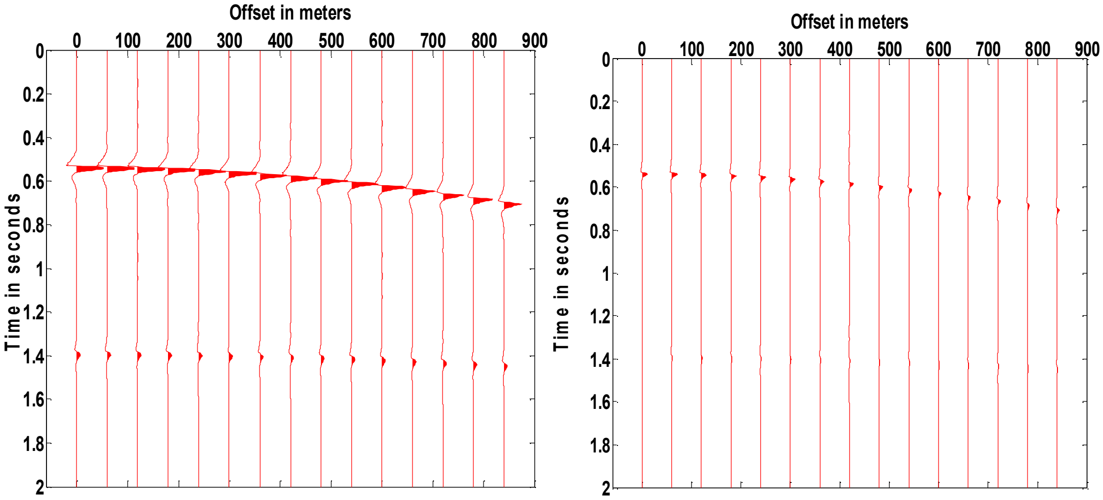

(c) (d)

Figure 2.2 Simulated nonstationary wavelet (total response) (a), vertical components of displacement of the wavelets (b), vertical components with geometrical spreading decay (c) and vertical components including geometrical spreading and transmission/reflection factors (d).

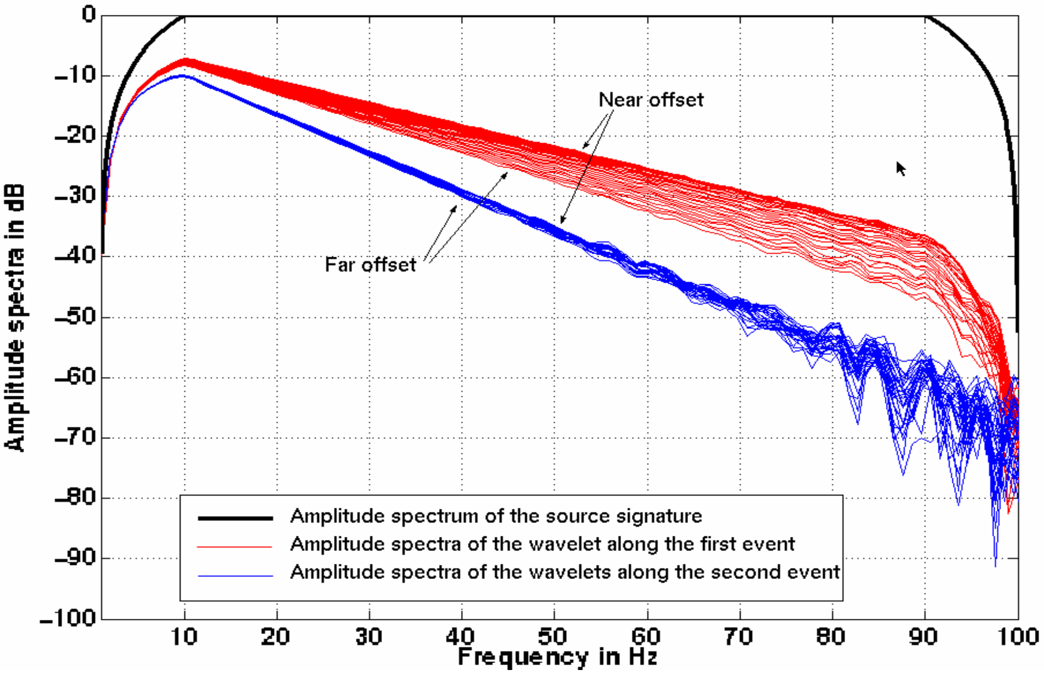

Figure 2.3 Amplitude spectra of the nonstationary wavelet along the first (red) and the second (blue) reflection events shown in Figure 2.2 (a), and amplitude spectrum of the source signature (black).

2.1.1.2 Amplitude analysis

To compare the nonstationary wavelet from the surface and VSP data, it is necessary to analyze the possible factors associated with amplitude variation. Geometrical spreading, reflection and transmission, source-receiver directivity and anelastic attenuation contribute to the amplitude variation. In our computation, the analytical formulas for computing the geometrical spreading, vertical component conversion and the reflection/transmission factors are given by Krebes (1984), Hearn and Krebes, (1990). Each of these factors was included in the amplitude computation step-by-step to see its effect. All the factors depend on frequency since the velocity and traveltime are frequency-dependent. Figure 2.4 shows five different amplitude spectra corresponding to the source signature, the nonstationary wavelet, the vertical component of this wavelet, the vertical component with the geometrical spreading, and the reflected vertical component with the geometrical spreading. All of them are reflected from the first reflector and received at an offset of 420 m. The decay of the amplitude spectrum with frequency is caused by the constant-Q attenuation. The other factors perform like constant scaling to the entire frequency spectrum and are independent of the frequency. This property will be helpful in the comparison of the wavelet estimates where we will assume that all the factors but the constant-Q attenuation are frequency-independent.

Figure 2.5 shows the log spectral ratio (from Tonn,1991) from the first reflection event shown in Figure 2.2 (a) with the reference spectrum being the amplitude spectrum of the first trace. The average Q between the surface and the first reflector is estimated by the spectral ratio method (White, 1992). The Q estimate is nearly equal to the given value in Table 2.1 at the offset from 250 m to 800 m. It shows the amplitude of the simulated wavelets is correct.

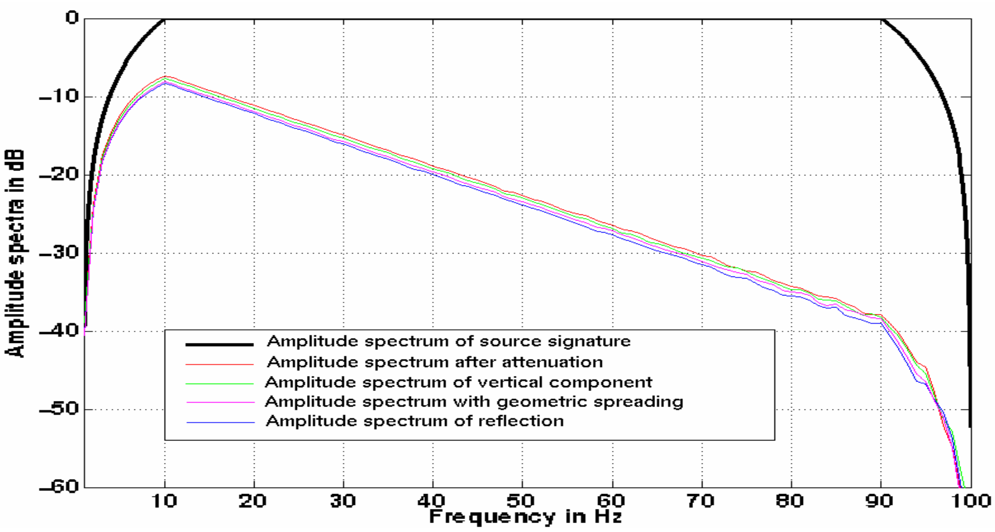

Figure 2.4 Amplitude spectra of the wavelet at offset of 420 m, its vertical component, vertical component with spreading loss and reflection/transmission as well as the amplitude spectrum of the source signature.

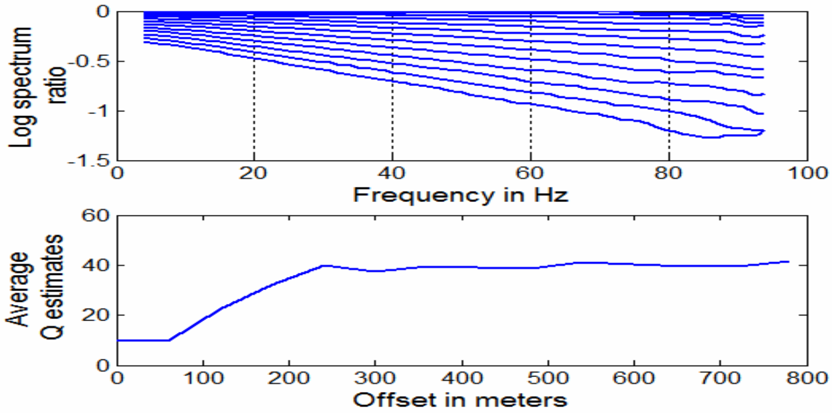

Figure 2.5 Log spectral ratio (top) from the first event shown in Figure 2.2 (a) and Q estimates from the same event (bottom).

2.1.2 Simulating zero-offset VSP wavelets by complex rays.

Suppose the receiver is located in the k^{th} layer. As shown in Figure 2.6, the horizontal offset from source to borehole can be expressed as

$$X = \sum_{j=1}^{k-1} \frac{h_j p}{\sqrt{\frac{1}{v_{Cj}^2} - p^2}} + \frac{\Delta Z p}{\sqrt{\frac{1}{v_{Ck}^2} - p^2}}, \tag{2.8}$$

where v_{Cj} and h_j is the complex velocity and the thickness of the j^{th} layer. ΔZ is the vertical component of the ray vector in the k^{th} layer, which can be calculated by

$$\Delta Z = \left(Z - \sum_{j=1}^{k-1} h_j \right), \tag{2.9}$$

where Z is the depth at which the receiver located. The traveltime of downgoing waves from source to each receiver at depth of Z is

$$\tau_C = pX + \sum_{j=1}^{k-1} h_j \left(\frac{1}{v_{Cj}^2} - p^2 \right)^{1/2} + \Delta Z \cdot \left(\frac{1}{v_{Ck}^2} - p^2 \right)^{1/2}, \tag{2.10}$$

The steps for VSP wavelet simulation are similar to those for surface wavelet simulation. Figure 2.7 shows the simulated vertical downgoing wavelets. The VSP wavelets were simulated with the same medium model and source signature as those in the surface wavelet simulation. The source was located 30 m apart from the specified well and 14 receivers located in the well at depths from 200 to 1500 m at 100 m spacing. The energy dissipation with the high frequency component attenuation is caused only by the constant-Q attenuation.

Figure 2.8 shows the amplitude spectra of VSP downgoing wavelets in dB down. For shallow wavelets, the difference in dB down is bigger than that in deep wavelets since the velocity is slower in the first layer than that in the second layer.

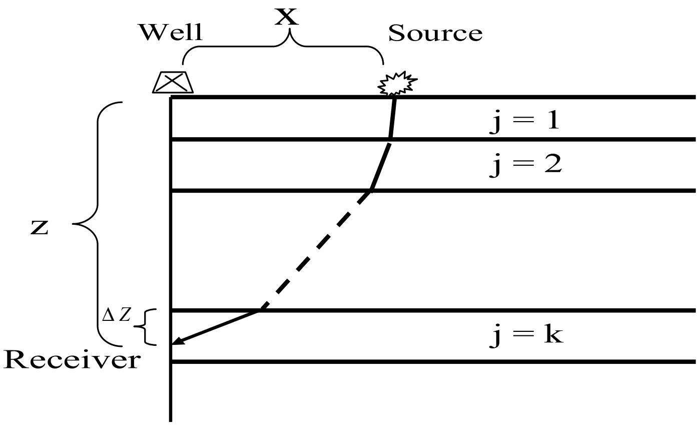

Figure 2.6 Geometry of VSP wavelet simulation. Only downgoing waves are simulated.

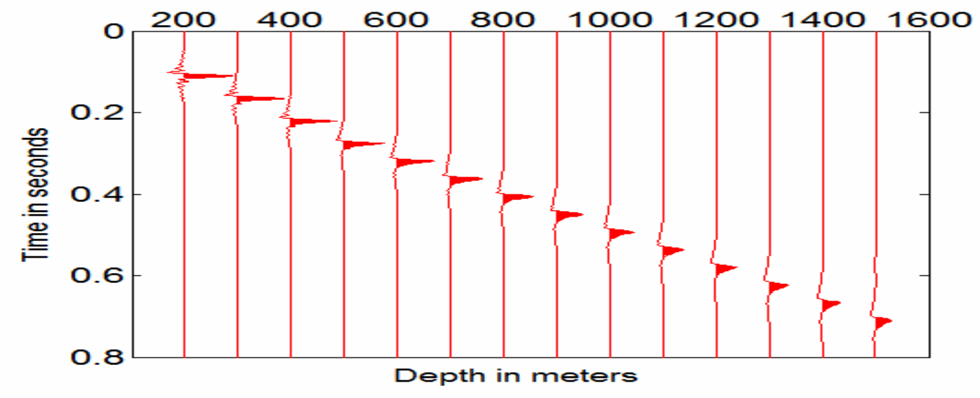

Figure 2.7 VSP downgoing wavelets. The source signature and media parameters are the same as those used in surface seismogram. The reflectors are located 500 m and 1500 m respectively.

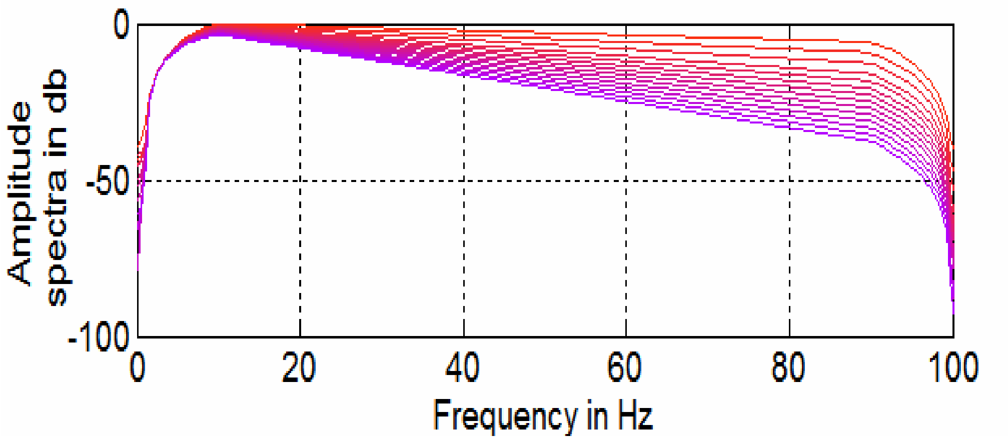

Figure 2.8 Spectra of VSP downgoing wavelet shown in Figure 2.7.

Figure 2.9 shows the log spectral ratio from the spectra shown in Figure 2.8 and Q estimates by the spectral ratio approach. The amplitude spectrum of the first wavelet is used as the reference spectrum. The average Q is close to the input interval Q in the first layer and then gradually approximates to the interval Q given in the second layer. That means the variation in the amplitude spectra of the simulated wavelets is reasonable.

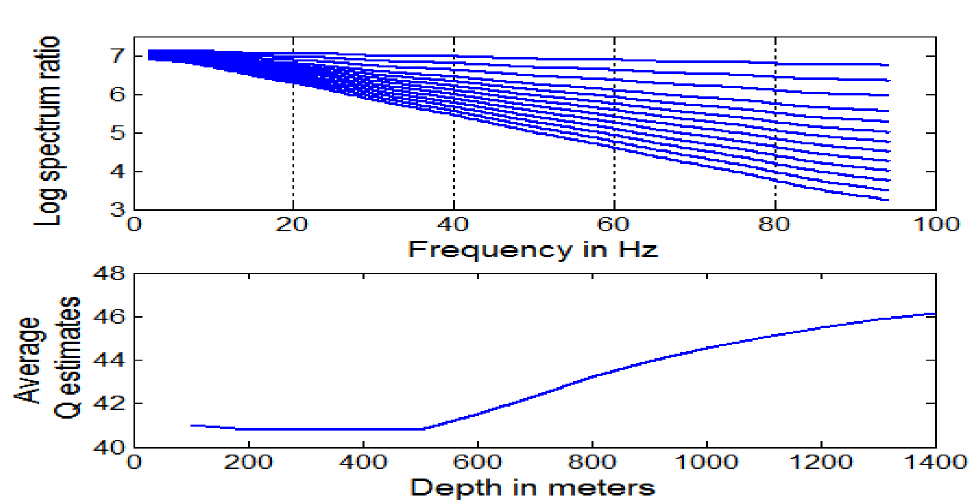

Figure 2.9 Log spectral ratio and average Q estimates from spectra shown in Figure 2.8.

2.2 Zero-offset VSP wavelet simulation by 1-D wavefield extrapolation

The seismogram obtained using complex rays is accurate for inhomogeneous waves. In our practice, sometimes, in the case of a multi-thin bed model, ray tracing is very slow to converge. The solution of the equation (2.7) may converge to another root or diverge if the initial guess is poor in the Newton-Raphson method. For normal-incidence waves, we consider an alternate method under the condition of $\gamma = 0$, that always gives a solution. Considering a plane, compressional wave normally incident in a horizontally layered anelastic medium, from equation (1.7) the Fourier component of the wavefront at depth z can be expressed as

$$\hat{w}(z,\omega) = D(\omega)\exp\left(-\frac{\omega z}{2Qv_H(\omega)}\right)\exp\left(-i\frac{\omega z}{v_H(\omega)}\right) + U(\omega)\exp\left(\frac{\omega z}{2Qv_H(\omega)}\right)\exp\left(i\frac{\omega z}{v_H(\omega)}\right), \quad (2.11)$$

where $D(\omega)$ is the Fourier spectrum of the downgoing source signature and $U(\omega)$ is the Fourier spectrum of the upgoing source signature. The source is considered to be buried within the first layer. Equation (2.11) was also given by Ganley (1981). Here his method is extended to generate zero-offset VSP synthetic seismograms for a many-layered model derived from a real sonic and density log.

If $D(z,\omega)$ is the Fourier spectrum of the downgoing wavelet at the depth z, then the downgoing wavelet at $z+\Delta z$ is given by

$$D(z+\Delta z,\omega) = D(z,\omega)\exp\left(-\frac{\omega|\Delta z|}{2Qv_H(z,\omega)}\right)\exp\left(-i\frac{\omega\Delta z}{v_H(z,\omega)}\right), \quad (2.12)$$

where Δz is the depth step which should be much less than the minimum thickness of any layer in the model, and $v_H(z,\omega)$ is the phase velocity. In the same manner, the upgoing wavelet, $U(z+\Delta z,\omega)$, is expressed by

$$U(z+\Delta z,\omega) = U(z,\omega)\exp\left(-\frac{\omega|\Delta z|}{2Qv_H(z,\omega)}\right)\exp\left(i\frac{\omega|\Delta z|}{v_H(z,\omega)}\right), \quad (2.13)$$

where $\Delta z > 0$ for the downgoing waves and $\Delta z < 0$ for the upgoing waves. Equation (2.12) is used to move the primary wavefield downward while equation (2.13) moves the reflected primary wavefield upward. Multiples are not modeled.

For the normal-incidence VSP in n layers over a half space, we can include reflections and transmissions in the zero-offset VSP seismogram in anelastic media as follows. First the layer depths of the model are all shifted slightly to fall exactly on a depth step. This causes minimal error if Δz is much smaller than the layer thickness. Then we use equations (2.12) and (2.13) to extrapolate the downgoing wavefield and the upgoing wavefield. If the wavefield reaches the j^{th} interface, the downgoing wave transmitted to the next layer is given by

$$D'(z = h_j, \omega) = (1 - R_j) D(z = h_j, \omega), \tag{2.14}$$

and the upgoing wave starting in the next layer is

$$U'(z = h_j, \omega) = \frac{-R_j}{(1 + R_j)} D(z = h_j, \omega) + \frac{1}{1 + R_j} U(z = h_j, \omega), \tag{2.15}$$

where D' and U' are the downgoing wavefield and the upgoing wavefield in the next layer. h_j is the depth of the j^{th} interface and R_j is the complex reflection coefficient at the j^{th} interface, which is written as (Ganley, 1981)

$$R_j = \frac{\rho_{j+1} v_{Cj+1}(\omega) - \rho_j v_{cj}(\omega)}{\rho_{j+1} v_{Cj+1}(\omega) + \rho_j v_{Cj}(\omega)} \tag{2.16}$$

where $v_{Cj}(\omega)$ is the interval complex velocity that can be calculated by equation (1.6) and ρ_j is the interval density.

The source signature, shown in Figure 2.10, is a minimum-phase waveform. The receivers were located in a vertical well at depths from 320 m to 1800 m with a receiver interval of 20 m. The model for synthetic data can be constructed from sonic and log data by making equal time layers (Margrave, 1996). The log data for the velocity and density calculations come from a well at Rosedale nearby Drumheller. Figure 2.11 shows the log data and impedance curve from the horizontal layers with equal traveltime of 0.002 second. Q for each layer is 50.

Figure 2.12 shows the synthetic VSP data from the given model. This data consist of both the primary downgoing and the primary upgoing waves which are attenuated with increasing travel distance. Figure 2.13 shows Fourier amplitude spectra of the downgoing wavelets in which the dominant frequency is shifted toward low frequency and the high frequency components are attenuated with the increasing depth. Figure 2.14 shows the impedance of the given model and the deconvolved upgoing waves. The deconvolution operators were designed from downgoing waves and applied to the upgoing waves recorded at the same level on trace-by-trace basis (Ross and Shah, 1987). The variation in impedance is consistent with the amplitude change in the upgoing waves where the peaks of the first arrivals are coincident with increasing in the impedance.

Figure 2.15 shows the corridor stack of the deconvolved upgoing waves and well-log synthetic seismograms with Ricker wavelet which has the same dominant frequency as the source signature shown in Figure 2.10. The corridor stacking over the deconvolved and flattened upgoing waves is similar to the nonstationary deconvolution of the zero-offset seismic trace recorded on the surface. Our result shows that the corridor stack of the deconvolved VSP upgoing waves tied quite closely to the well-log synthetic trace. It also shows that the deconvolution procedure can not completely remove the effect of the attenuation since these two traces display different gain factors.

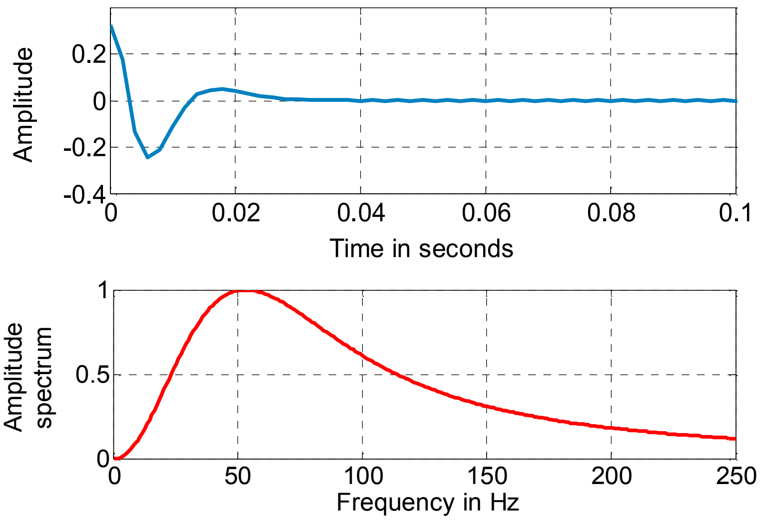

Figure 2.10 A minimum-phase source signature and its amplitude spectrum.

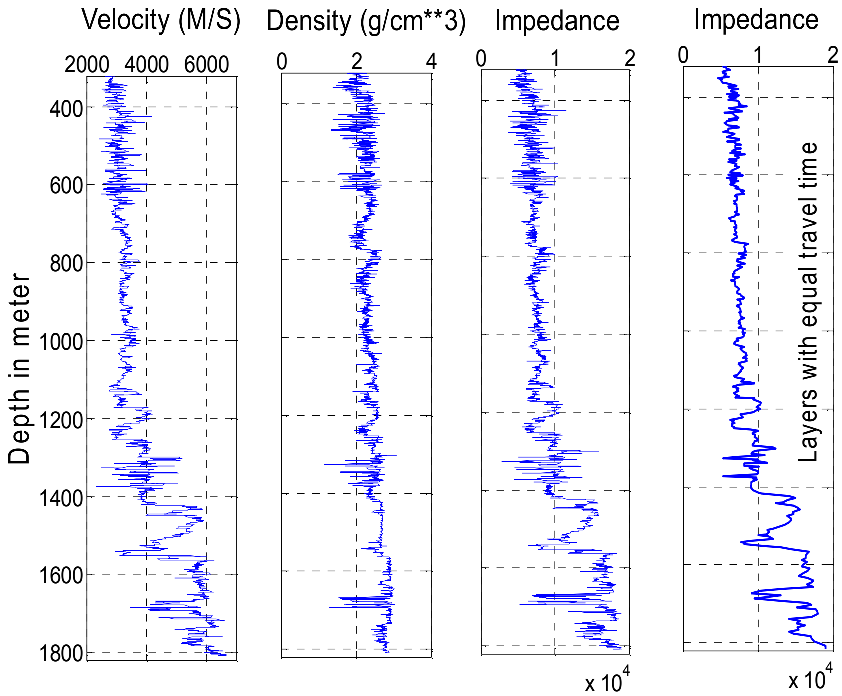

Figure 2.11 The simultaneous velocity from sonic log, density log, impedance and impedance model with the equal traveltime within each layer.

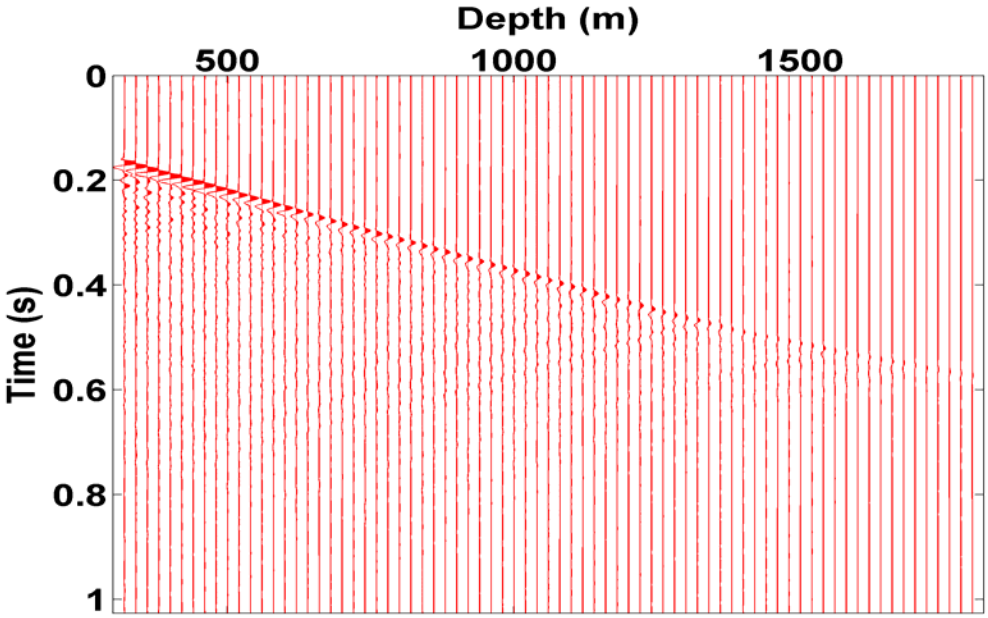

Figure 2.12 VSP synthetic seismogram including constant-Q attenuation.

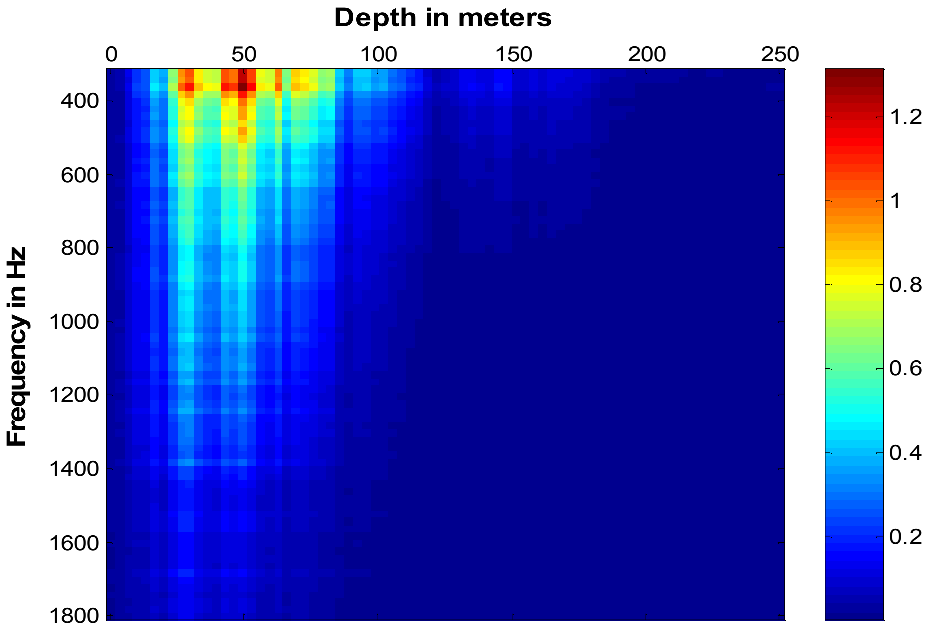

Figure 2.13 Amplitude spectra of the downgoing wavelets.

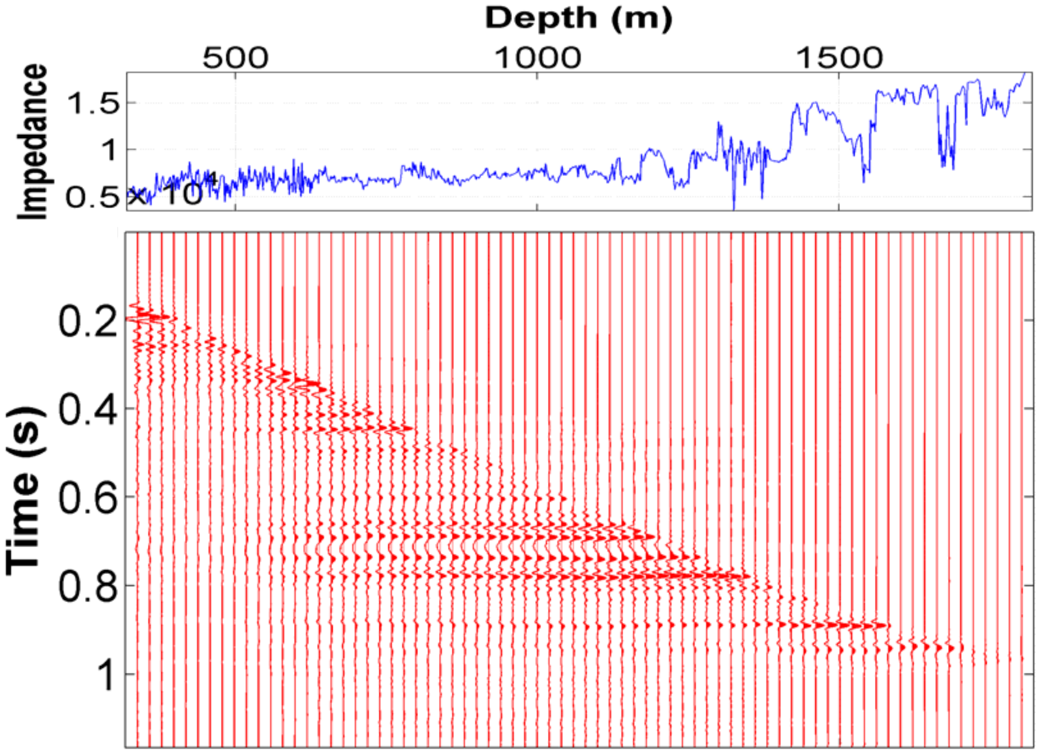

Figure 2.14 Impedance model and the flattened and deconvolved VSP upgoing waves. Major reflection events are consistent with the rapid changes in the impedance.

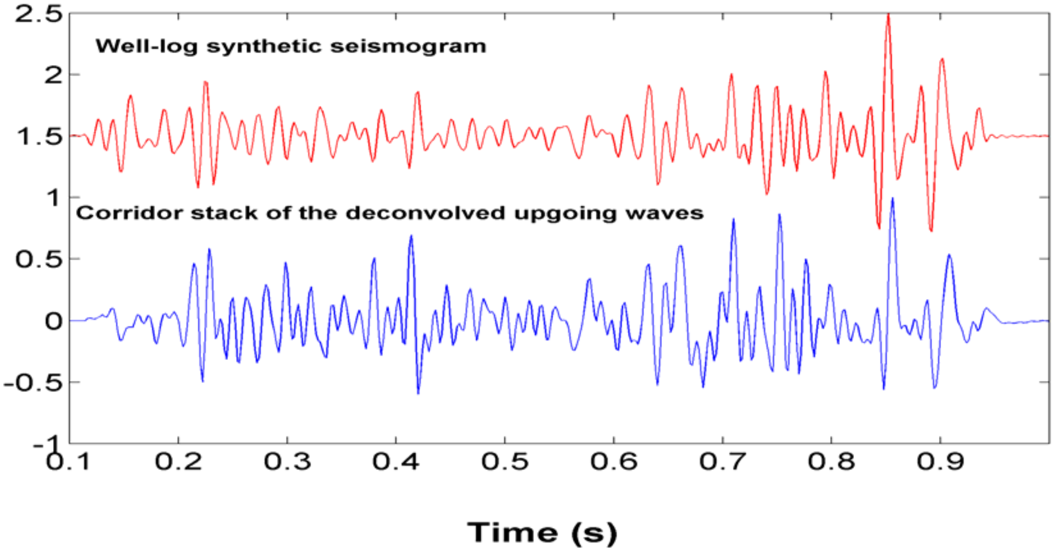

Figure 2.15 Well-log synthetic seismogram with Ricker wavelet and corridor stack of the deconvolved upgoing waves.

2.3 Nonstationary wavelet simulation by finite difference method

If the medium is not horizontally layered, it will be difficult to use ray tracing to simulate the nonstationary wavelet since the angle between attenuation and propagation will vary with the dip of the subsurface. The easy way to simulate the nonstationary wavelet in 2-D is to include the attenuation directly in the wavefield extrapolation formula under the assumption of $\gamma = 0$ (Kjartansson, 1979, Hargreaves and Calvert, 1991, and Wang, 2002). A frequency-space domain wavefield extrapolation approach is a reasonable choice for nonstationary wavelet simulation since the effect of energy dissipation and velocity dispersion can be easily included in the extrapolator.

In a 2-D medium, the wave equation for compressional waves in space-frequency domain can be written as

$$\frac{\partial^2 P}{\partial z^2} = -\frac{\partial^2 P}{\partial x^2} - \frac{\omega^2}{v^2} P, \tag{2.17}$$

where $P = P(x, z, \alpha)$ represents the pressure wavefield , $v = v(x, z)$ is the velocity and α is the angular frequency. The minus sign convention in forward Fourier transform is chosen. Equation (2.17) is a two-way wave equation. If we directly use it in wavefield continuation, multiples will be generated when the velocity is not a continuous function of space. Thus, a one-way equation is useful if multiples are not wanted. The square root equation can be directly derived from equation (2.17), that is

$$\frac{\partial P}{\partial z} = \pm \frac{i\omega}{v} \sqrt{1 + \frac{v^2}{\omega^2} \frac{\partial^2}{\partial x^2}} P, \tag{2.18}$$

where the plus sign on the right side of the equation represents the wave traveling toward the source and the minus sign means the wave going away from the source. Based on the exploding reflector concept (Claerbout, 1976), the zero-offset reflected wave recorded at the surface can be simulated by an upward continuation of the wavefield from the exploding reflector using a half velocity. Thus we chose the minus sign in equation (2.18).

To approximate equation (2.18) with a finite-difference equation, we use the continued fraction method (Lee and Suh, 1985). Suppose

$$Y = (1 + S)^{\frac{1}{2}} - 1, \tag{2.19}$$

where

$$S = \frac{v^2}{\alpha^2} \frac{\partial^2}{\partial x^2}. \tag{2.20}$$

The n^{th} order approximation of Y can be given by

$$Y_n = \frac{S}{2 + Y_{n-1}} . \tag{2.21}$$

The 2^{nd} order approximation of equation (2.18) for the downgoing wavefield can be written as a conventional 45-degree equation (Lee and Suh, 1985)

$$\frac{\partial P}{\partial z} = -\frac{i\omega}{v}(1+Y_2)P \quad , \tag{2.22}$$

where

$$Y_2 = \frac{S}{2+Y_1} = \frac{S}{2+\frac{S}{2+Y_0}} , \tag{2.23}$$

where $Y_0 = 0$. Substituting equation (2.23) into equation (2.22) yields

$$\frac{\partial P}{\partial z} = -\frac{i\omega}{v}P - \frac{i\omega}{v}\frac{\frac{v^2}{\omega^2}\frac{\partial^2}{\partial x^2}}{2+\frac{v^2}{2\omega^2}\frac{\partial^2}{\partial x^2}}P \quad . \tag{2.24}$$

The wavefield P is related to time-shifted wavefield $P^{'}$ (Yilmaz, 1987)

$$P = p^{'} e^{-i\omega\frac{z}{\bar{v}}} , \tag{2.25}$$

where $\frac{z}{\bar{v}}$ is the retarded time at depth z. The derivative of P over z is

$$\frac{\partial P}{\partial z} = \left(\frac{\partial}{\partial z}P' - i\frac{\omega}{\bar{v}}P' \right) e^{-i\omega\frac{z}{\bar{v}}} \tag{2.26}$$

Substituting equations (2.25) and (2.26) into equation (2.24) then it can be written as

$$\frac{\partial P^{'}}{\partial z} = (\frac{i\omega}{\bar{v}} - \frac{i\omega}{v})P^{'} - \frac{i\omega}{v}\frac{\frac{v^2}{\omega^2}\frac{\partial^2}{\partial x^2}}{2+\frac{v^2}{2\omega^2}\frac{\partial^2}{\partial x^2}}P^{'} \quad . \tag{2.27}$$

If the horizontal velocity variation can be ignored, $\bar{v} \approx v$, equation (2.27) can be expressed as

$$\frac{4\omega^2}{v^2}\frac{\partial P'}{\partial z}+\frac{\partial^3 P'}{\partial x^2 \partial z}+\frac{2i\omega}{v}\frac{\partial^2 P'}{\partial x^2}=0. \tag{2.28}$$

After getting the solution $P'(x,z,\omega)$ from equation (2.28), we then use equation (2.25) to shift the wavefield from depth z to surface. The synthetic data is $P(x,z=0,t)$, which is the inverse Fourier transform of the final solution from equation (2.25).

Now we need to include the effect of the constant-Q attenuation in Equations (2.25) and (2.28). The constant-Q theory of Kjartansson and others is the simplest attenuation theory. It can be easily incorporated in the wavefield continuation. The relationship between the dispersion and constant-Q attenuation given by Kjartansson (1979) is

$$\frac{v_C(\omega)}{v_{ref}(\omega_0)}=\left(\frac{i\omega}{\omega_0}\right)^{\zeta}, \tag{2.29}$$

where ω_0 is the reference frequency, v_{ref} is the phase velocity at the reference frequency and

$$\zeta=\frac{1}{\pi}\tan^{-1}\left(\frac{1}{Q}\right). \tag{2.30}$$

Let $\omega_0=1$. Then the complex velocity can be written as

$$v_C(\omega)=v_{ref}\left(\frac{i\omega}{\omega_0}\right)^{\zeta}=v_{ref}\,\omega^{\zeta}\exp\left(\frac{\pi}{2}i\zeta\right), \tag{2.31}$$

If $Q >> 1$, the equation (2.30) can be approximated by

$$\varsigma\approx\frac{1}{\pi Q}. \tag{2.32}$$

Substituting equation (2.32) into equation (2.31) and then replacing the velocity v in equations (2.25) and (2.28) for $v_C(\omega)$ yield

$$P = p' e^{-i\frac{z}{v_{ref}} \exp\left(-i\frac{1}{2Q}\right)\omega^{1-\frac{1}{\pi Q}}} , \tag{2.33}$$

and

$$\frac{4\omega^2}{v_{ref}^2\Omega^2}\frac{\partial P'}{\partial z} + \frac{\partial^3 P'}{\partial x^2 \partial z} + \frac{2i\omega}{v_{ref}\Omega}\frac{\partial^2 P'}{\partial x^2} = 0 , \tag{2.34}$$

where

$$\Omega = \omega^{\frac{1}{\pi Q}} \exp\left(i\frac{1}{2Q}\right). \tag{2.35}$$

Usually v_{ref} is chosen as the real interval velocity.

Using the Crank-Nicolson difference method (Smith, 1978), the solution for equation (2.34) can be represented with the finite difference equation

$$aP'_{m-1,n+1} + bP'_{m,n+1} + aP'_{m+1,n+1} = cP'_{m-1,n} + dP'_{m,n} + cP'_{m+1,n} , \tag{2.36}$$

with the notations of:

$$P'_{m,n} = P'(m\delta x, n\delta z),$$

$$a = \frac{1}{\delta z}\left(\frac{iv_{ref}\Omega}{2\omega} + \frac{i\omega x^2}{6v_{ref}\Omega\delta z}\right) - 0.5 ,$$

$$b = -2a + \frac{2i\omega\delta x^2}{v_{ref}\Omega\delta z} ,$$

$$c = a + 1 ,$$

$$d = -2c - \frac{2i\omega\delta x^2}{v_{ref}\Omega\delta z} . \tag{2.37}$$

The computing process includes several steps:

1. Given a model in (x, z) domain as well as a exploding reflector $P'(x, z, t = 0)$.

2. From maximum depth level, for each depth step, solve the equation (2.36) to get the monochromatic wavefield at a given depth and then shift the wavefield upward to surface by equation (2.33).

3. At depth $z = 0$, transform the wavefield $P(x, z = 0, \omega)$ to the time domain.

Figure 2.16 is the minimum-phase source signature which is assumed to be located on the interfaces shown in Figure 2.17. Q for all the layers is 40. Figure 2.18 shows the resulting seismic section. The wavelets broadening along the dipping reflector show the dispersion effect. The amplitude of the wavelet does not change along the horizontal event for the zero-offset synthetic data, but decays greatly along the dipping event due to the constant-Q attenuation.

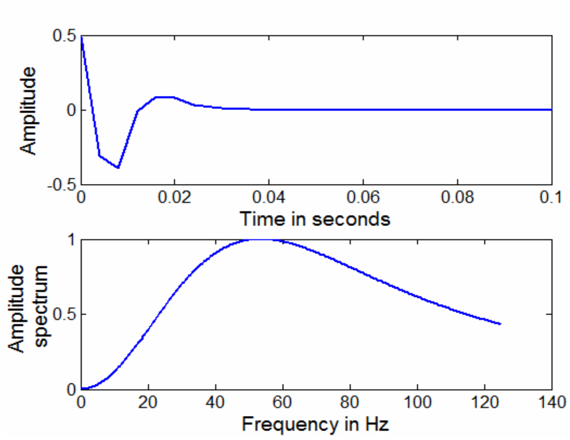

Figure 2.16 Minimum-phase source signature and its amplitude spectrum.

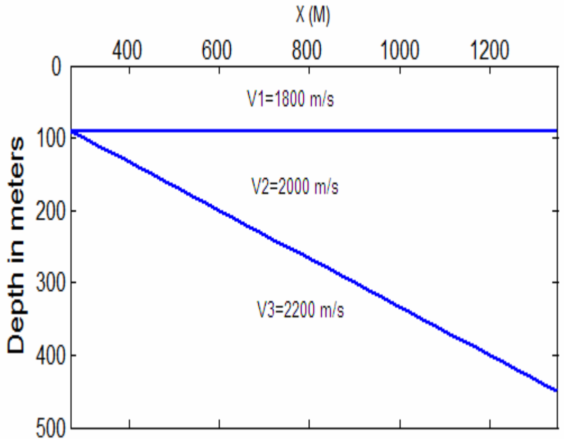

Figure 2.17 A model including a horizontal interface and a dipping reflector.

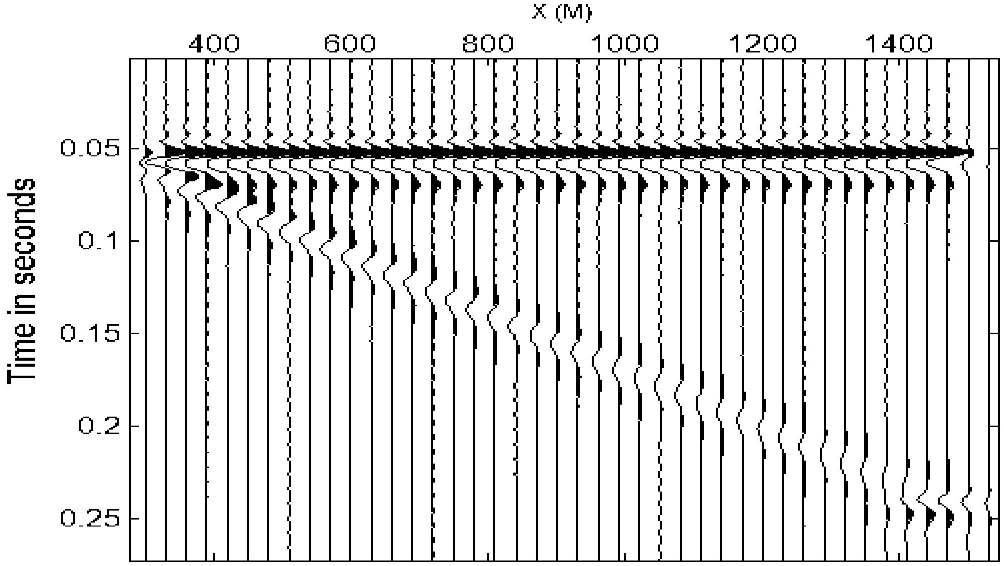

Figure 2.18 Nonstationary wavelet which is zero-offset section. Grid size is 10(m)*10(m) in finite difference computing and Q equals to 40 for all the layers.

2.4 Chapter summary

The constant-Q attenuation causes a loss of high-frequency energy with increasing arrival time and also a time-varying distortion of wavelet phase. This process has been simulated with three methods: the inhomogeneous wavelet simulation by complex ray tracing in a simple constant-Q attenuation medium, zero-offset VSP seismic wavefield extrapolation in a horizontally many layered constant-Q medium, and the frequency-space domain 45-degree wave equation extrapolation in a 2-D viscoacoustic medium. The amplitude spectra of the simulated wavelets show that the high frequency components decay exponentially with increasing frequency. The attenuation factor was introduced into the wave propagation by replacing the frequency-independent velocity for the frequency-dependent phase velocity or complex velocity. Therefore, the phase dispersion causes the phase variation of the wavelet toward minimum phase with increasing traveltime, which will be verified by real VSP data in Chapter 5. All these methods extend the stationary wavelet traveling in an elastic medium to the nonstationary wavelet propagating in a constant-Q medium.

CHAPTER 3 NONSTATIONARY WAVELET ESTIMATION

Unlike stationary deconvolution, nonstationary deconvolution requires different operators at different traveltime. Otherwise some parts of the deconvolved trace will be over compressed while the other parts of the traces are less compressed. Figure 3.1, shows what will happen if we deconvolve an attenuated trace with a stationary operator. The attenuated trace displayed in the bottom of the figure was produced by the complex ray method in horizontally layered media with a constant-Q attenuation. The deconvolution operator is designed within each window denoted by W1, W2, W3 and W4. Applying each operator to the whole trace respectively, we observed that the pulse is best compressed with the operator derived from the pulse itself. The pulses at earlier time are over compressed while those at later time are less compressed. The best results are shown in the oval displayed in Figure 3.1 in which the attenuated pulses are compressed into spikes. So it is clear that if we can accurately estimate and deconvolve the nonstationary wavelets, the resolution of the seismic trace can be truly improved.

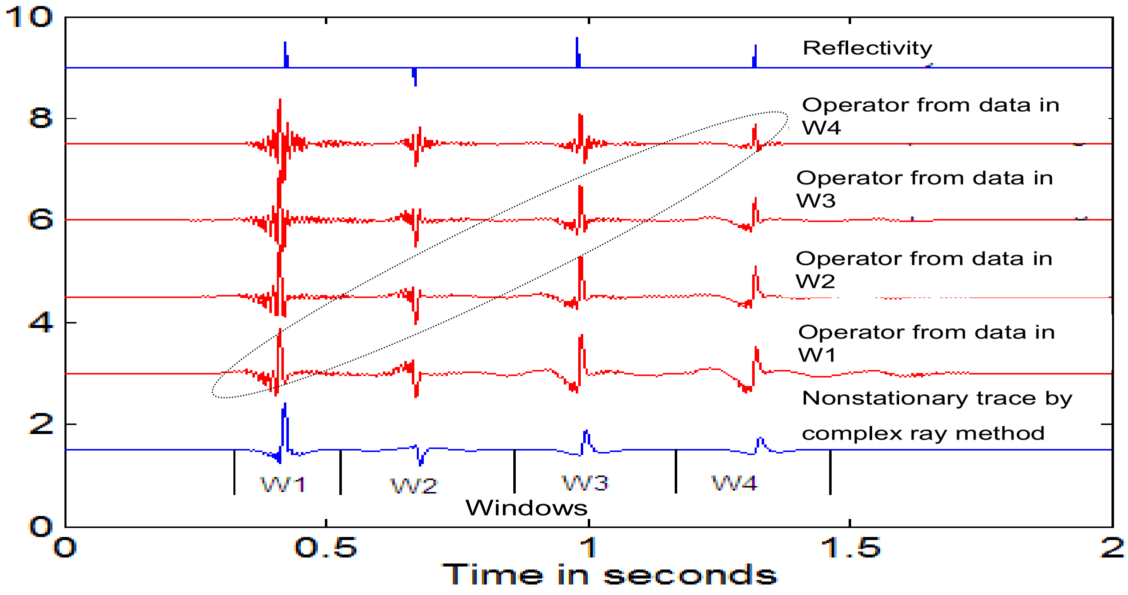

Figure 3.1 A simple attenuated trace, stationary convolved trace and reflectivity. The pulses are less compressed.

The key step in nonstationary deconvolution is how to estimate the nonstationary wavelets. At first we need to consider the assumptions in wavelet estimation. Although the nonstationary wavelet is closer to the real wavelet than the stationary one, it is still a theoretical model. All the assumptions made in the stationary wavelet estimation, except that of stationarity, are required in the nonstationary wavelet estimation. These assumptions include (Yilmaz, 1987)

1. The compressional plane wave impinges on layer boundaries at normal incidence. This means the wavelet estimation is a 1-D inversion problem.
2. The wavelet is temporally short or equivalently it has smooth amplitude spectrum.
3. Reflectivity is a random process. It implies that the seismogram and the seismic wavelet have similar autocorrelations and amplitude spectra. We hope that we can estimate the amplitude spectrum of the wavelet by smoothing the amplitude spectrum of the seismogram because the smoothed amplitude spectrum of the reflectivity is roughly constant.
4. The seismic wavelet is zero or minimum phase. Therefore we can recover the phase of the wavelet estimate from its amplitude spectrum, usually by Hilbert transform.

In addition to these assumptions, nonstationary wavelet estimation further requires that these above assumptions are satisfied within the specified window and the wavelet changes very little within the window. So the stationary deconvolution methods can be used in the nonstationary wavelet estimation from the windowed data.

In Section 3.1, two seismic traces, one from a dynamite source and the other from a vibroseis source, will be generated from the nonstationary convolution model, and will be used in wavelet estimation. Section 3.2 will focus on the wavelet estimation by the multi-window Wiener deconvolution. Section 3.3 will talk about the wavelet estimation by multi-window frequency domain spiking deconvolution. In Section 3.4 the wavelet estimation by Gabor deconvolution will be investigated. Section 3.5 will show the wavelet estimates and then compare them with the given wavelets imbedded in the synthetic trace. Finally, in Section 3.6 the wavelet estimates from the trace with vibroseis source will be discussed.

3.1 Synthetic nonstationary trace

The nonstationary trace can be expressed by (Margrave, 1998)

$$\hat{x}(\omega) = \hat{w}(\omega)\int \alpha(\tau,\omega) r(\tau) e^{-i\omega\tau} d\tau , \qquad (3.1)$$

where $\hat{x}(\omega)$ and $\hat{w}(\omega)$ are the Fourier spectra of the trace and the source signature, r is reflectivity, and α is the time and frequency dependent attenuation function defined by equation (1.15). The time domain nonstationary trace from a given source can be obtained by an inverse Fourier transform to equation (3.1), which can be written as

$$x_d(t) = \frac{1}{2\pi}\int \hat{w}(\omega)\left[\int \alpha(\tau,\omega) r(\tau) e^{-i\omega\tau} d\tau\right] e^{i\omega t} d\omega , \qquad (3.2)$$

where x_d denotes the synthetic nonstationary trace in time domain. Equation (3.2) can also be written as

$$x_d(t) = \int r(\tau)\left[\frac{1}{2\pi}\int \hat{w}(\omega)\alpha(\tau,\omega) e^{i\omega(t-\tau)} d\omega\right] d\tau = \int r(\tau) w_\alpha(t-\tau,\tau) d\tau , \qquad (3.3)$$

which is the nonstationary convolution of the nonstationary wavelet, w_α , and the reflectivity.

Figure 3.2 shows the procedure of the trace creation in the time domain as equation (3.3). The trace was generated by using a minimum-phase source signature with the dominant frequency equal to 50 Hz and quality factor being 50. The reflectivity is obtained from the real log data.

The other trace was generated to simulate the vibroseis signal. Following the physical procedure of the real vibroseis seismogram, first the sweep was attenuated in an anelastic medium. Like the nonstationary wavelet defined in equation (3.3), a constant-Q attenuated sweep is calculated by

$$w_{sweep}(t-\tau,\tau) = \frac{1}{2\pi}\int \hat{s}_{sweep}(\omega)\alpha(\tau,\omega) e^{i\omega(t-\tau)} d\omega , \qquad (3.4)$$

where w_{sweep} is attenuated sweep and $\hat{s}_{sweep}$ is the Fourier spectrum of the pilot sweep. The second step carried out the nonstationary convolution between the attenuated sweep and the the reflectivity, which is expressed by

$$x_{rec}(t) = \int w_{sweep}(t-\tau,\tau) r(\tau) d\tau, \tag{3.5}$$

where $x_{rec}(t)$ is a model for uncorrelated vibroseis data. Finally the correlated vibroseis trace was produced by

$$x_{v}(t) = \int x_{rec}(t+\tau) s_{sweep}(\tau) d\tau, \tag{3.6}$$

which is the cross-correlation between uncorrelated vibroseis data and the pilot sweep.

Figure 3.3 shows that the uncorrelated vibroseis trace is the nonstationary convolution of the attenuated sweep and the reflectivity. Figure 3.4 shows the nonstationary trace is the cross-correlation of the uncorrelated data and the pilot sweep.

The nonstationary wavelet from a vibroseis source can be generated by

$$w_{\alpha}(t-\tau,\tau) = \int w_{sweep}(t-\tau+t',\tau) s_{sweep}(t') dt', \tag{3.7}$$

which is the cross-correlation of the attenuated sweep, $w(t'-\tau,\tau)$ and the pilot sweep. The procedure for the generation of the nonstationary wavelet is shown in Figure 3.5.

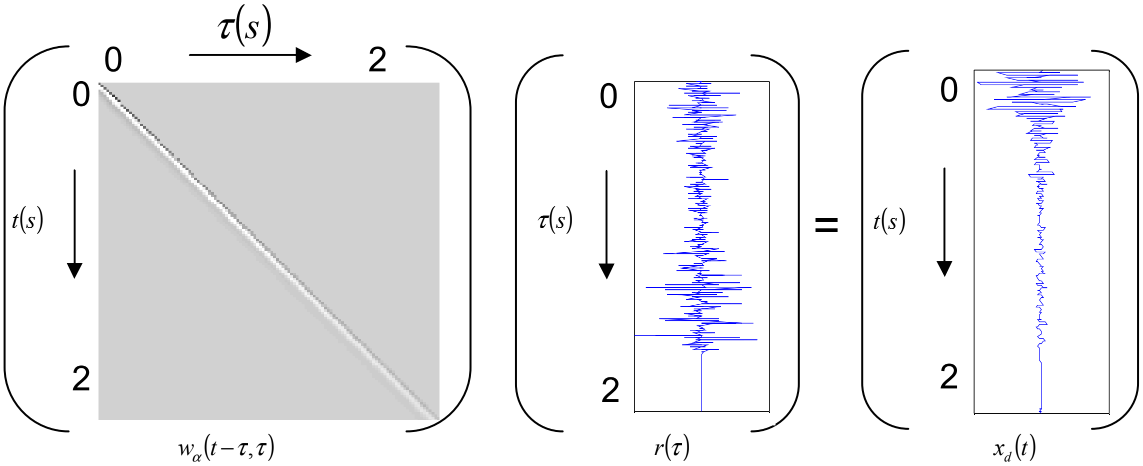

Figure 3.2 Synthetic nonstationary trace by the nonstationary convolution of nonstationary wavelet and reflectivity (Adapted from Margrave (1998)).

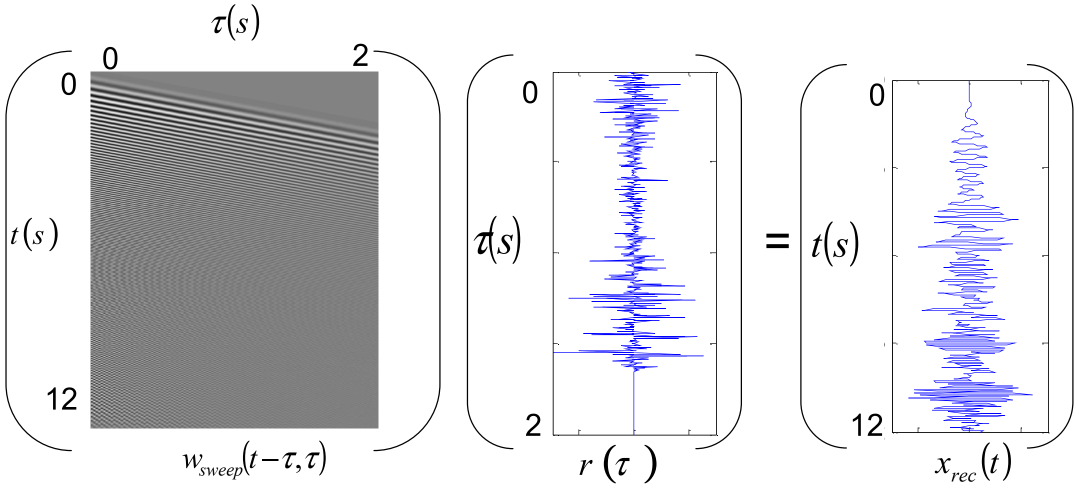

Figure 3.3 Uncorrelated vibroseis signal (right) is the nonstationary convolution of the nonstationary sweep (left) and reflectivity (middle).

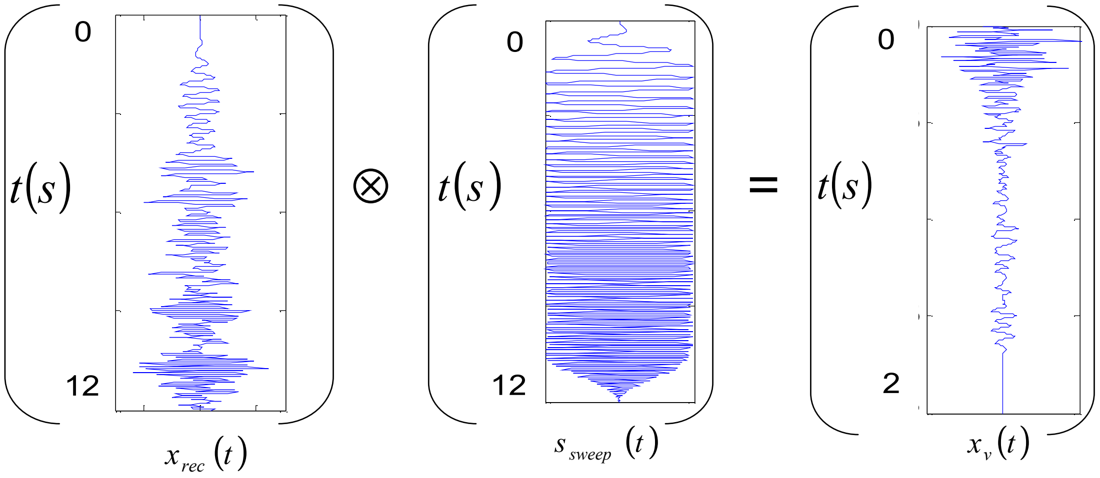

Figure 3.4 The correlated vibroseis trace (right) is the cross-correlation of the received seismic signal (left) and the pilot sweep (middle).

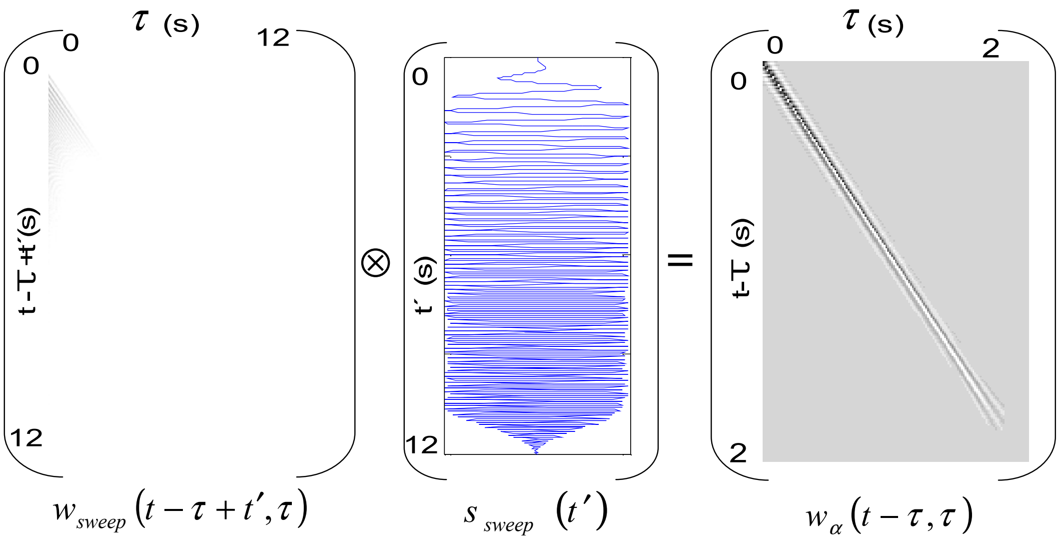

Figure 3.5 Nonstationary wavelet is the cross-correlation between the nonstationary sweep and pilot sweep.

To examine the phase property of the nonstationary wavelet simulated from the vibroseis source, we applied Wiener deconvolution to the nonstationary wavelet shown in Figure 3.5. If the result is close to a zero-phase spike, we can infer that the wavelet approximates to minimum phase. Figure 3.6 shows the selected wavelets and the output of the Wiener deconvolution. Operator length in Wiener deconvolution is 0.16 s and the stabilization factor is 0.0001. Figures 3.6 (a) and 3.6 (b) show the simulated vibroseis wavelets and deconvolved wavelets. The output of the deconvolution is close to the band limited zero-phase spike. Thus we believe that the simulated nonstationary wavelet from the vibroseis source signature approximates to the minimum phase.

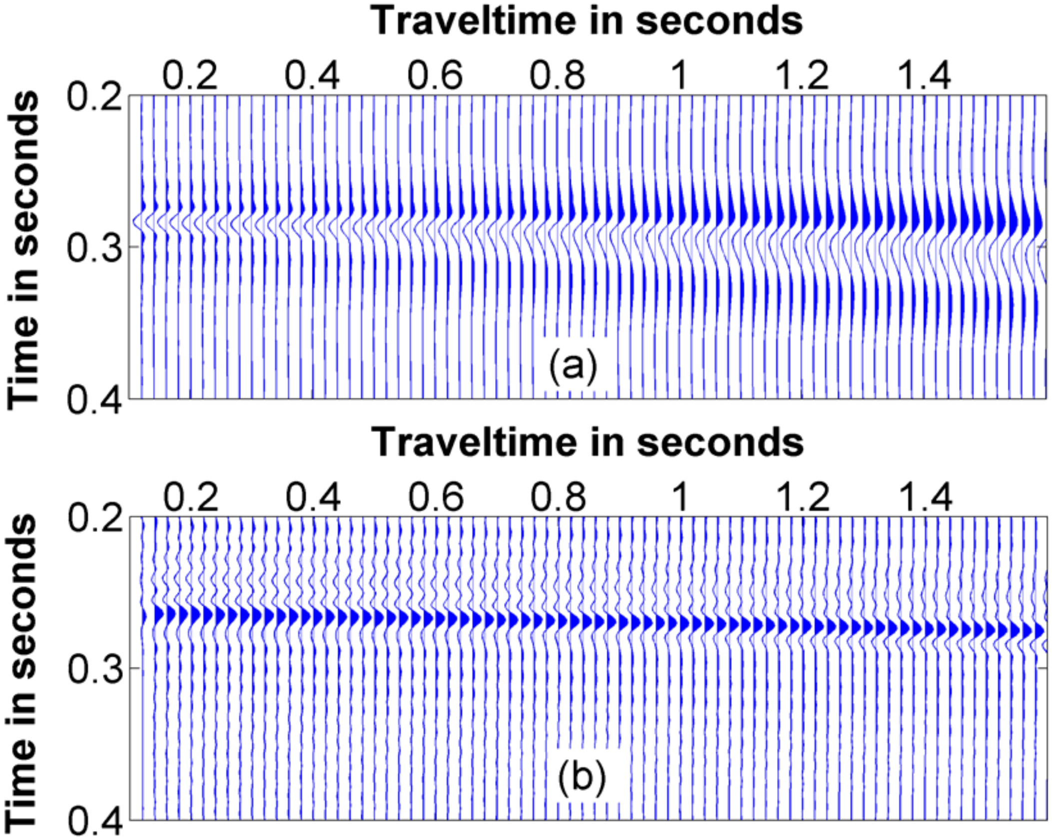

Figure 3.6 Simulated wavelets from a vibroseis source (a) and the output of the Wiener spiking deconvolution (b).

3.2 Nonstationary wavelet estimation by multi-window Wiener deconvolution

This is a theoretical, numerical simulation of standard industry practice. Before deconvolution, the trace is windowed with a boxcar and gained by AGC method. We assume that the wavelet estimate represents the average wavelet in the window. Within each window the Wiener-Levinson algorithm is used twice for solving two normal equations. In the n^{th} window, the first equation is

$$\begin{bmatrix} \phi_n(0)+\varepsilon & \phi_n(1) & \cdots & \phi_n(L-1) \\ \phi_n(1) & \phi_n(0)+\varepsilon & \cdots & \phi_n(L-2) \\ \vdots & \vdots & \ddots & \vdots \\ \phi_n(L-1) & \phi_n(L-2) & \cdots & \phi_n(0)+\varepsilon \end{bmatrix} \begin{bmatrix} a_n(0) \\ a_n(1) \\ \vdots \\ a_n(L-1) \end{bmatrix} = \begin{bmatrix} 1 \\ 0 \\ \vdots \\ 0 \end{bmatrix}, \tag{3.8}$$

where $\phi_n(\tau)$ is autocorrelation of the seismic data within the n^{th} window , which is given by

$$\phi_n(\tau) = \sum_{t=0}^{T-1} x_n(t) x_n(t+\tau), \quad \tau = 0,1,2...L-1, \tag{3.9}$$

where T is the length of the trace segment to be used for operator design and L is operator length. x_n denotes the seismic data in the window. After solving equation (3.8), the deconvolution operator, a_n , can be obtained and then be used for estimating the wavelet by equation

$$\begin{bmatrix} \psi_n(0)+\varepsilon & \psi_n(1) & \cdots & \psi_n(L-1) \\ \psi_n(1) & \psi_n(0)+\varepsilon & \cdots & \psi_n(L-2) \\ \vdots & \vdots & \ddots & \vdots \\ \psi_n(L-1) & \psi_n(L-2) & \cdots & \psi_n(0)+\varepsilon \end{bmatrix} \begin{bmatrix} w_n(0) \\ w_n(1) \\ \vdots \\ w_n(L-1) \end{bmatrix} = \begin{bmatrix} 1 \\ 0 \\ \vdots \\ 0 \end{bmatrix}, \tag{3.10}$$

where $\psi_n(\tau)$, the autocorrelation of the deconvolution operator obtained from equation (3.8), is expressed as

$$\psi_n(l) = \sum_{\tau=0}^{L-1} a_n(\tau) a_n(\tau+l), \quad l = 0,1,2...L-1, \tag{3.11}$$

where w_n is the wavelet estimate over the n^{th} window. It should be noticed that the value of stabilization factor, ε, and operator length should be the same in equations (3.8) and (3.10) to maintain consistency in wavelet estimation.

3.3 Nonstationary wavelet estimation multi-window frequency domain spiking deconvolution

Frequency-domain spiking deconvolution is the Fourier equivalent to Wiener deconvolution (Margrave, 2001). Both of them are spiking deconvolution but use different approaches to estimate the wavelet. It is necessary to investigate the differences caused by these approaches. In multi-window, frequency-domain spiking deconvolution, we also assume the wavelet changes very little within a boxcar window and the wavelet estimate represents the average wavelet in this window. The trace was also gained before the deconvolution.

The Fourier amplitude spectrum of windowed data within the n^{th} window can be expressed by

$$\hat{x}_n \approx \hat{g}_n \bullet (\hat{w}_n \hat{r}) = \hat{w}_n (\hat{g}_n \bullet \hat{r}) + [\hat{g}_n \bullet, \hat{w}_n] \hat{r} \ , \tag{3.12}$$

where " $\bullet$ " denotes convolution. $\hat{g}_n$ and $\hat{w}_n$ are the Fourier spectra of the n^{th} boxcar window and the wavelet within this window. $[\hat{g}_n \bullet, \hat{w}_n]\hat{r}$ is called the commutator and can be ignored (Margrave and Lamoureux, 2001) in some cases (it will be further discussed in next section). To estimate the wavelet we need to smooth the Fourier amplitude spectrum of x_n by

$$\overline{|\hat{x}_n|} \approx \hat{B} \bullet |\hat{w}_n (\hat{g}_n \bullet \hat{r})| = |\hat{w}_n| \left[\hat{B} \bullet |\hat{g}_n \bullet \hat{r}|\right] + \left[\hat{B}(\omega) \bullet, |\hat{w}_n|\right] |\hat{g}_n \bullet \hat{r}|, \tag{3.13}$$

where $\hat{B}$ is a boxcar smoother in Fourier domain and $\overline{|\hat{x}_n|}$ denotes the smoothed Fourier amplitude spectrum of the trace within the n^{th} window. Again we ignore the commutator, $\left[\hat{B}(\omega) \bullet, |\hat{w}_n|\right] |\hat{g}_n \bullet \hat{r}|$, and then assume the reflectivity within the window is white. Thus, the smoothed reflectivity is a unit, that is

$$\hat{B} \bullet |\hat{g}_n \bullet \hat{r}| \approx 1, \tag{3.14}$$

and the Fourier amplitude spectrum of the wavelet estimate is

$$|\hat{w}_n|_{est} \approx \overline{|\hat{x}_n|}. \tag{3.15}$$

Under the assumption of minimum-phase wavelet, the phase spectrum can be obtained from the smoothed amplitude spectrum by Hilbert transform

$$\varphi_n(\omega) = \int_{-\infty}^{\infty} \frac{\ln\left(\overline{|\hat{x}_n|} + \mu \max\left(\overline{|\hat{x}_n|}\right)\right)}{\omega - \omega'} d\omega'. \tag{3.16}$$

Finally the wavelet in the n^{th} window can be given by

$$w_n(t) = \frac{1}{2\pi}\int_{-\infty}^{\infty} \overline{|\hat{x}_n|} e^{i\varphi_n(\omega)} e^{i\omega t} d\omega \ . \tag{3.17}$$

3.4 Nonstationary wavelet estimation by Gabor deconvolution

3.4.1 Approximation to Gabor spectrum of the seismic trace

The Gabor spectrum of the seismic trace, $x(t)$, is expressed as (Margrave and Lamoureux, 2001)

$$G[x](\tau,\omega) = \int_{-\infty}^{\infty} x(t) g(t-\tau) e^{-i\omega t} dt \ , \tag{3.18}$$

where g is the Gabor analysis window and τ is the window centre. $x(t)$ is defined in equation (3.2). Equation (3.18) can be factorized as (Margrave et al, 2003)

$$G[x] \approx \hat{g}_\tau \bullet (\hat{w}_\alpha \hat{r}) = \hat{w}_\alpha (\hat{g}_\tau \bullet \hat{r}) + [\hat{g}_\tau \bullet, \hat{w}_\alpha]\hat{r} \ , \tag{3.19}$$

where $[\hat{g}_\tau \bullet, \hat{w}_\alpha]\hat{r}$ is the commutator which is just the difference between applying the operations in one order and then the other. Nonstationary wavelet, $\hat{w}_\alpha$, is defined in equation (1.15). It has been justified that the product of the nonstationary wavelet and Gabor spectrum of the reflectivity is close to the first asymptotic term of the Gabor spectrum of the seismic trace (Margrave and Lamoureux, 2001). Following from equation (3.19) by neglecting the commutator, we have

$$G[x](\tau,\omega) \approx \hat{w}_\alpha(\tau,\omega) G[r](\tau,\omega) \, . \tag{3.20}$$

An example for approximation to a Gabor amplitude spectrum of the attenuated seismic trace is shown in Figure 3.7 where .X is a symbol of pointwise multiply.

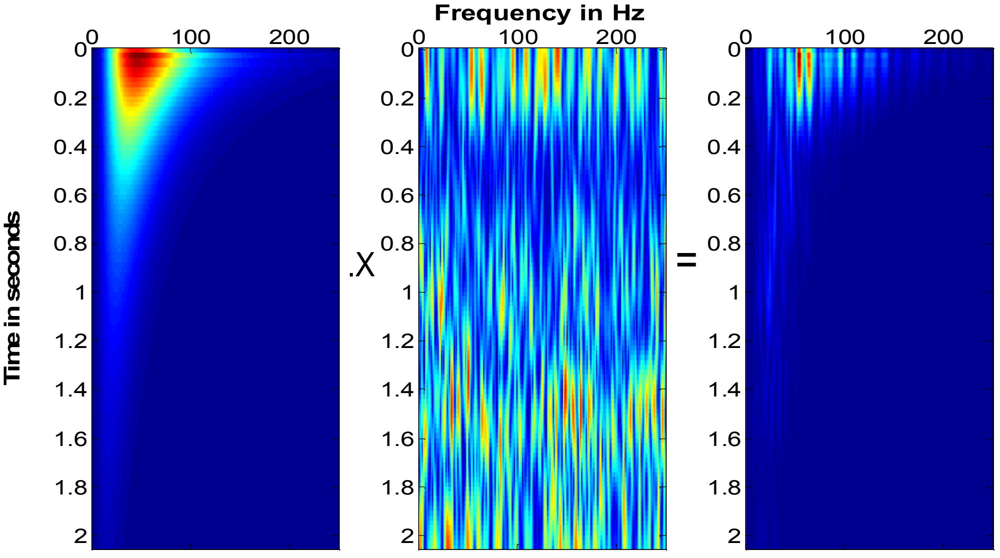

$\left|\hat{w}_\alpha(\tau,\omega)\right|$ $\left|G[r](\tau,\omega)\right|$ $\left|\hat{w}_\alpha(\tau,\omega)G[r](\tau,\omega)\right|$

Figure 3.7 Gabor amplitude spectrum of the seismic trace is close to the product of the time-frequency domain amplitude spectrum of the nonstationary wavelet and the Gabor amplitude spectrum of the reflectivity.

Given the source signature, the attenuation function and the reflectivity, we can calculate the Gabor amplitude spectrum of the seismic trace, $\left|\hat{g}_\tau \bullet (\hat{w}_\alpha \hat{r})\right|$, and its approximation, $\left|\hat{w}_\alpha (\hat{g}_\tau \bullet \hat{r})\right|$. Figures 3.8 (a) shows Gabor amplitude spectrum of the seismic trace. Here the half width of the Gaussian window is 0.2 s and Q in the attenuation function is 50. The source signature is a minimum-phase wavelet with dominant frequency being 50 Hz. Figures 3.8 (b) shows Gabor amplitude spectrum of the approximation that is the same figure as shown in Figure 3.7. The shape of the amplitude spectra in Figures 3.8 (a) and (b) is very similar, which means equation (3.20) is accurate in this case. Figure 3.8 (c) shows the absolute value of the commutator, which is much less than that shown in Figure 3.8 (a) or (b) at the same position.

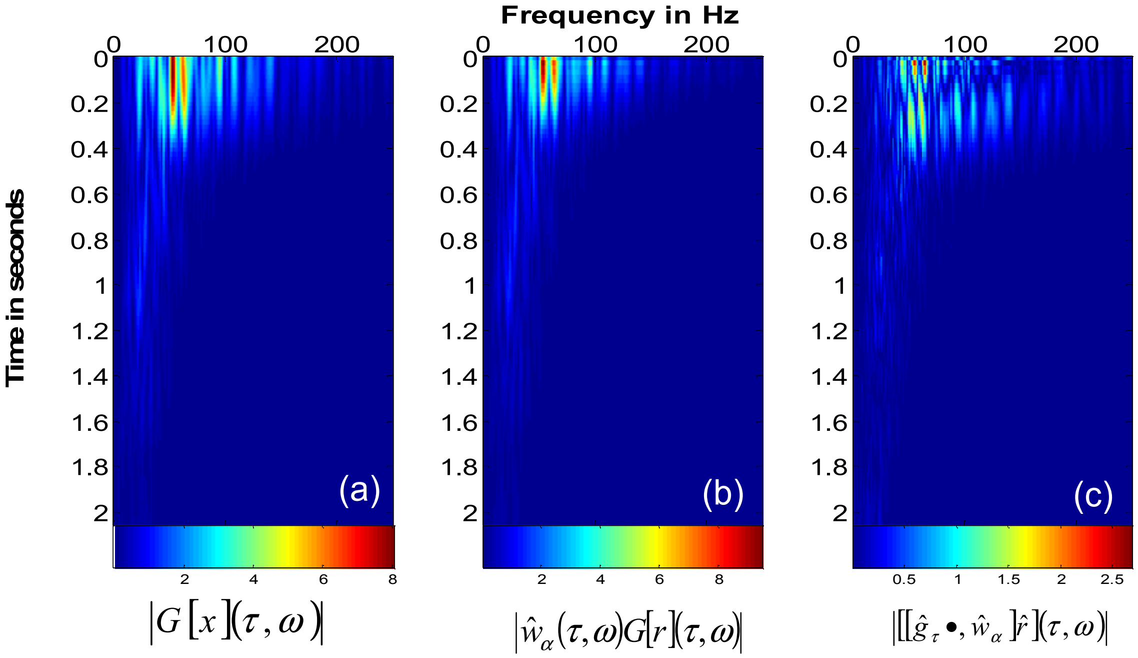

Figure 3.8 Gabor amplitude spectrum of the seismic trace (a), approximation to the Gabor amplitude spectrum of the seismic trace (b) and the absolute value of the commutator (c).

The accuracy of the equation (3.20) depends on the commutator which varies with the window length and Q (Margrave et al., 2003). The ratio of the commutator energy and the total energy can be written as

$$D(Q,l)=\frac{\sqrt{\sum_{l}\sum_{Q}\left(\left|\hat{g}_\tau \bullet (\hat{w}_\alpha \hat{r}) - \hat{w}_\alpha (\hat{g}_\tau \bullet \hat{r})\right|\right)^2}}{\sqrt{\sum_{l}\sum_{Q}\left(\left|\hat{g}_\tau \bullet (\hat{w}_\alpha \hat{r})\right|\right)^2}}, \tag{3.21}$$

where l is the half width of the Gaussian window. τ denotes window center time.

Figure 3.9 shows the total energy, the commutator energy and the ratio of the commutator energy and the total energy, $D(Q,l)$, varying with different Q and the half width of the window, l. With the small Q, the commutator energy decreases with increasing window length. Since the total energy decreases more quickly than the commutator energy, the ratio of the energy tends to increase with the increasing window width. It is observed that for a big Q there is an optimal window length.

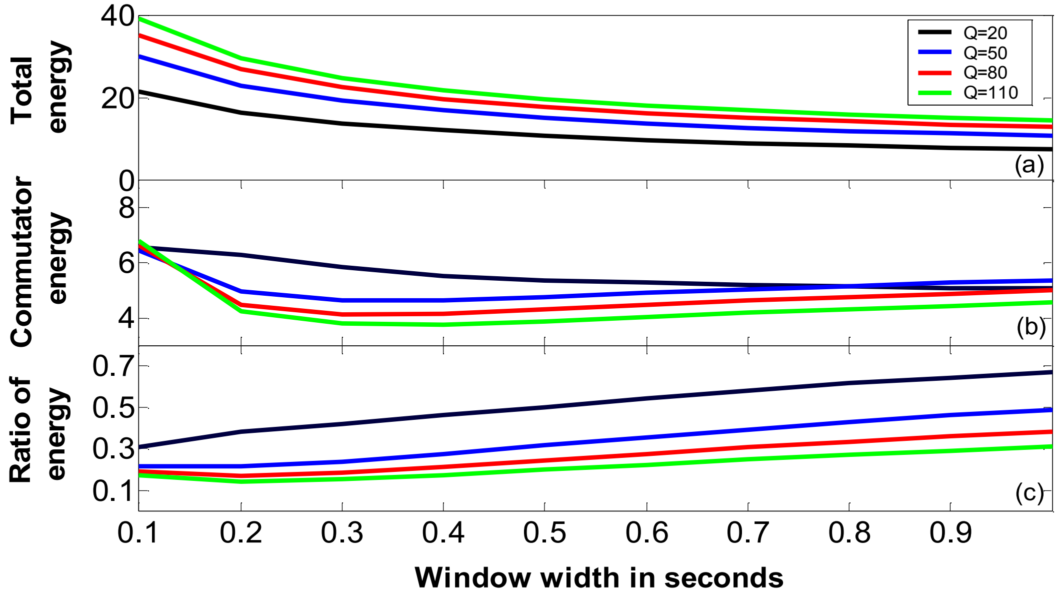

Figure 3.9 The total energy (a), the commutator energy (b) and the ratio of the commutator energy and the total energy (c).

3.4.2 Nonstationary wavelet estimation by Gabor deconvolution

The main idea in nonstationary wavelet estimation is the factorization of $|G[x](\tau,\omega)|$ into $|\hat{w}_\alpha(\tau,\omega)|$ and $|G[r](\tau,\omega)|$. The key step in the factorization is smoothing $|G[x](\tau,\omega)|$ under the assumption of white reflectivity. Different smoothers will result in different wavelet estimates. Here we investigate two smoothers, boxcar and hyperbolic smoothers, for wavelet estimation.

Smoothing a Gabor amplitude spectrum of a seismic trace by a 2-D boxcar can be expressed as

$$\overline{|G[x]|} \approx B \bullet |\hat{w}_\alpha G[r]| = |\hat{w}_\alpha| \hat{B} \bullet |G[r]| + \left[\hat{B}\bullet, |\hat{w}_\alpha|\right] |G[r]|, \tag{3.22}$$

where

$$\hat{B}(\tau,\omega) = \begin{cases} 1 & |\tau| \le \tau_0, |\omega| \le \omega_0 \\ 0 & |\tau| > \tau_0, |\omega| > \omega_0 \end{cases}, \tag{3.23}$$

here τ_0 and ω_0 are the boxcar lengths in the time and the frequency domain. If we ignore the commutator, $\left[\hat{B}\bullet, |\hat{w}_\alpha|\right]|G[r]|$, and assume the Gabor spectrum of the reflectivity is white, the smoothed Gabor amplitude spectrum of the reflectivity is approximately unity and the Gabor amplitude spectrum of the wavelet estimate can be written as

$$\left|\hat{w}_\alpha(\tau,\omega)\right|_{est} \approx \overline{\left|G[x](\tau,\omega)\right|}. \tag{3.24}$$

Under the assumption of minimum phase, the phase spectrum of the wavelet estimate can be calculated by the Hilbert transform

$$\varphi(\tau,\omega) = \int_{-\infty}^{\infty} \frac{\ln \overline{\left|G[x](\tau,\omega)\right|}}{\omega-\omega'} d\omega'. \tag{3.25}$$

Thus, the nonstationary wavelet in the time-frequency domain is expressed as

$$\hat{w}_{est}(\tau,\omega) \approx \overline{\left|G[x](\tau,\omega)\right|} e^{i\varphi(\tau,\omega)}, \tag{3.26}$$

where $\hat{w}_{est}(\tau,\omega)$ denotes the nonstationary wavelet estimate.

Unlike the boxcar smoother, the hyperbolic smoothing method attempts to estimate both the magnitude of the attenuation function and the source signature from Gabor spectrum of seismic trace. Following the procedure provided by Iliescu and Margrave (2002), given a family of hyperbolae

$$\omega\tau = k \quad , k = 1,2,3....K, \tag{3.27}$$

where k is constant with respect to α and τ . The magnitude of attenuation function estimate is expressed as

$$\left|\alpha(k)\right|_{est} = \frac{\int_0^{\omega_N} \left|G[x](k/\omega,\omega)\right| d\omega}{l_k}, \tag{3.28}$$

where l_k represents the length of the k^{th} hyperbola and ω_N denotes the Nyquist frequency. Substituting equations (3.20) and (1.15) into equation (3.28) yields

$$\left|\alpha(k)\right|_{est} = \frac{e^{-\frac{k}{2Q}} \int_0^{\omega_N} \left|\hat{w}(\omega)\right| \left|G[r](k/\omega,\omega)\right| d\omega}{l_k} = \rho(k) e^{-\frac{k}{2Q}}, \tag{3.29}$$

where $\rho(k)$ represents the error in the attenuation function estimate. It depends on the result of the integral in equation (3.29). Under the assumption of stationary source signature and white reflectivity, this integral will change with k very little. Thus, we have

$$\rho(k) \approx \rho_0 = \text{constant}. \tag{3.30}$$

Therefore the magnitude of the attenuation function estimate can be approximated as

$$\left|\alpha(\tau,\omega)\right|_{est} = \left|\alpha(\omega\tau)\right|_{est} = \rho_0 e^{-\frac{k}{2Q}}. \tag{3.31}$$

The Gabor amplitude spectrum of the source signature estimate is given by (Iliescu and Margrave, 2002)

$$\left|\hat{w}(\omega)\right|_{est} = \frac{1}{\tau_{\max}} \int_0^{\tau_{\max}} \frac{\left|G[x](\tau,\omega)\right|}{\left|\alpha(\tau,\omega)\right|_{est}} d\tau \ , \tag{3.32}$$

which means the amplitude spectrum of the source signature estimate is equal to the time average of the ratio between the Gabor spectrum of the trace and the estimated attenuation function. Then $\left|\hat{w}(\omega)\right|_{est}$ is further smoothed by

$$\overline{\left|\hat{w}(\omega)\right|}_{est} = \left|\hat{w}(\omega)\right|_{est} * B(\omega), \tag{3.33}$$

where $B(\omega)$ is a boxcar smoother in frequency domain. Finally the Gabor amplitude spectrum estimate of nonstationary wavelet is given by

$$\left|\hat{w}_\alpha(\tau,\omega)\right|_{est} \approx \left|\alpha(\tau,\omega)\right|_{est} \overline{\left|\hat{w}(\omega)\right|}_{est}. \tag{3.34}$$

Under the minimum phase assumption, the Gabor spectrum of the nonstationary wavelet estimate can be expressed as

$$\hat{w}_{est}(\tau,\omega) = \left|\hat{w}_\alpha(\tau,\omega)\right|_{est} e^{iH\left[\left|\hat{w}_\alpha(\tau,\omega)\right|_{est}\right]} , \tag{3.35}$$

here H denotes Hilbert transform.

3.5 Comparison of the wavelet estimates and simulated wavelets

The synthetic trace was the convolution of the nonstationary wavelet and the reflectivity. Thus the closer the wavelet estimate to this simulated nonstationary wavelet, the more accurate the wavelet estimate is. In this section, four methods shown in Sections 3.2, 3.3 and 3.4 were applied for wavelet estimates from the same synthetic trace displayed in Figure 3.2. The wavelet estimates were compared with the simulated wavelets as shown in Figure 3.10 to evaluate the accuracy of each method. In Figure 3.10, every eighth wavelet is shown while the amplitude spectra of all the wavelets are shown for better display. As the traveltime increases the various frequency components that constituted original source signature have been attenuated differently and have traveled at different speeds. The dominant frequency of the simulated nonstationary wavelet becomes lower with increasing traveltime and the phase relationships amongst the frequency components change.

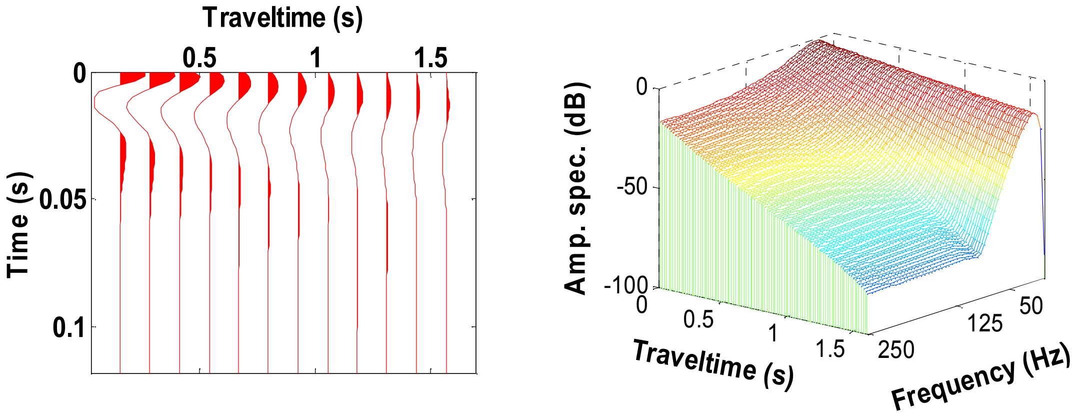

Figure 3.10 Simulated wavelets (left) and their Fourier amplitude spectrum (right). Only every eighth wavelet is shown while the amplitude spectra of all the wavelets are shown for display purposes.

3.5.1 Wavelet estimates from the multi-window Wiener deconvolution methods

Like the conventional deconvolution procedure, the multi-window time-domain Wiener deconvolution and the multi-window frequency-domain spiking deconvolution (frequency domain Wiener deconvolution) were done on the gained data in temporal boxcar window that was moved down the trace in increments.

Figure 3.11 shows the wavelet estimates and the Fourier amplitude spectrum estimates from the time-domain Wiener deconvolution. Since the trace was gain corrected with AGC before wavelet estimation, the amplitude of the wavelet estimate does not decay with the increasing traveltime. The high frequency components shown in the simulated wavelets were not properly recovered in the wavelet estimates. For both the wavelet estimates and simulated wavelets the dominant frequency decreases as the traveltime increases.

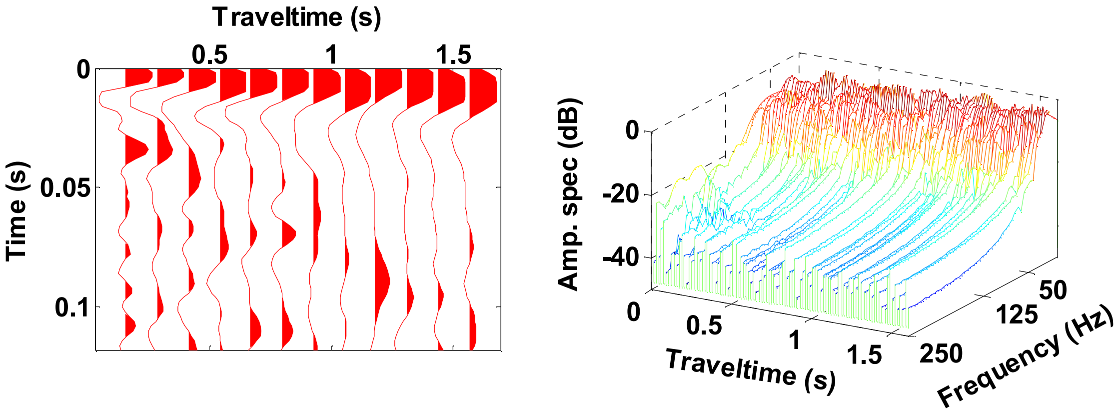

Figure 3.11 Wavelets (left) and their Fourier amplitude spectrum (right) by the multi-window Wiener deconvolution.

Figure 3.12 shows the wavelet estimates and the amplitude spectrum estimates by the multi-window frequency spiking deconvolution. This method is equivalent to the multi-window time-domain Wiener deconvolution. The same parameters such as stabilization factor and window length were used in both approaches. Thus, the wavelet estimates from the frequency-domain spiking deconvolution are close to those from the time-domain Wiener deconvolution while the amplitude spectra of the former change more smoothly than those of the latter.

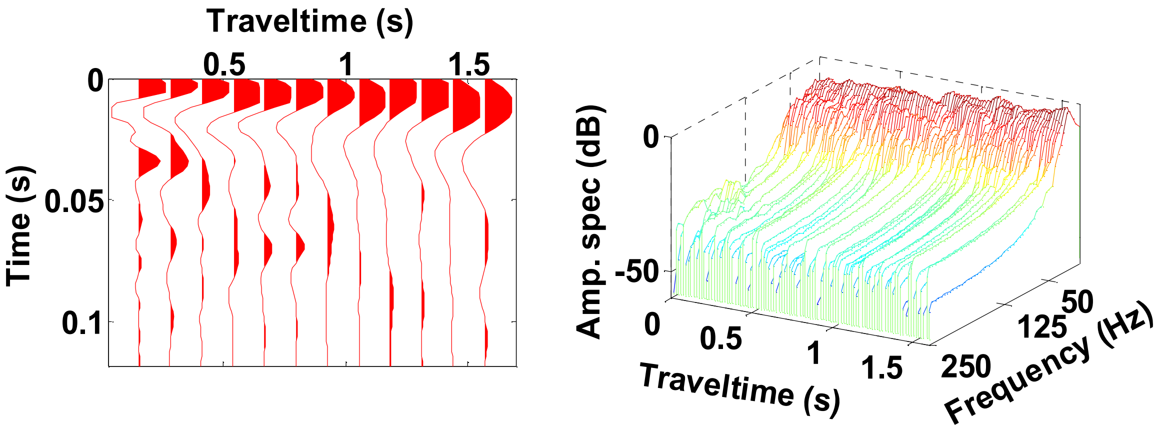

Figure 3.12 Wavelets (left) and their Fourier amplitude spectrum (right) by the multi-window frequency domain spiking deconvolution.

3.5.2 Wavelet estimates by the Gabor deconvolution

The Gabor deconvolution was done on the data without gaining because its algorithm includes a gaining operation. To estimate wavelets with Gabor deconvolution, both the boxcar and the hyperbolic smoothers are applied. With the boxcar smoother, we apply the Gabor transform using Gaussian windows with a 90 percent window overlap, and then smooth the Gabor amplitude spectrum by a time-frequency domain boxcar to estimate the Gabor amplitude spectrum of the wavelet estimate. In the hyperbolic smoothing method, we smooth the Gabor magnitude spectrum of the seismic trace along hyperbolae ($t \bullet f$ =constant) to estimate the magnitude of the attenuation function. The source signature is then estimated by dividing the Gabor amplitude spectrum by the attenuation estimates, and averaging over time. The Gabor amplitude spectrum of the wavelet estimate is the production of the attenuation surface and the amplitude spectrum of the source signature estimate. A Hilbert transform over frequency at constant time, applied to the logarithm of the Gabor amplitude spectrum of the wavelet estimates, provides the associated minimum phase estimate.

Figure 3.13 shows the wavelet estimates and the amplitude spectra by Gabor deconvolution with a time-frequency domain boxcar smoother. Here the frequency components within 10 dB are close to those of the simulated wavelets but the gain is not exactly same as that in the simulated wavelets. The difference in the gain depends on the window width and the smoother length (which will be further discussed in next Chapter). The high frequency components are also enhanced especially at an early time, but are not high enough to the level as shown in the amplitude spectra of the simulated wavelets.

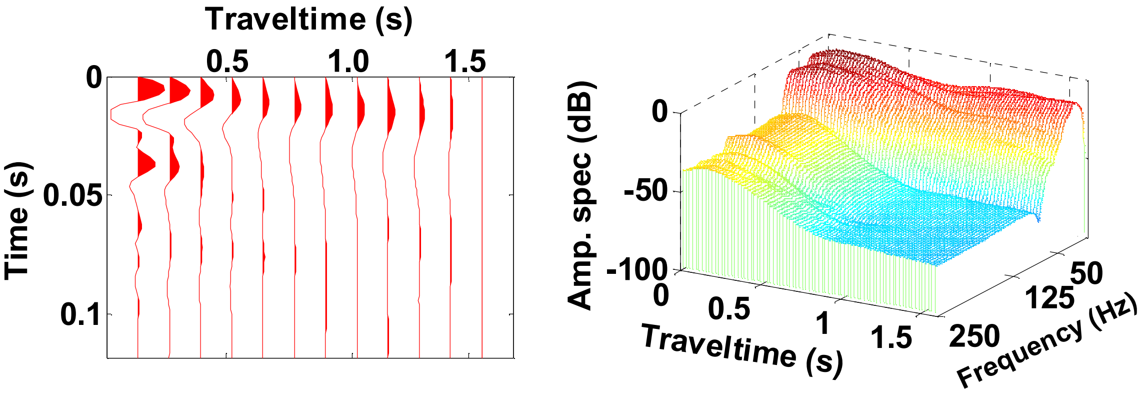

Figure 3.13 Wavelets (left) and their Fourier amplitude spectrum (right) by Gabor deconvolution with boxcar smoother.

Figure 3.14 shows the wavelet estimates and the amplitude spectra by the Gabor deconvolution with a hyperbolic smoother. The amplitude variation of the wavelet estimates is very close to that of the simulated wavelets and the amplitude spectrum estimates are the best approximation to the amplitude spectra of the simulated wavelets.

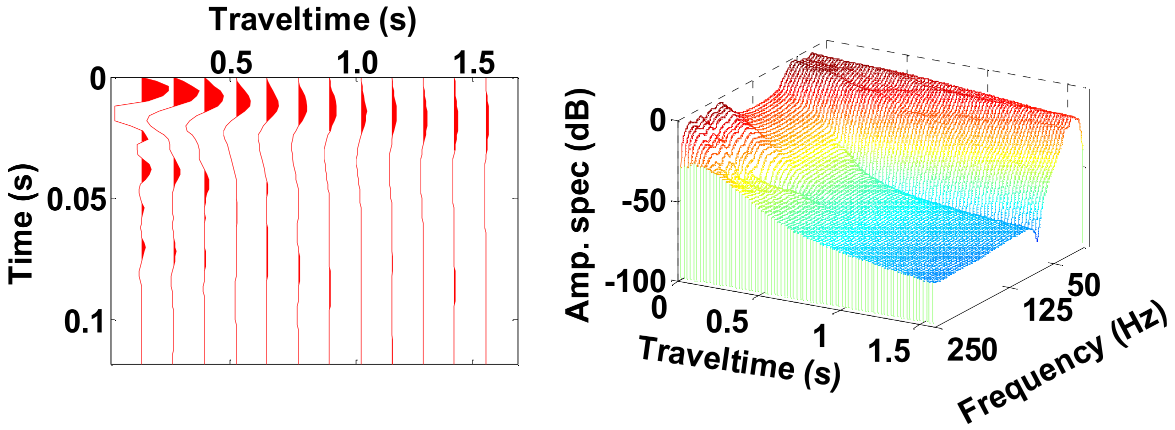

Figure 3.14 Wavelets (left) and their Fourier amplitude spectrum (right) by Gabor deconvolution with hyperbolic smoother.

Figure 3.15 shows cross-correlations of the wavelet estimates from four deconvolution methods with the simulated wavelets. It is shown that the wavelets estimated by Gabor deconvolution are most similar to the simulated wavelets but with a little bit phase shift shown by the lags of maximum cross-correlation.

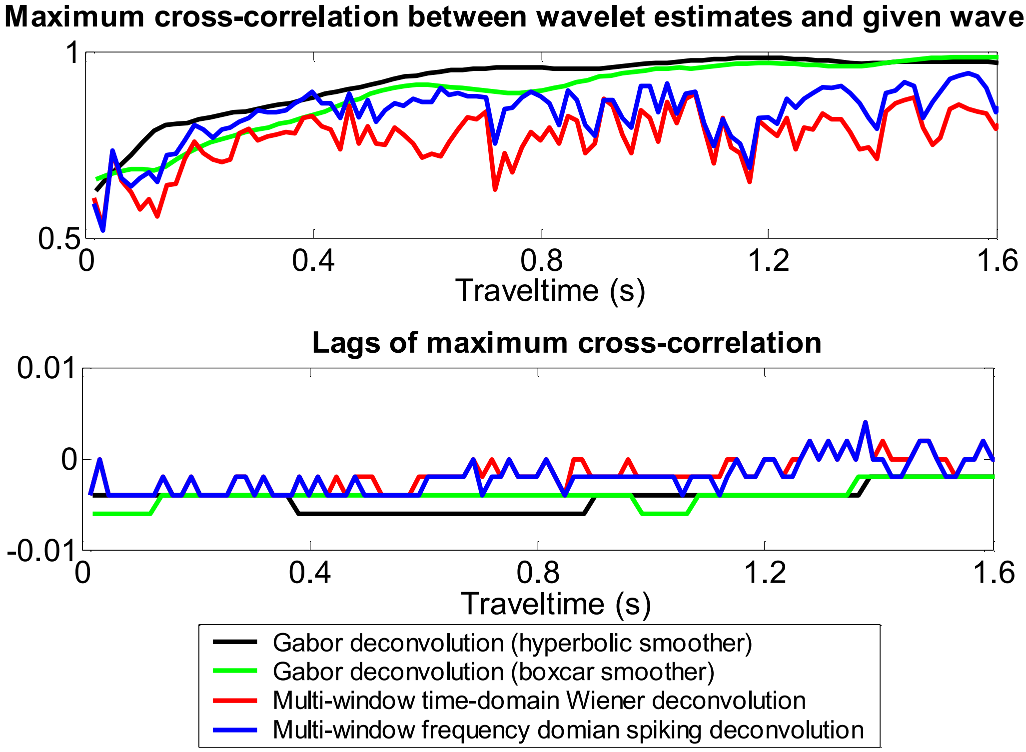

Figure 3.15 Normalized maximum cross-correlations between wavelet estimates and simulated wavelets (top), and the lags of the maximum cross-correlation (bottom).

3.6 Vibroseis wavelet estimation by the Gabor deconvolution

As showed in Section 3.1, the wavelets recorded in VSP downgoing waves from a vibroseis source are approximately minimum-phase. Here we apply the minimum-phase nonstationary deconvolution to estimate the wavelets from the synthetic trace shown in Figure 3.4.

Figure 3.16 shows the Gabor amplitude spectrum of the nonstationary wavelet estimate from the synthetic trace shown in Figure 3.4, and the Fourier amplitude spectra of the simulated nonstationary wavelet shown in Figure 3.5. After 0.5 s, these two spectra are roughly similar to each other. Figure 3.17 shows the wavelet estimates from Gabor and multi-window Wiener deconvolution. The trace was gained with 0.1s length AGC before the Wiener deconvolution and the wavelet estimates were rescaled with the same AGC function. Gabor deconvolution includes the gain effect in its algorithm so that this approach was directly applied to the synthetic trace. The given wavelets are also shown in the figure. At an earlier time, the wavelet estimates show a different waveform from the given wavelets, but they gradually resemble each other at later time. The similarity between the wavelet estimates and the given wavelets is also shown in the maximum crosscorrelation displayed in the bottom of the Figure 3.17. The wavelet estimates from Gabor deconvolution are closer to the input wavelets than those from the Wiener deconvolution at later time.

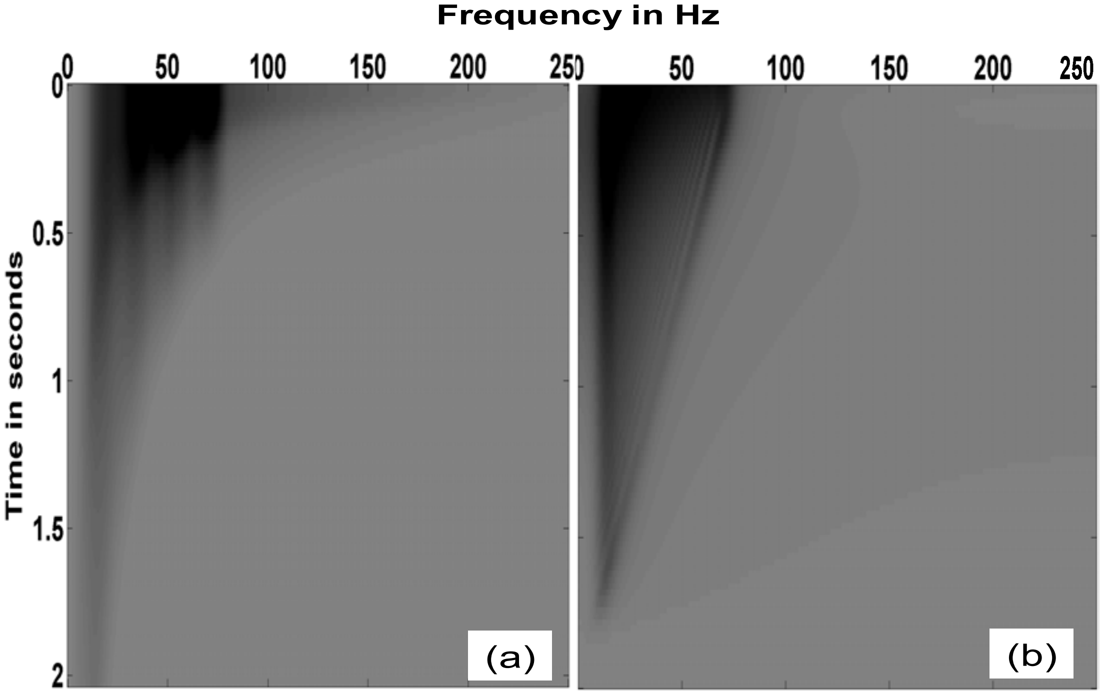

Figure 3.16 Gabor spectrum of the nonstationary wavelet estimate (a) and Fourier amplitude spectrum of the simulated nonstationary wavelets shown in Figure 3.5 (b).

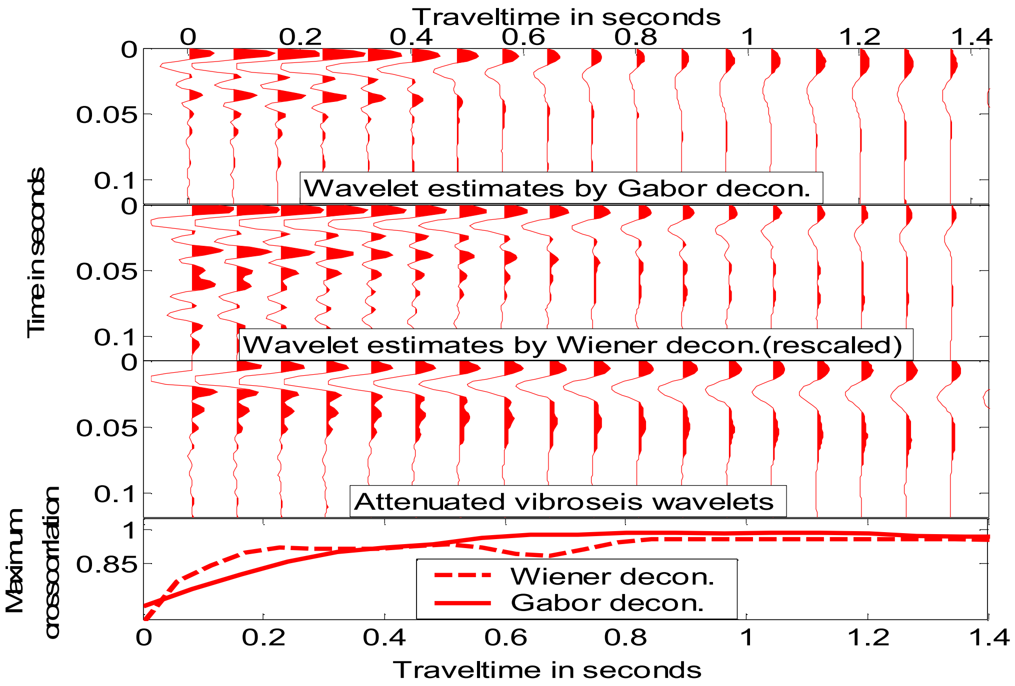

Figure 3.17 Wavelet estimates by Gabor and multi-window Wiener deconvolution from a synthetic vibroseis trace.

3.7 Chapter summary

In this chapter, the four different methods for nonstationary wavelet estimation are described. The first two approaches are the traditional time-domain Wiener deconvolution and frequency-domain Wiener deconvolution. Following the standard practice, in Wiener deconvolution, the wavelets are estimated on the gained and windowed synthetic nonstationary trace. Here the window is the boxcar. The other two methods are the Gabor deconvolution with boxcar smoothing and the Gabor deconvolution with hyperbolic smoothing. The wavelets are estimated on the same nonstationary trace but windowed by Gaussian function. All the wavelet estimates are then compared with the input nonstationary wavelet. We find that the wavelet estimates from the Gabor deconvolution with hyperbolic smoothing are the closest to the input wavelets. This means they are the most accurate among all the wavelet estimates.

Gabor amplitude spectrum of the seismic trace is usually approximated as the product of the Fourier amplitude spectrum of nonstationary wavelet and the Gabor amplitude spectrum of the reflectivity. This approximation depends on the Q value and the width of the analysis window. Our result shows that for small Q the commutator energy decreases with the increasing window width, but for big Q there is an optimal window length.

CHAPTER 4 NONSTATIONARY WAVELET ESTIMATION FROM REAL DATA

Wavelet estimation from real data is much more difficult than what we have done from synthetic data since the mechanism of the real data is more complicated. The major factors related to wavelet estimation from surface data include the following items:

1. Physical factors including transmission, spreading, absorption, mode conversion, intra-bed multiples and near surface effects.
2. Acquisition factors such as source type and strength, receiver coupling, coherent and ambient noise, offset range, and instrumentation.
3. Processing factors: noise reduction, spreading correction and wavelet estimation.

The physical and acquisition factors associated with wavelet estimates from VSP data are the same as those in surface data. The special factors in VSP wavelet estimation consist of wavefield separation, gain recovery and downgoing wave windowing.

This research only considers noise reduction, spreading correction, wavefield separation and wavelet estimation.

4.1 Survey and data quality

A simultaneous VSP and 2-D surface seismic survey was provided by EnCana for this research. The data acquisition was carried out in 1995 at Rosedale, located about 130 km Northeast of Calgary in Alberta. The recording geometry is shown in Figure 4.1. Receivers were positioned between 322 and 1820 m depth at a receiver interval of 20 m for a total of 75 receiver locations within the borehole. An additional 78 geophones were placed between 30 and 2310 m from the borehole at a 30 m interval on the surface. Five source points were used for this survey, located 27, 430, 960, 1350 and 1700 m from the borehole. The source was vibroseis with a 12 s, 10-96 Hz linear sweep. The recording was 16 second uncorrelated surface shot records and VSP records at a 2 ms sample rate.

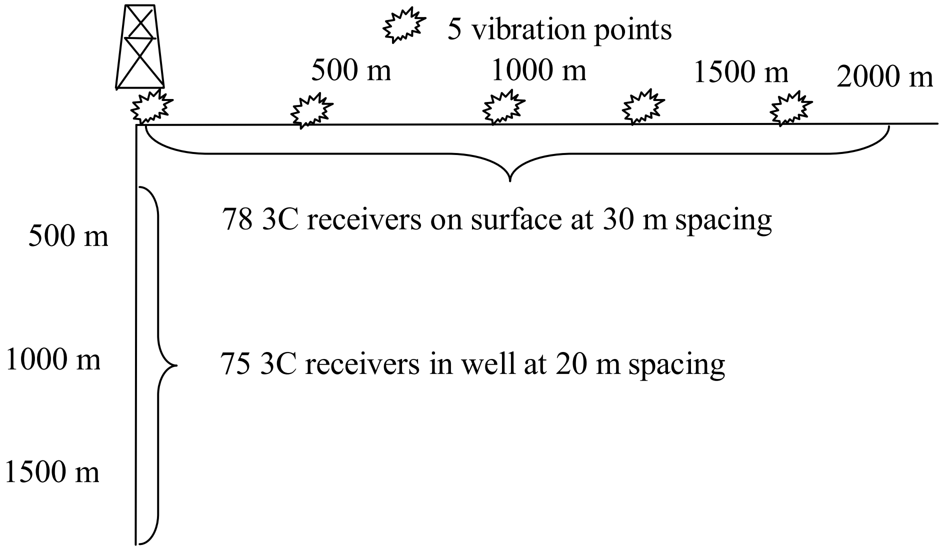

Figure 4.1 Geometry of a joint survey.

Figure 4.2 shows the gain-corrected vertical components of VSP data with the source location being 27m from the well. A 200 ms length AGC was applied for the purpose of display. The primary downgoing waves are seen as linear events traveling from left-to-right while upgoing waves travel up from left-to-right. Figure 4.3 shows the scaled vertical components of the surface data sharing the same source point as the VSP data shown in Figure 4.2. The surface data includes both reflected waves and noises. To identify these noises, we applied band pass filters with different frequency bands to the data gather shown in Figure 4.3. This is also called frequency scan. Figure 4.4 shows the filtered gathers with different band passes. Four kinds of the noises including ground roll, air blast, linear coherent noise and random noise can be easily observed from the data with different bandpass. Shallow refraction arrivals and guided waves, which are considered as noise in wavelet estimation, are also evident. All these noises need to be suppressed before the wavelet extraction. There are many strong reflections located between 0.8 and 2 s. The band width of the signal is from 10 to 50 Hz with high frequency components locating in shallow area and low frequency components extending to deep area. This frequency variation with the traveltime represents the nonstationarity of the seismic signal.

Unfortunately, the signal within near offset traces is buried in the ground roll so the wavelets have to be estimated from the middle offset area.

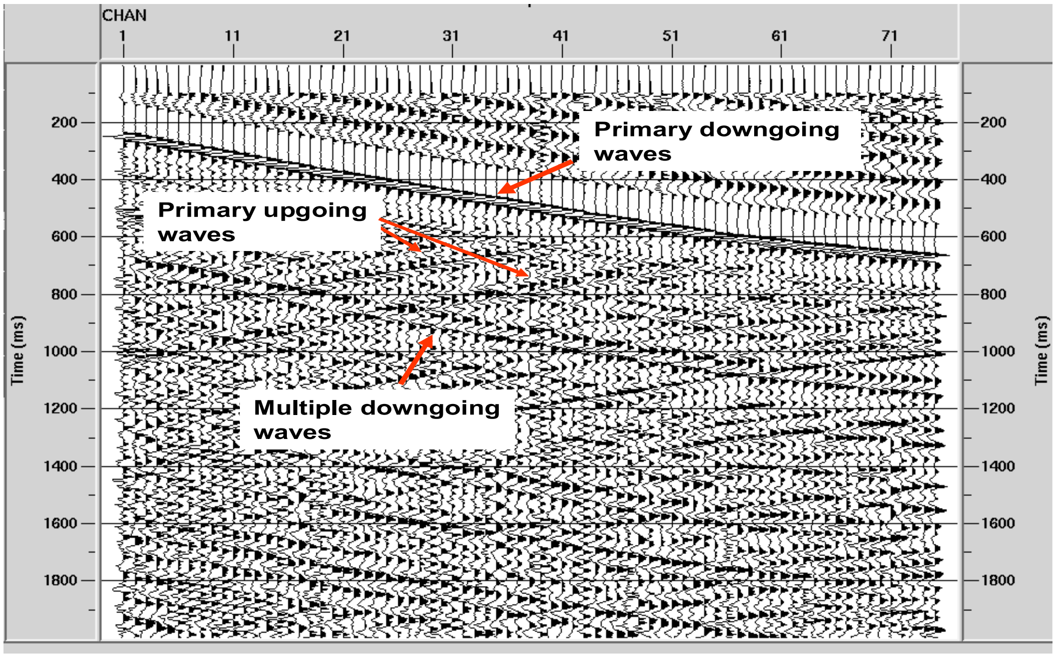

Figure 4.2 Vertical components of the zero-offset VSP section. A 200 ms length AGC was applied.

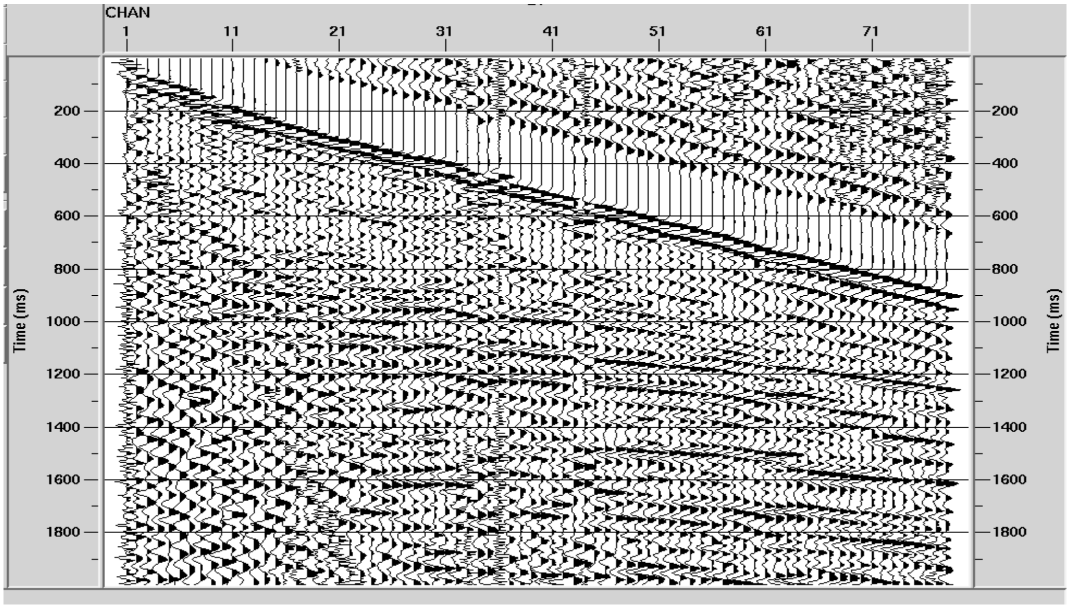

Figure 4.3 Vertical components of a raw source gather (surface data). A 400 ms AGC was applied.

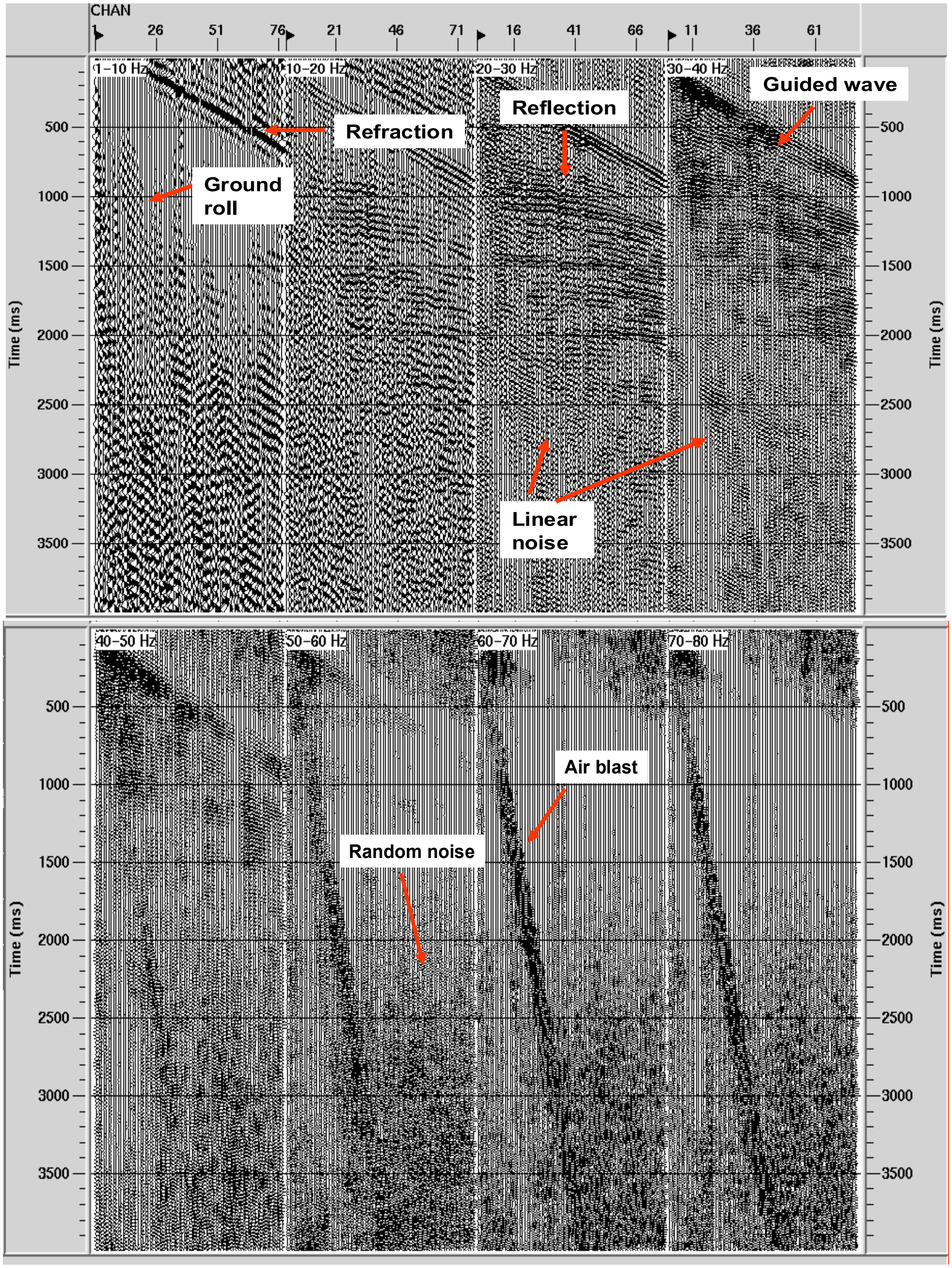

Figure 4.4 Panels of frequency scanning. A 400 ms length AGC was applied.

4.2 Wavelet estimation from VSP data

Wavelet estimation from VSP data is easier than from surface data; however, intensive data processing is still required. Many factors in processing can affect the wavelet estimates.

4.2.1 Wavelet estimation from VSP data

Figure 4.5 shows the flow chart for the VSP data processing before wavelet estimation. The major steps are vertical stacking, geometrical spreading correction, wavefield separation and downgoing wavefield windowing.

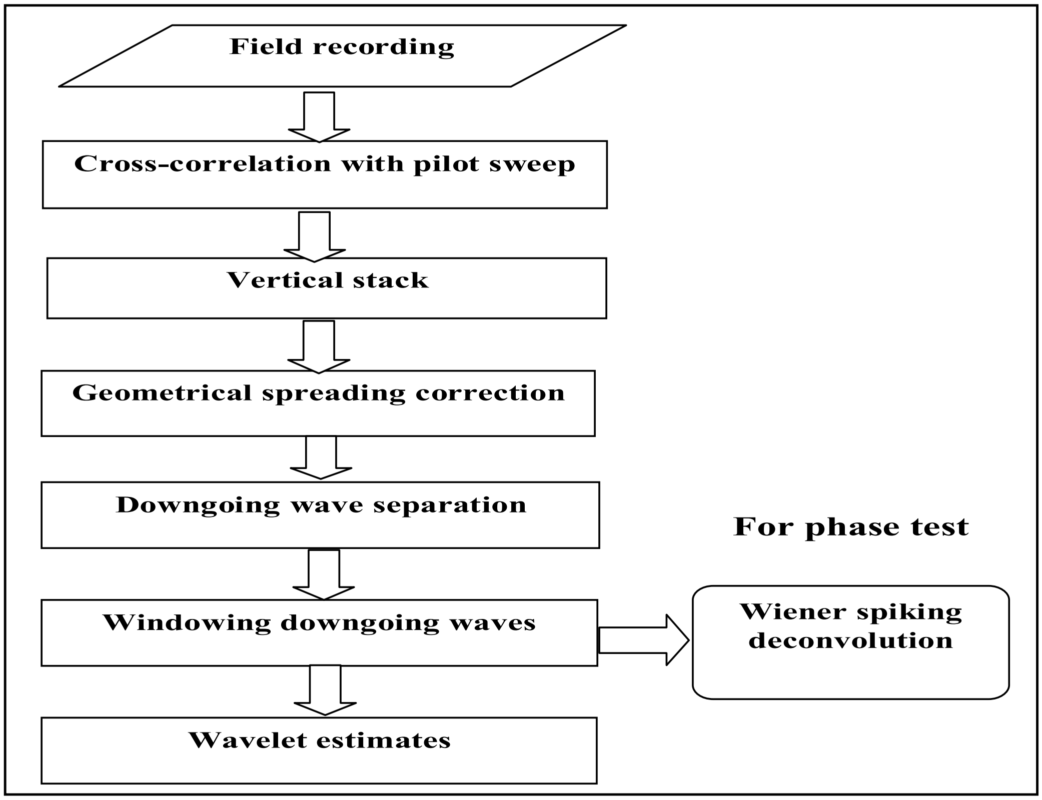

Figure 4.5 Flow chart for VSP data processing and wavelet estimation.

For each receiver position in the well 5 independent recordings were made. The direct sum of these recordings is called vertical stacking and reduces random noise. Figure 4.6

shows the VSP section before and after vertical stacking. The random noise was suppressed by vertical stacking.

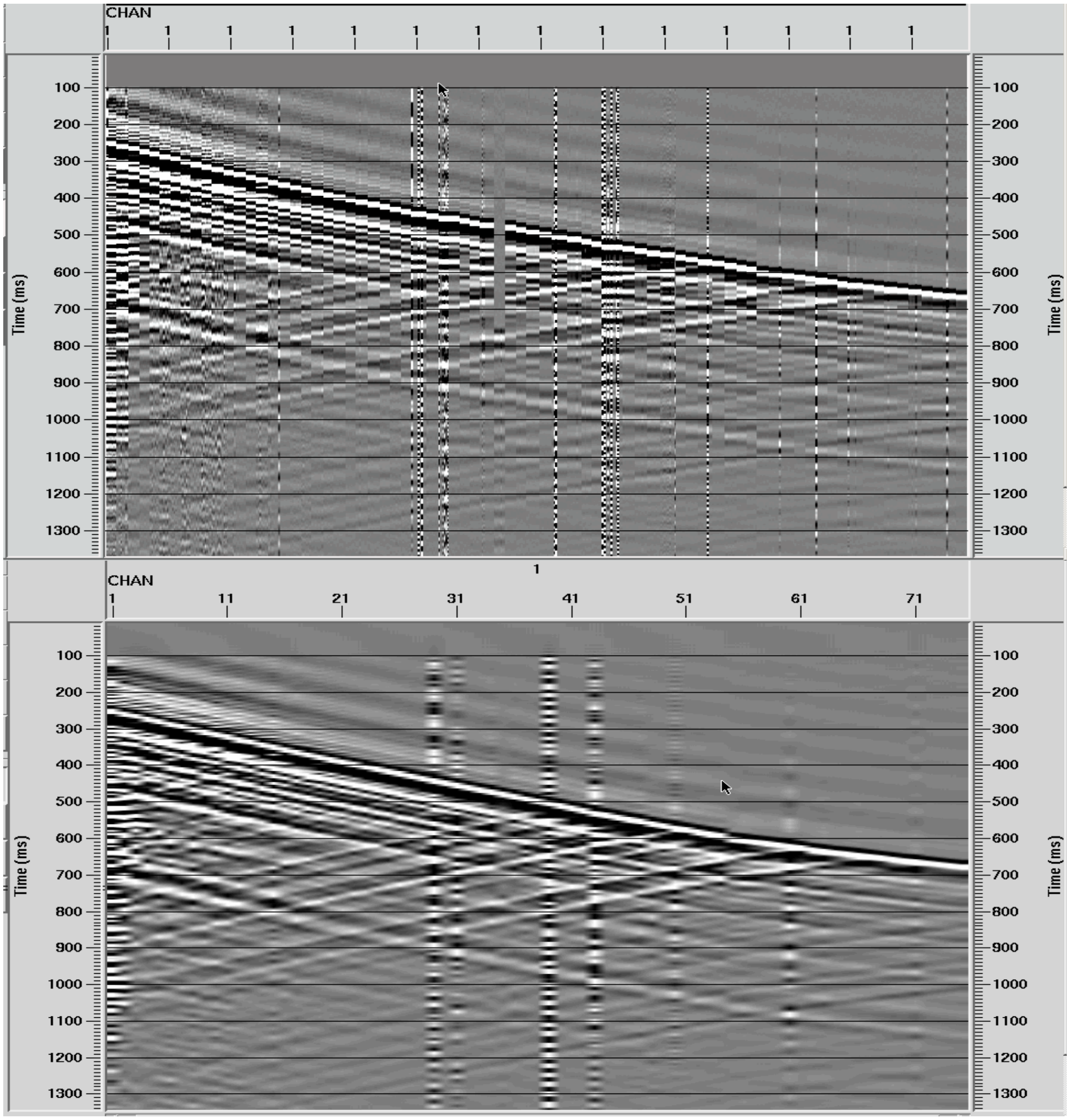

Figure 4.6 VSP section before (top) and after (bottom) vertical stacking displayed with a 200 ms length AGC.

The geometrical spreading correction removes the energy decay relating to spherical divergence. The velocity function used in the geometrical spreading correction was estimated by velocity analysis from surface data so as to make the energy consistent between VSP and surface data. Figure 4.7 shows the effect of the geometrical spreading correction without scaling. Comparing the data before the correction and the data after correction, we observed that the energy of the trace at greater times and depths was enhanced by the geometrical spreading correction.

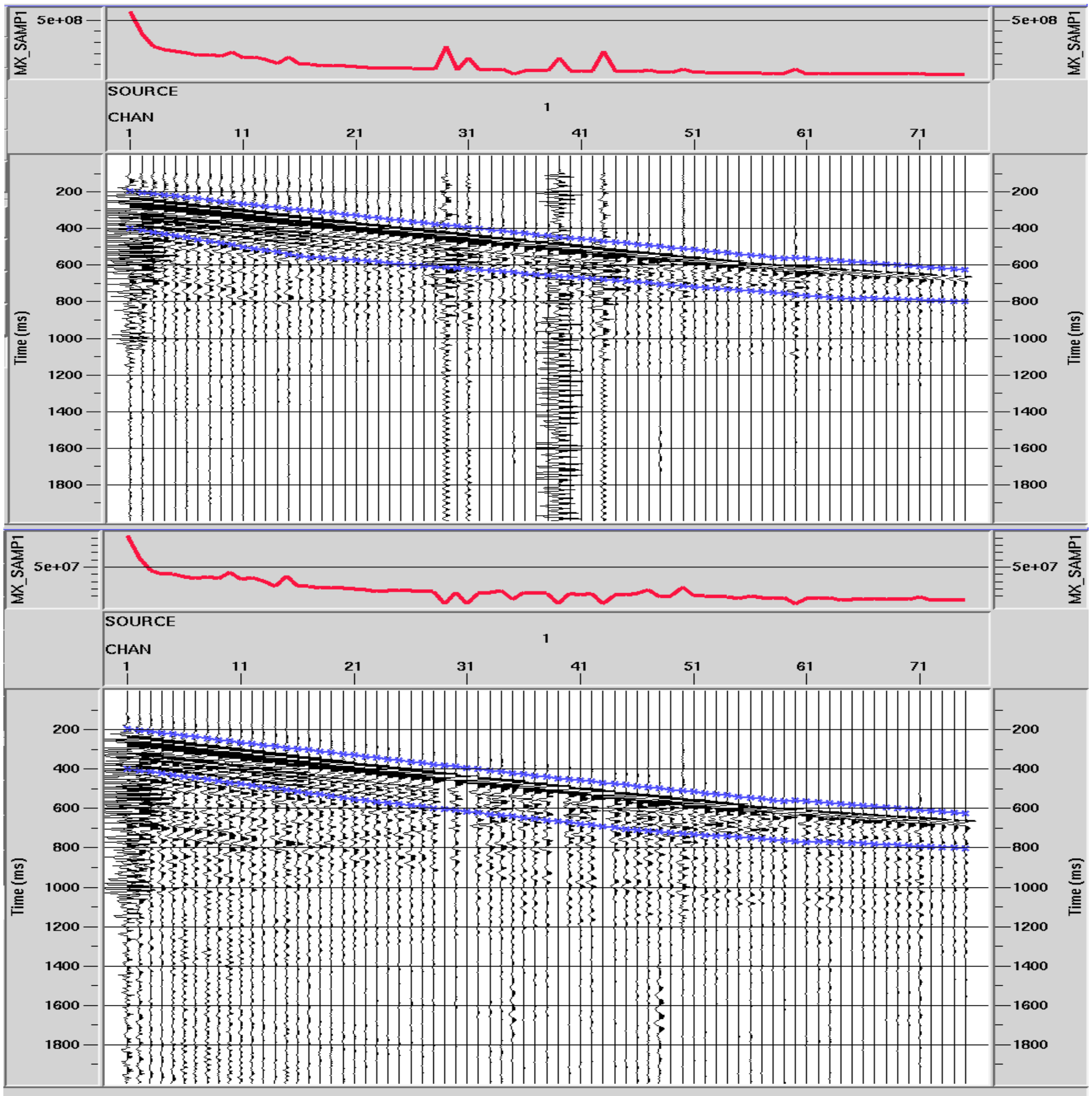

Figure 4.7 VSP data before (top) and after (bottom) geometrical spreading correction without gaining. The curve shown on the top of each figure is the maximum amplitude detected within the window shown in the figure. The noise traces were killed on the bottom figure.

Wavefield separation refers to the process of isolating the downgoing and upgoing wavefield. This was done in three steps. First the first breaks of downgoing waves were flattened. Second a median filter (at central time) was run to suppress the upgoing waves and thus isolate the downgoing waves. Finally, the upgoing waves were estimated by subtraction of the estimated downgoing waves from the flattened record (of step 1). Figure 4.8 shows the maximum amplitude for each depth of the estimated downgoing waves for various median filter lengths. We observe that the length of the median filter has little effect on amplitude variation, but the short filter may yield a few irregular amplitude values as shown in Figure 4.8. After many experiments, finally the 11-point median filter was chosen for the wavefield separation. Figure 4.9 shows the flattened wavefield (a) and separated downgoing waves (b) with 0.1 second length AGC applied, and the same wavefield (c) and the downgoing waves (d) without AGC.

Finally, the downgoing wavelets are estimated by applying a boxcar window to isolate the downgoing wave from 0.2 to 0.4 seconds. Figure 4.10 shows the wavelet estimates where the change in the wavelet with depth is caused by absorption and transmission factors. Figure 4.11 shows the Fourier amplitude spectra of wavelet estimates. Each line from the top to the bottom represents the Fourier amplitude spectrum of the wavelet estimate from the shallow to the deep receiver level. A progressive decay of the amplitude spectrum and a reduction in bandwidth of the amplitude spectrum with increasing depth are evident. The notches shown in the amplitude spectra are result of ghosts or downgoing multiples.

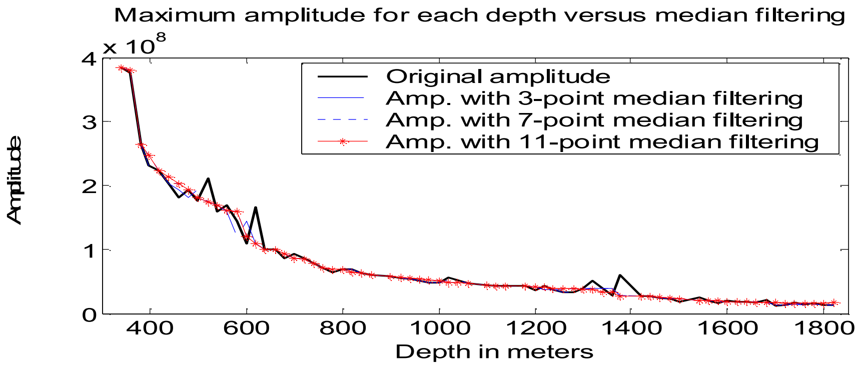

Figure 4.8 Maximum amplitude for each depth versus different median filter lengths.

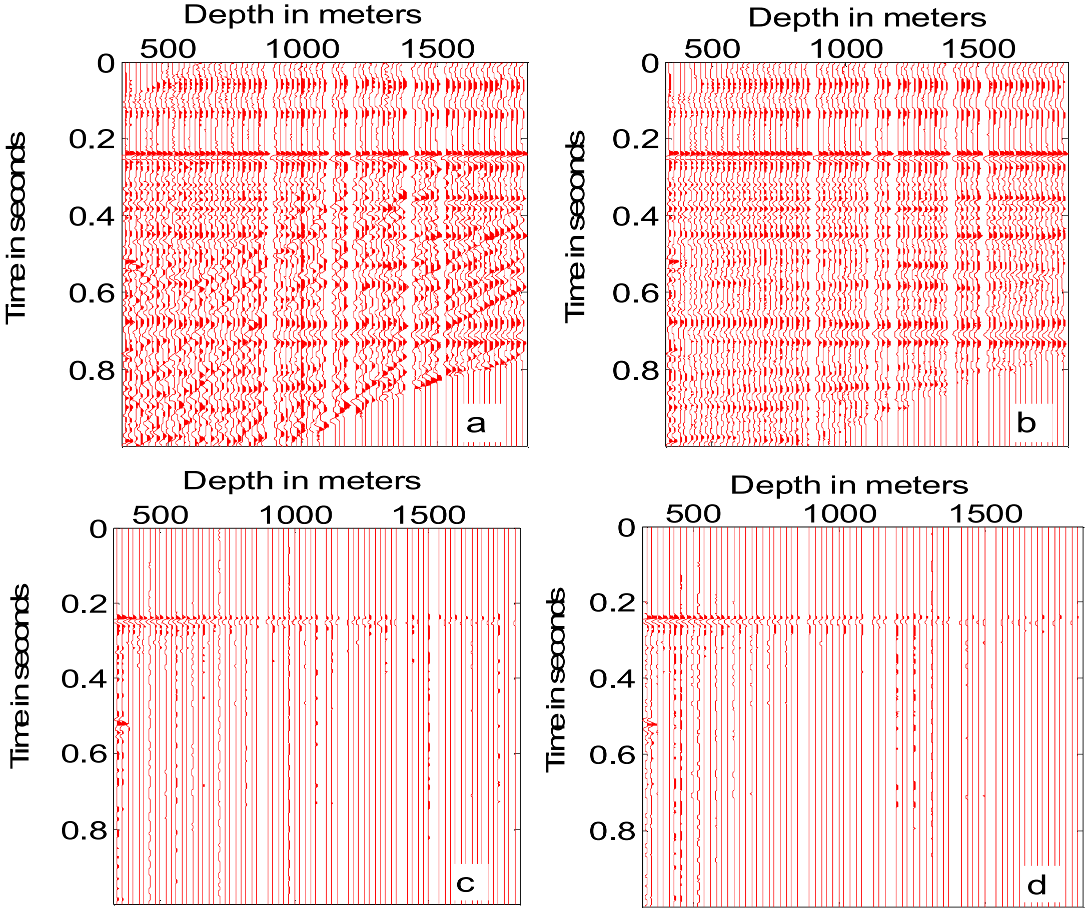

Figure 4.9 Flattened VSP data (a) and separated downgoing waves (b) using 0.2 s length AGC, and the flattened VSP data (c) and the downgoing waves (d) without AGC. Gaps occur where noisy traces have been deleted.

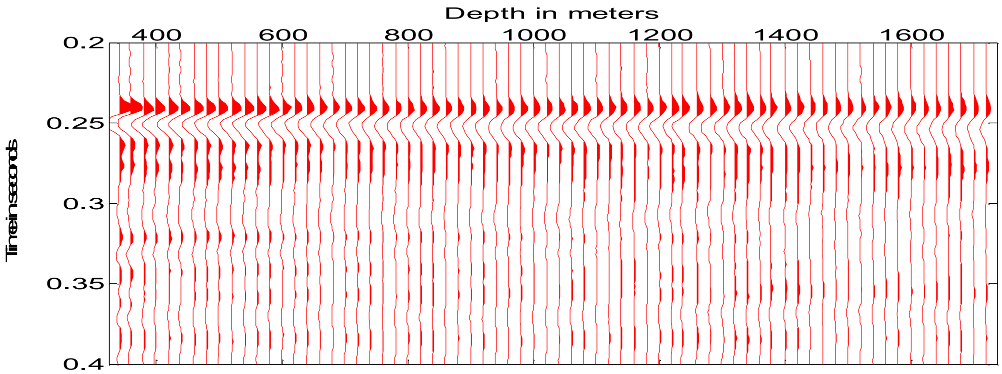

Figure 4.10 Wavelet estimates from VSP downgoing waves. The deleted traces were interpolated.

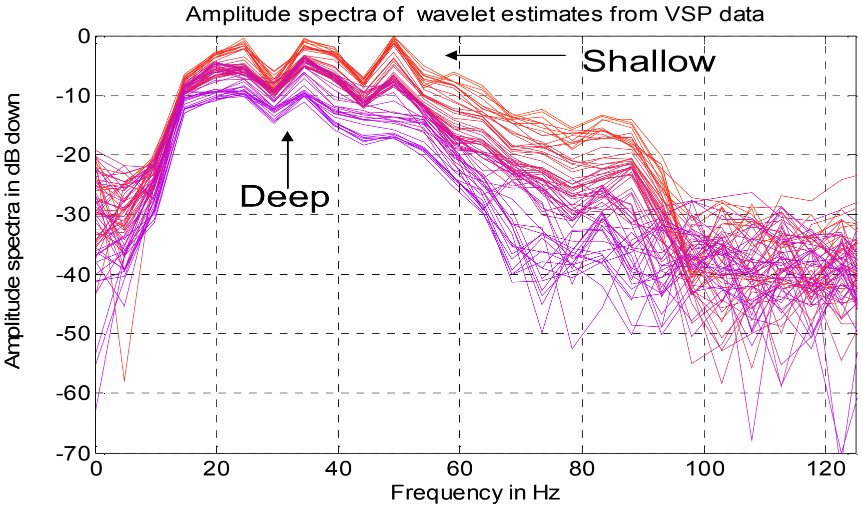

Figure 4.11 Fourier amplitude spectra of the wavelet estimates from VSP data. The lines represent the Fourier amplitude spectrum estimates at the different depth levels.

4.2.2 Phase characteristics of the wavelet estimates

The phase property of the wavelet estimate from a vibroseis source is still an important topic discussed by many people. Conventionally, the measured uncorrelated data are cross-correlated with the sweep from the recording truck. The wavelet embedded in the correlated data is assumed to be the zero-phase autocorrelation of the sweep (see Brötz et al, 1987; Bickel 1982). This assumption has been challenged by Baeten and Ziolkowski (1990) who show that the wavelet is not an autocorrelation function but the cross-correlation between the pilot sweep and the ground force, which can be determined from measurable vertical acceleration of the base plate and the reaction mass. The far field wavelet is equal to the cross-correlation between the pilot sweep and the time derivative of the ground force. Thus, the wavelet from the vibroseis source propagating in the elastic medium is not zero-phase. Ziolkowski's argument ignores attenuation. Gibson and Larner (1984) attempted to shape the vibroseis wavelet to minimum phase by reducing the earth filter effects and phase correction. Brittle (2001) stated that the presence of earth-attenuation results in a mixed-phase wavelet that is the convolution of the Klauder wavelet and the earth-attenuation minimum-phase filter, but this assumption is not verified. Therefore, the phase property of the wavelet embedded in the vibroseis trace is still an unsolved problem. The theoretical verification of this phase property is very difficult, but it can be examined empirically by a minimum-phase deconvolution. In time-domain Wiener spiking deconvolution, if the wavelet is minimum-phase and the reflectivity is white, the output of the deconvolution would be close to band-limited zero-phase spike. Conversely if the output of this deconvolution is close to the band-limited zero-phase spike, we can infer that the wavelet is a reasonable approximation to minimum phase.

In Section 3.1, we applied Wiener deconvolution to the simulated nonstationary vibroseis wavelet and found that this wavelet is close to a minimum-phase wavelet. Here Wiener spiking deconvolution was further applied to the wavelet estimates from the real VSP data. In Wiener deconvolution, the data for the operator design were chosen in the range from 0.2 to 0.3 s which is symmetric about the wavelet location. Operator length was 0.12 s and stabilization factor was chosen to be 0.0001. Figure 4.12 shows the deconvolved wavelets and their amplitude spectra. After deconvolution, the wavelet was compressed into band-limited approximation to an impulse. Figure 4.13 shows the wavelets before Wiener deconvolution (a) and after Wiener deconvolution (b). All the wavelets were normalized for display purposes. The deconvolved wavelets are close to the band-limited zero-phase spikes.

Therefore, we believe that the propagating wavelet in the VSP data from a vibroseis source is effectively minimum phase. This property is very important in wavelet estimation from surface data since we can only estimate the amplitude spectra of the wavelets and don’t know their phase property. The phase property of the VSP wavelet can help us to make a correct phase assumption for the wavelet estimates from surface data.

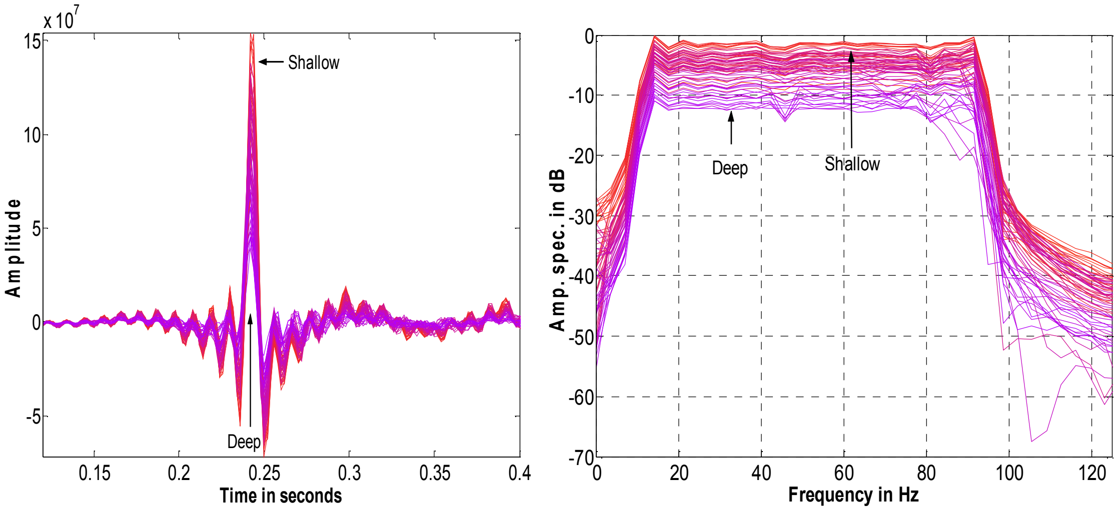

Figure 4.12 Wiener spiking deconvolved wavelets (left) and Fourier amplitude spectra (right) where each line represents the Fourier amplitude spectrum of the deconvolved wavelet estimated at the different depth level. The deconvolved wavelets approximate to the band-limited impulses.

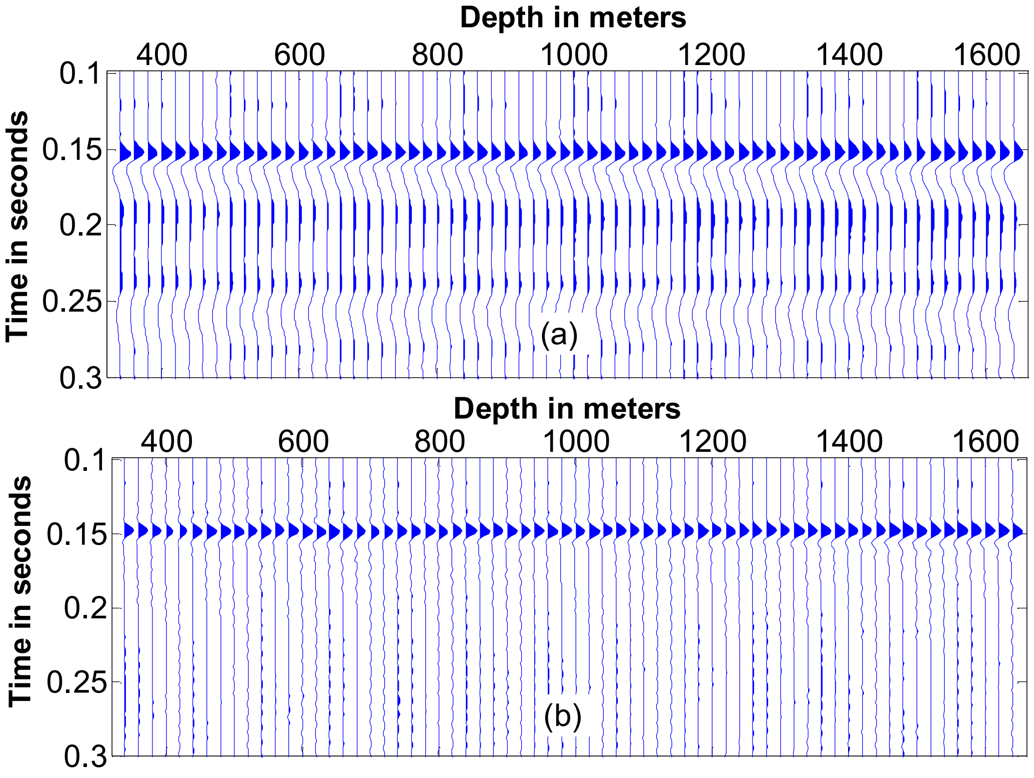

Figure 4.13 Wavelets before Wiener spiking deconvolution (a) and after Wiener deconvolution (b). All the wavelets were normalized.

4.3 Surface data preprocessing and wavelet estimation

4.3.1 Data preprocessing

The objective of the data preprocessing is to suppress noise, recover amplitude and estimate stacking velocity. Figure 4.14 shows the flow chart for wavelet estimation. The first part of the figure shows the steps in data preprocessing and the second part is the procedure of wavelet estimation.

Low frequency and low velocity noise were suppressed by the program called *surface wave attenuation* in ProMAX. This program attempts to remove coherent noise by f-k filter. Geometrical spreading was corrected by *true amplitude recovery* in ProMAX. The velocity used in geometrical spreading correction was estimated from common middle point gathers. Figure 4.15 shows the source gather before processing (left) and the same gather after processing (right) without any gain. After processing, the signal in the deep and far-offset areas was obviously enhanced and the noises were suppressed.

Figure 4.16 shows the same processed gather as Figure 4.15 with a 400 ms length AGC applied. Since the near-offset traces still contain ground roll, we choose traces with much less noise from the data within the middle offset range. The traces within the boxcar window on Figure 4.16 are selected to estimate the wavelet.

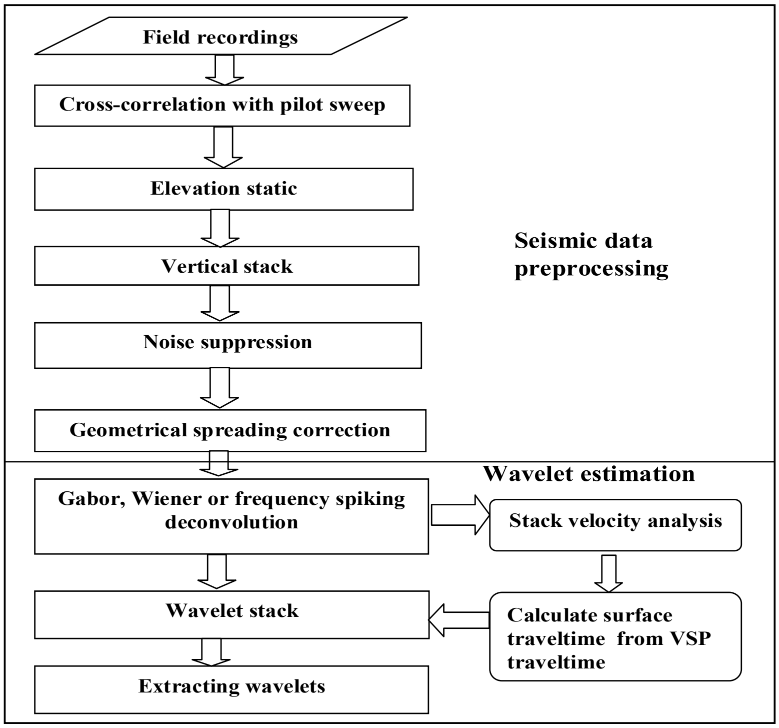

Figure 4.14 The flow chart for wavelet estimation from surface data.

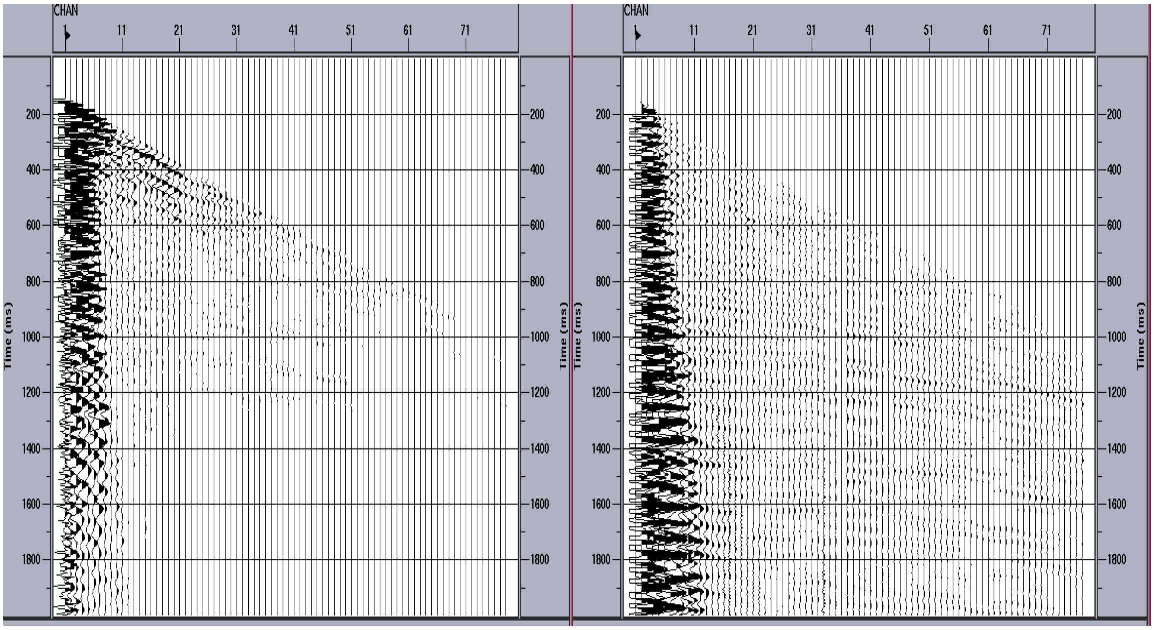

Figure 4.15 The gather before processing (left) and the same gather after processing (right). The processing steps include noise suppression, static correction, geometric spreading correction and shallow refraction muting. Both sections were displayed without scaling.

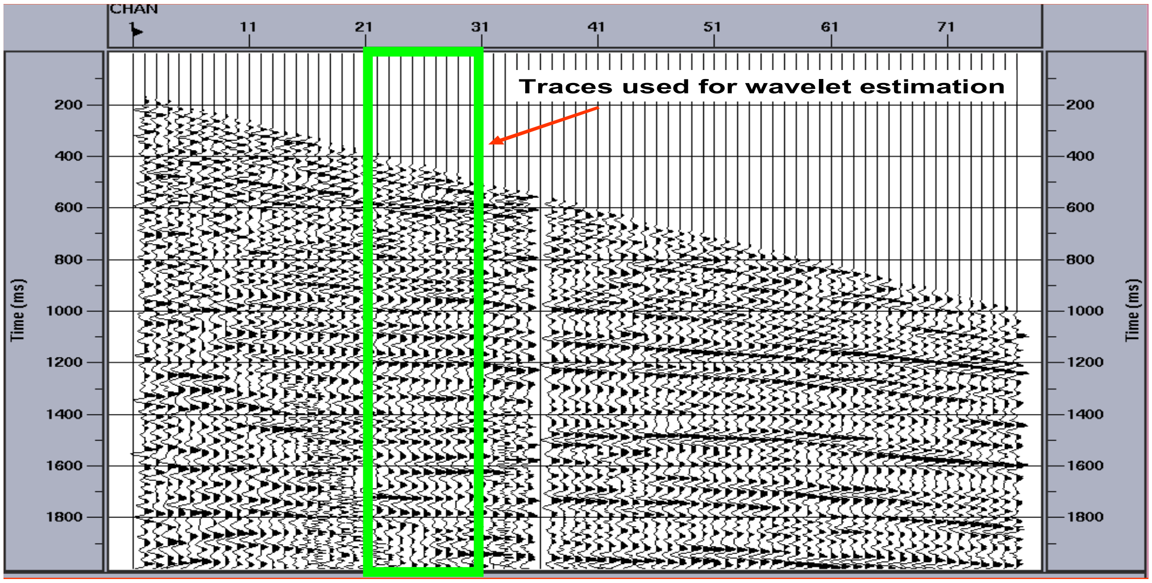

Figure 4.16 The same gather as shown on the right of Figure 4.15 , but with a 400 ms length AGC applied.

4.3.2 Wavelet estimation and selection

The principle and method of the wavelet estimation by Gabor deconvolution has been introduced in chapter 3 where all the wavelet estimates were extracted under the assumptions of white reflectivity and minimum phase wavelet. For the real data, it is said that the assumption of white reflectivity brings fewer problems than assumptions in the wavelet phase (Dey, 1999). The wavelet estimation requires us to assume the phase property of the wavelet at very beginning stage since the phase property determines the methods applied in the wavelet estimation. For the wavelet estimates from VSP data, we have verified that their phase is close to minimum phase. For the data received on the surface they share the same source as VSP data and travel in the same media. Thus, it is reasonable to assume the wavelet estimates from surface data are also minimum phase.

Now we describe how to estimate the VSP-related wavelets from surface data. At first, we define a specified reflector model as the horizontally layered medium with interfaces located at the position of each receiver in the borehole. We call these interfaces as equivalent reflectors. This definition is reasonable under the random reflectivity assumption from which every point in the medium can be considered as a reflection point. From the stacked section shown in Figure 4.17, the real medium in our case is close to the horizontally layered medium. So the defined medium model is realistic and valid for our research.

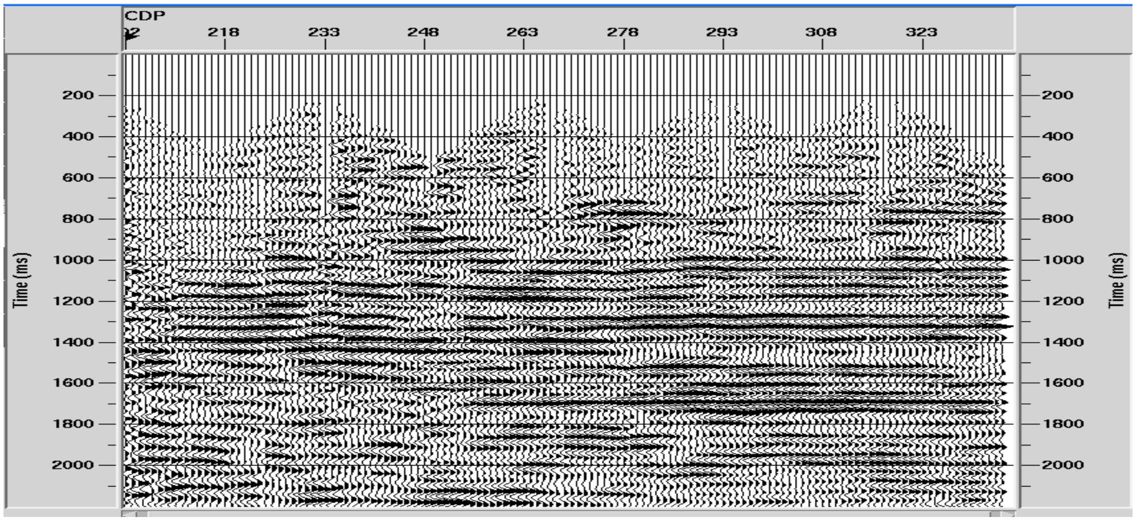

Figure 4.17 Stacked section from the joint survey shown in Figure 4.1.

Figure 4.18 shows a simple model as we defined above. Suppose VSP traveltime, t_1, is the arrival time to a receiver in the borehole for an offset VSP, and surface traveltime, t_2, is the two-way traveltime of a reflection recorded at the surface for a reflector at the same depth. The relationship between t_1 and t_2 can be expressed as

$$t_2 = \sqrt{4t_1^2 - \frac{4c^2}{v_a^2} + \frac{x^2}{v_{stk}^2}}\ , \qquad (4.1)$$

where v_a is the average velocity which can be calculated from the first break in VSP wavefield at time, t_1, v_{stk} is the stacking velocity estimated from the surface seismic, c is the horizontal distance between the shot location and the borehole, and x is the source-receiver offset on the surface.

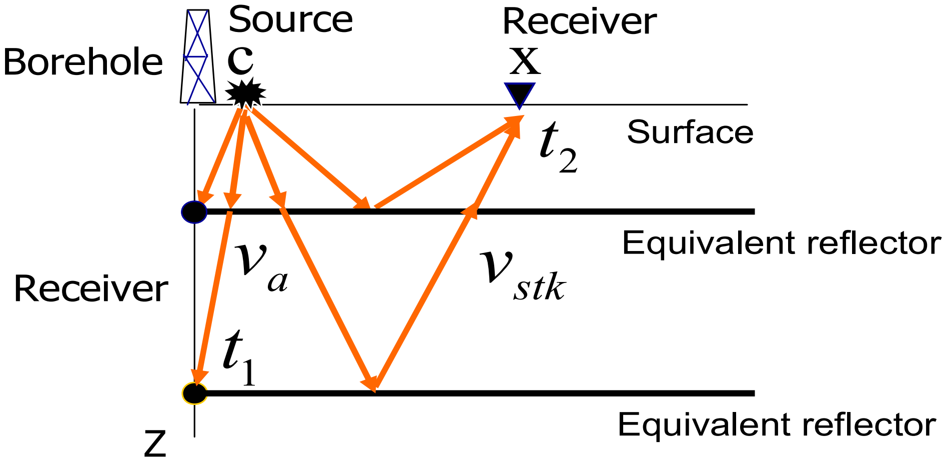

Figure 4.18 The relationship of the oneway and two-way traveltime.

From equation (4.1), we know that for a fixed x, there is only one wavelet estimate from surface data corresponding to a VSP traveltime. Figure 4.19 shows the VSP traveltime, t_1, measured from VSP first break and calculated surface traveltime, t_2, at 10 horizontal offsets of 10 traces chosen for wavelet estimation. The time difference in the shallow area between different traces is bigger than that for deeper data.

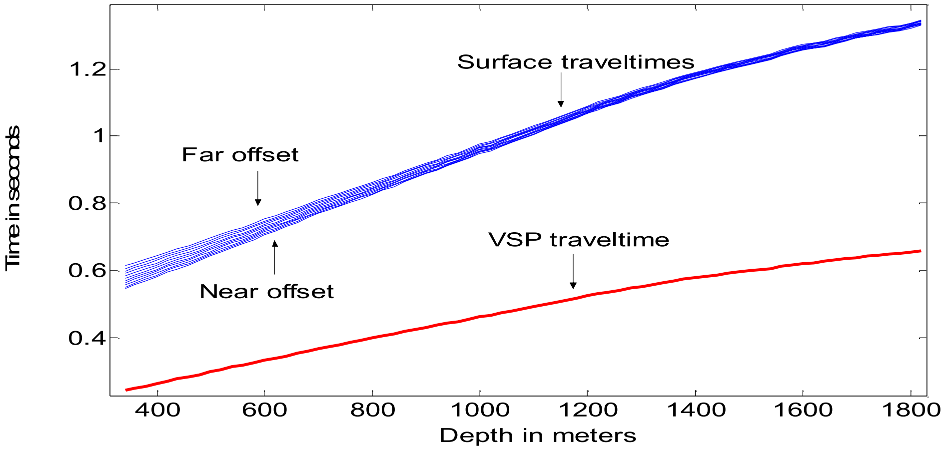

Figure 4.19 VSP one-way traveltime and corresponding surface traveltimes calculated from equation (4.1).

Although we have suppressed the noises before the wavelet estimation, some residual noises or other factors may still distort the shape of the wavelet estimates as shown in

Figure 4.20 where ten wavelets were estimated by Gabor deconvolution from the selected traces shown in Figure 4.16 without AGC. Most of them are similar to each other, but some are different in the waveform. To make the wavelet estimates more reliable and stable, the wavelets estimated from each trace were stacked to yield final wavelet estimate. The equation in wavelet stacking is given by

$$\overline{w}(t,t_2) = \sum_{j=1}^{N} w(t,t_2,x_j)/N, \tag{4.2}$$

where N is the number of traces to be stacked and x_j is the offset of the j^{th} trace.

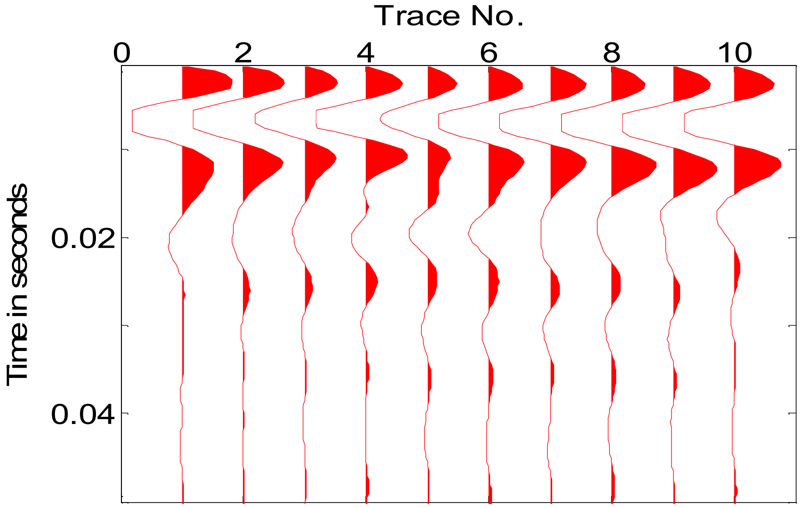

Figure 4.20 Wavelet estimates at twoway traveltime of 0.8 s from traces show in Figure 4.16.

Figure 4.21 shows the final wavelet estimates from surface data by Gabor deconvolution with hyperbolic smoothing (a), and corresponding wavelet estimates from VSP data (b). In Gabor deconvolution, a Gaussian window with 0.2 s half width and a boxcar smoother of 25 Hz length were applied.

Figure 4.22 show the Gabor amplitude spectrum of the wavelet estimates shown in Figure 4.21 (a), and the Fourier amplitude spectra of the wavelet estimates shown in Figure 4.21 (b). The dominant frequency shown in Figures 4.22 (a) and 4.22 (b) are similar to each other. In an earlier time, the bandwidth of the surface wavelets is wider than that of the VSP wavelet. With increasing the time they are close to each other.

Apparently, the wavelet estimates from the surface data were attenuated much more than the wavelet estimates from the VSP data. This difference, caused by constant-Q attenuation, will be discussed in Chapter 5.

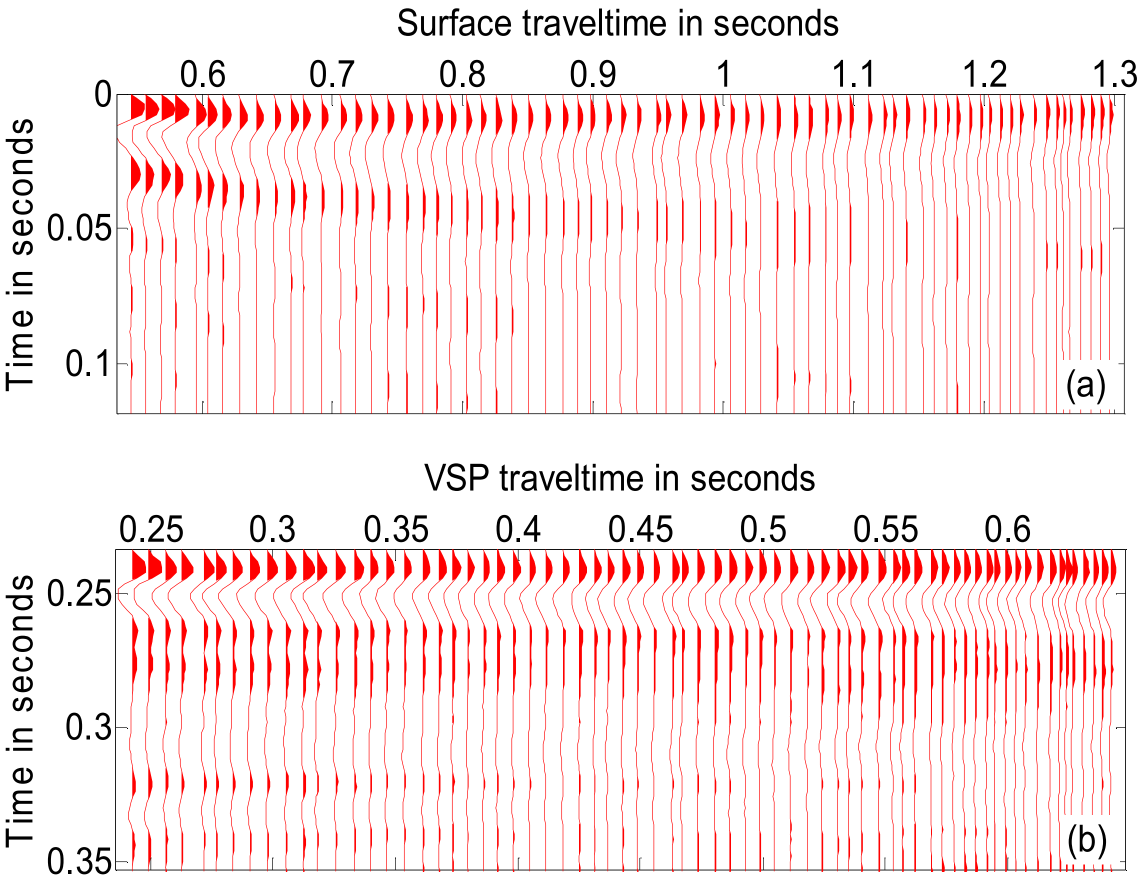

Figure 4.21 Wavelet estimates from surface data by Gabor deconvolution with hyperbolic smoothing (a), and wavelet estimates from VSP data (b).

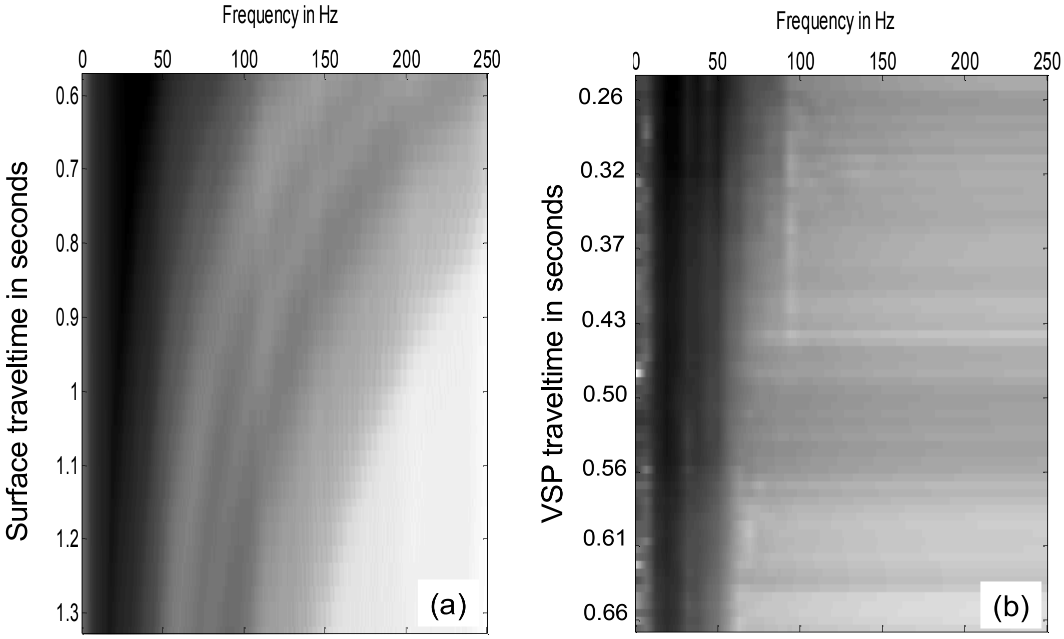

Figure 4.22 Gabor amplitude spectrum of wavelet estimates from surface data (a) and Fourier amplitude spectra of wavelet estimates from VSP data (b).

4.3.3 Parameter testing of Gabor deconvolution

In addition to the factors we introduced at the beginning of this chapter, the parameters in the wavelet estimation also contribute to the variation in the wavelet estimates. Here we will test the effects of the window width and the smoother length on the wavelet estimates

Effect of the window length on the wavelet estimates

The window length, the half width of Gaussian, will affect the wavelet estimate. The stationary deconvolution requires the window length be long enough to make the wavelet estimate stable within a quite wide temporal range. A rule of thumb in the industry is that the window length should be at least eight times the length of the deconvolution operator (Yilmaz, 1987). The window length in the nonstationary deconvolution links with the Q value. The higher the Q value the larger the upper bound on window length can be. However the longer the window, the more the wavelet estimate will be averaged. For the nonstationary deconvolution, the window length should be consistent with the expected nonstationarity of the wavelets. The optimum length only can be determined by comparison of the deconvolved trace or wavelet estimate to the data from well, or by extensive testing of a variety of window lengths.

At first let us see the effect of the window length on the wavelet estimates from Gabor deconvolution with the boxcar smoother. Figure 4.23 shows the wavelet estimates and their amplitude spectra at four different times with three windows. The longer the window, the stronger the high frequency components are. The reason for this phenomenon is that the high frequency components in shallower area are stronger than those in deeper area.

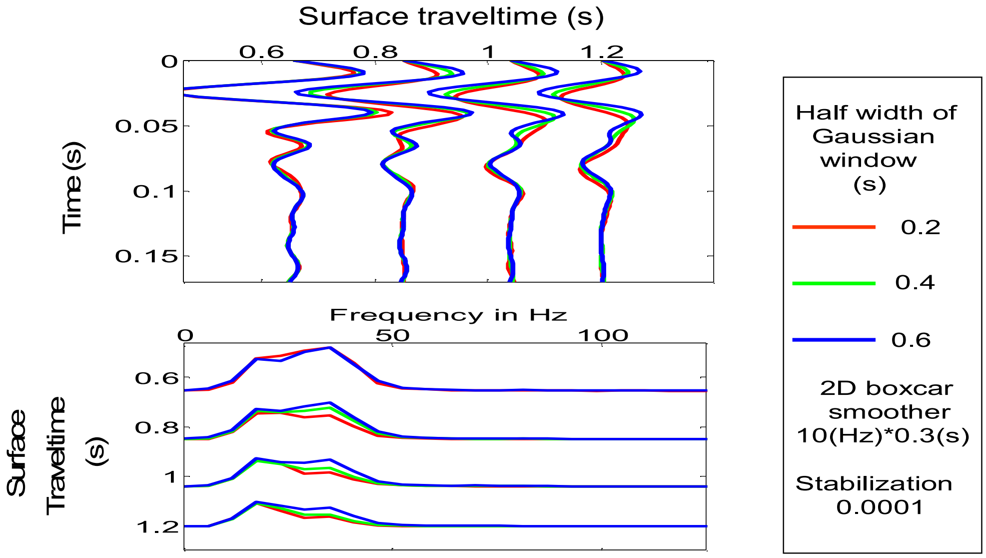

Figure 4.23 Wavelets (top) and corresponding amplitude spectra (bottom) estimated with Gaussian windows of different lengths.

Figure 4.24 shows the variation in both wavelet estimates and their spectra from Gabor deconvolution with the hyperbolic smoother. The change in the frequency components is similar to that shown in Figure 4.23.

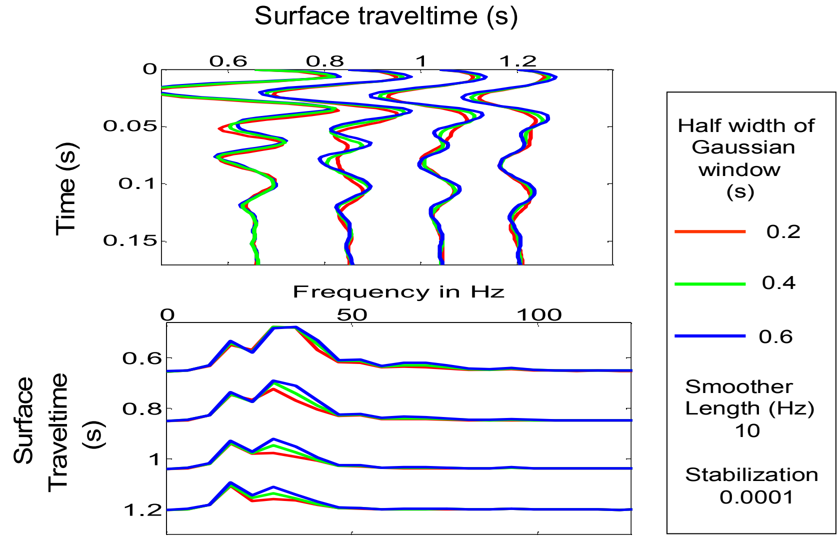

Figure 4.24 Wavelets (top) and corresponding amplitude spectra (bottom) estimated with Gaussian windows of different lengths.

Effect of smoothing on the wavelet estimates

The Gabor spectrum of the wavelet estimate includes the effect of constant-Q attenuation. This attenuation surface is a relaxation function in the traveltime and frequency domain. The size of the boxcar smoother will affect the attenuation function. The bigger the size of the boxcar, the less the estimated attenuation surface changes in time-frequency domain. In the extreme case, an smoother with an infinite length would yield a constant amplitude spectrum and a wavelet estimate close to an impulse. Therefore, the smoother length should be chosen carefully. The optimum smoother length can be obtained by comparing the wavelet estimates to the VSP wavelet (as we did in this thesis), or by extensive testing of the different lengths of the smoother.

Figure 4.25 shows the influence of the frequency domain smoother length on wavelet that was estimated by Gabor deconvolution with a boxcar smoother. Here the half width of the widow is 0.2 s and the time domain smoother length is 0.3 s. It is clearly displayed that the smoother extends the bandwidth of the wavelet estimates and also introduce a phase rotation. The longer smoother makes the wavelet estimate similar to an impulse.

Figure 4.26 shows the effect of three different lengths of the boxcar smoothers on the wavelet and amplitude spectrum estimates in the case of Gabor deconvolution with hyperbolic smoother. The result of smoothing in this case is similar to that shown in Figure 4.25, but now, only the amplitude spectra of the source signature estimates are smoothed and no time smoother is applied. Thus the biases caused by smoothing should be less than those by the time-frequency domain boxcar smoother.

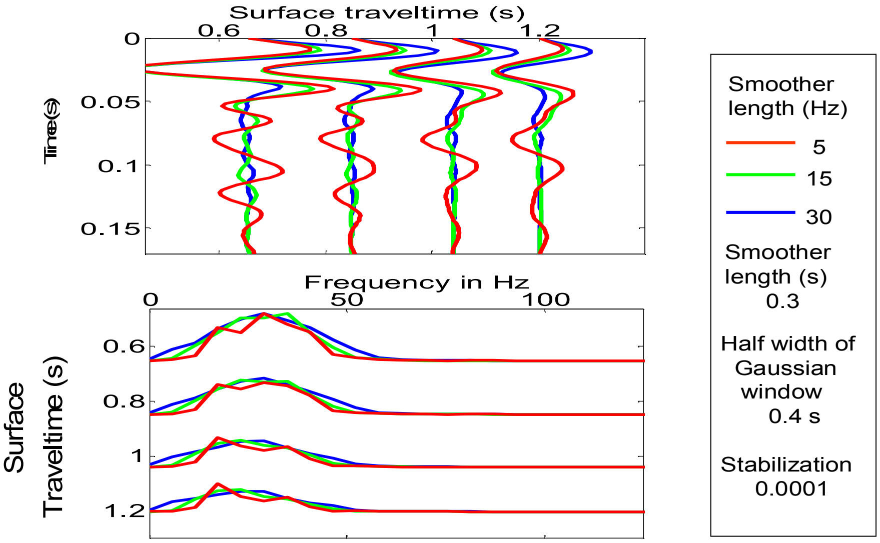

Figure 4.25 Wavelets (top) and corresponding amplitude spectra (bottom) smoothed by boxcars with different lengths in the frequency domain.

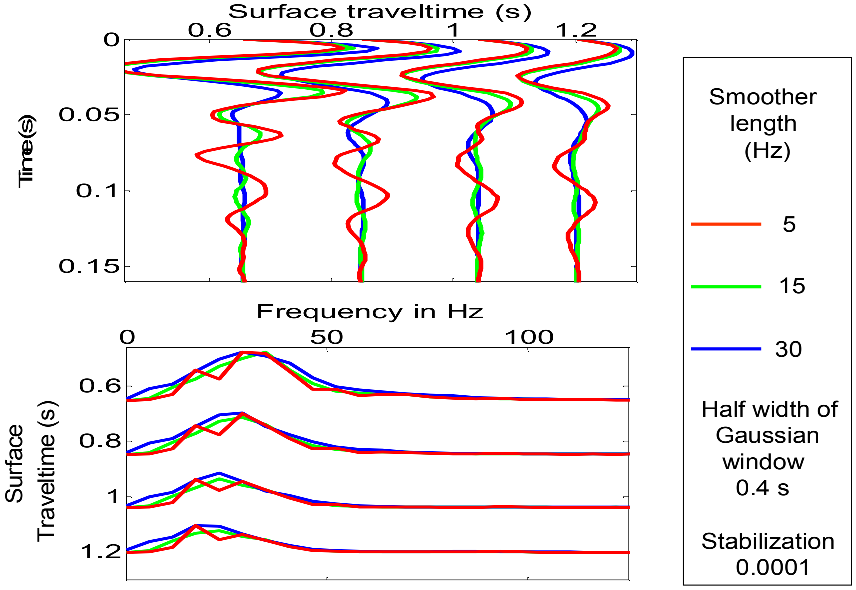

Figure 4.26 Wavelets (top) and corresponding amplitude spectra (bottom) corresponding to the three source signature estimates smoothed by boxcars with different lengths in frequency domain.

4.3 Chapter summary

The real VSP wavelets are extracted from VSP downgoing waves. As the result of the phase examination by the time-domain Wiener deconvolution, the wavelet estimates are found to be close to minimum phase though the vibroseis source is zero-phase. Based on this phase property, we estimate the wavelets from the real surface seismic traces sharing the same source signature with the VSP data. Then the wavelets reflected from the equivalent reflector are extracted. Each of these wavelets is corresponding to the different wavelet estimates from VSP data.

The intensive VSP and surface data processing plays a key role in the wavelet estimation. The purpose for the data processing is to separate the other factors from seismic attenuation and to make the wavelet embedded in the seismic trace be associated only to the source signature and the seismic absorption.

The window width and smoother length also influence the wavelet estimates. The wide window will enhance the high frequency components in the wavelet estimates and too short smoother will make the wavelet vibrate strongly.

CHAPTER 5 COMPARISON OF WAVELET ESTIMATES FROM VSP AND SURFACE DATA

The accuracy of the nonstationary wavelet estimates determines the performance of Gabor deconvolution. Verifying the accuracy of the wavelet estimates only from surface data themselves is difficult. Conventionally, people consider the wavelet estimates are correct providing that the deconvolved trace is similar to the band-limited reflectivity estimated from log data. Usually this is difficult because the original bandwidths of the log recordings and seismic data are very different. On the other hand, VSP and surface data usually share similar bandwidth especially in the joint VSP and surface survey. Ever better, the nonstationary wavelet is directly recorded by VSP downgoing waves. Thus, it is possible to evaluate the accuracy of the surface wavelet estimates by VSP data.

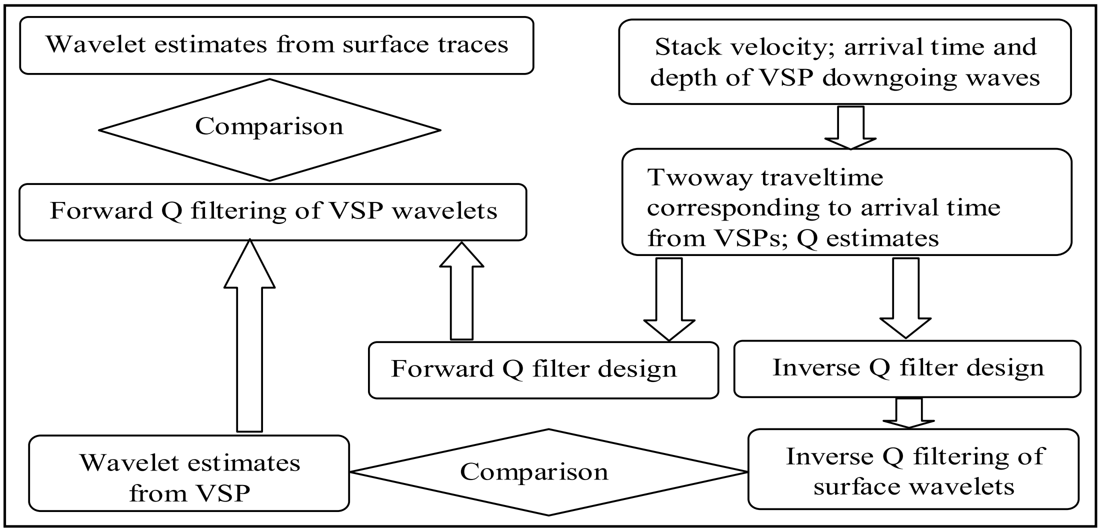

Figure 5.1 Flow chart for wavelet estimate comparison.

In this chapter, first we will describe the differences between the VSP and surface data, and also introduce how to reduce these differences so as to make the wavelet estimates from VSP and surface data more comparable. Then the wavelet comparison will be implemented on the synthetic data and finally the wavelet estimates from real VSP and surface data will be compared. The strategy of the wavelet comparison is shown in Figure 5.1

5.1 The difference of the wavelet estimates from VSP and surface data

Although the wavelets in our VSP and surface data share the same source and travel in the same medium, they are not equivalent. The major factors causing these differences include

1. **Spreading loss**

For a point source, the amplitude of the spherical wave traveling through the body of a medium decreases inversely as the distance the wave has traveled (Sheriff, 1991). Thus, the amplitude of the wavelet estimated at surface traveltime, t_2, can be written as the function of the amplitude of the wavelet estimated from VSP traveltime, t_1, which is

$$A(t_2) = \frac{v_{stk}(t_1)t_1}{v_{stk}(t_2)t_2} A(t_1), \tag{5.1}$$

where A denotes the amplitude of the wavelet estimates. t_1 and t_2 are defined in equation (4.2). v_{stk} denotes the stacking velocity which is estimated from the CDP gathers of the surface data. In both surface and VSP data processing, we have recovered amplitude decay caused by the geometrical spreading with the program called *true amplitude recovery* in ProMAX system. The results of the geometrical spreading correction are shown in Figures 4.6 and 4.14.

2. **Transmission loss**

For a normal incidence transmission through a set of horizontal layers, the two-way transmission loss is

$$T_{sur}(N)=\prod_{k=1}^{N}\left[1-R_k^2\right], \tag{5.2}$$

where T_{sur} and R_k are transmission and reflection coefficients. N is the number of layers. The one-way transmission loss for a normal incidence is given by

$$T_{VSP}(N)=\prod_{k=1}^{N}\left[1-R_k\right], \tag{5.3}$$

where T_{VSP} represents the transmission coefficients. The ratio of T_{sur} and T_{VSP} is

$$\frac{T_{sur}(N)}{T_{VSP}(N)}=\prod_{k=1}^{N}\left[1+R_k\right], \tag{5.4}$$

which means that for the same layered sequence we need to amplify the VSP wavelet to compensate the difference in transmission loss. From the nonstationary trace model expressed by equation 3.3, if we can properly factorize the wavelet and reflectivity the wavelet estimates will have no relationship with the transmission loss, but the VSP wavelet does experience the amplitude decay caused by the transmission loss. In principle, this loss can be calculated from the log data. However, compensation for this effect is not considered in this thesis.

3. Geophone directivity

In this thesis, the wavelets were estimated from the vertical components of the middle-offset surface and zero-offset VSP data. The amplitude of the wavelet estimate at a horizontal shot-receiver offset is given by

$$V=A\cos(\theta), \tag{5.5}$$

where A and V are the amplitude of the wavelet estimate and its vertical component, and θ is the emergence angle. For middle-offset surface data, θ increases with increasing offset, while for zero-offset VSP data, θ is equal to zero. The ratio of the vertical components between VSP and surface data is $\cos(\theta)$. In the real case, θ is small due to the very low velocity of the near surface layer. Thus in our research, the effect of the geophone directivity is ignored. This may cause large differences between the wavelet estimates from shallow surface and VSP data.

4. **Difference in constant-Q attenuation**

If Q is independent of the direction of wave propagation, the nonstationary surface wavelet is expressed by

$$\hat{w}_{sur}(t_2,\omega) = w(\omega)e^{-\frac{\omega t_2}{2Q}+i\frac{t_2}{2Q}H(\omega)}, \tag{5.6}$$

where $\hat{w}_{sur}(t_2,\omega)$ denotes the spectrum of the wavelet estimate from surface data and $w(\omega)$ is the spectrum of the source signature. The nonstationary VSP wavelet can be written as

$$\hat{w}_{VSP}(t_1,\omega) = w(\omega)e^{-\frac{\omega t_1}{2Q}+i\frac{t_1}{2Q}H(\omega)}, \tag{5.7}$$

where $\hat{w}_{VSP}(t_1,\omega)$ is the spectrum of the wavelet estimate from VSP data. Since surface and VSP data shared the same source signature in our case, the spectral ratio of the VSP and surface wavelets is given by

$$\frac{\hat{w}_{sur}(t_2,\omega)}{\hat{w}_{VSP}(t_1,\omega)} = e^{-\frac{t_2-t_1}{2Q}\omega+i\frac{t_2-t_1}{2Q}H(\omega)}, \tag{5.8}$$

where traveltime t_1 and t_2 are calculated from equation (4.1). Equation (5.8) is actually a Q filter. Q can be estimated from VSP downgoing waves.

5.2 Q estimation

As an intrinsic property of the rock, Q is a ratio of stored energy to dissipated energy, but the Q estimates from seismic data do not exactly represent this property. The errors in Q estimates are closely related to data acquisition and processing. Intrabed multiples, scattering and mode conversion also contribute to Q estimation since their effects are similar to Q attenuation (Tonn, 1991). Therefore what we estimate is actually an effective Q which includes the intrinsic property of the rock and interference from the other factors. Q estimates from VSP downgoing waves are more reliable than those from the surface or log data (White, 1992). Among many approaches available for Q estimation, the spectral-ratio method is more reliable and accurate if the data are noise-free (Tonn, 1991). In the spectral-ratio method, the relation of the amplitude spectrum $A(Z,f)$ of the trace recorded at a deeper geophone level, Z, and the reference amplitude spectrum $A_0(Z_0,f)$ at a shallow level, Z_0, is expressed as

$$A(Z,f)=A_0(Z_0,f)e^{-\alpha(Z-Z_0)}, \tag{5.9}$$

where α is attenuation coefficient given by

$$\alpha=\pi f/Qv. \tag{5.10}$$

This means

$$\ln\left(A(Z,f)/A_0(Z_{0,}f)\right)=-\pi f(T-T_0)/Q, \tag{5.11}$$

where T and T_0 are the P-wave arrival time at geophone levels, Z and Z_0, respectively. By a linear fit to the data points in a crossplot of $\ln\left(A(Z,f)/A_0(Z_{0,}f)\right)$ versus f, Q can be estimated from equation (5.11).

Here we use the amplitude spectra of the VSP wavelet estimates (as shown in Figure 4.21 (b)) to estimate Q by a linear fitting to the log spectral ratio between the wavelet estimate at each deeper level and the wavelet estimate at the shallowest level. A frequency-domain boxcar smoother with a 30 Hz length was applied to the log spectral ratio before the linear fitting. The linear fitting was done over the frequency range from 8 to 70 Hz. Both the log spectral ratios and the fitted straight lines are shown in Figure 5.2 (only every second ratio line was shown for display purpose).

The slope of the fitted straight line increases from the shallow level to the deep level. The standard deviation of the slope is given by (Draper and Smith, 1981)

$$\delta S(Z) = \frac{S(Z)}{\sqrt{S_{xx}}}, \tag{5.12}$$

where $S(Z)$ is standard deviation of the spectral ratio, which is written as

$$S(Z) = \left[\frac{1}{K} \sum_{1}^{K} \left[\ln\left(A(Z, f_k) / A_0(Z_0, f_k)\right) - a(Z) - b(Z) f_k \right] \right]^{1/2}, \tag{5.13}$$

where $a(Z)$ and $b(Z)$ are the intercept and the slope of the fitted straight line. They were given by

$$a(Z) = \frac{1}{K} \sum_{1}^{K} \ln\left(A(Z, f_k) / A_0(Z_0, f_k)\right) - b(Z) \frac{1}{K} \sum_{1}^{K} f_k, \tag{5.14}$$

and

$$b(Z) = \frac{S_{xy}(Z)}{S_{xx}}, \tag{5.15}$$

where

$$S_{xy}(Z) = \sum_{1}^{K} \left[f_k \ln\left(A(Z, f_k) / A_0(Z_0, f_k)\right) \right] - \frac{1}{K} \sum_{1}^{K} f_k \sum_{1}^{K} \ln\left(A(Z, f_k) / A_0(Z_0, f_k)\right), \tag{5.16}$$

and

$$S_{xx} = \sum_{k=1}^{K} f_k^2 - \frac{1}{K} \left(\sum_{k=1}^{K} f_k \right)^2, \tag{5.17}$$

where K is the number of the frequency components within the selected frequency range. The error in average-Q estimate caused by the standard deviation of the slope is expressed by

$$\delta Q(Z) = \left| \delta S(Z) \right| \frac{Q^2}{\pi \Delta t}, \tag{5.18}$$

where Δt is the traveltime when wave travels from the depth Z_0 to Z.

The standard deviation in the slope of the fitted straight line and the error in average-Q estimate are shown in Figure 5.3 where the deviation grows with increasing depth while the error in the average-Q estimate roughly decreases with increasing depth. Figure 5.4 shows the average Q estimates between the shallowest receiver level and each deeper level. The relative error in Q estimates is less than 7 percent as shown in Figure 5.4.

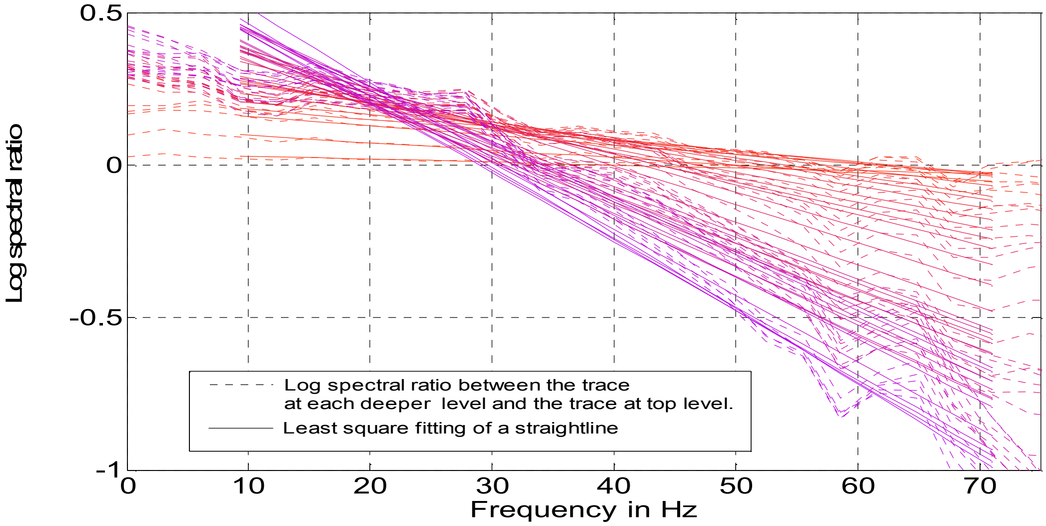

Figure 5.2 Log spectral ratios and their linear fits in a sense of the minimum square root. The dip of the straight line is proportional to Q estimates.

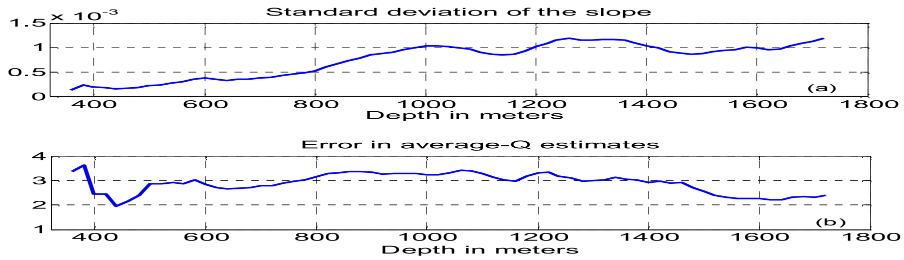

Figure 5.3 Standard deviation in the slope of the fitted straight line (a) and the errors in average-Q estimates (b).

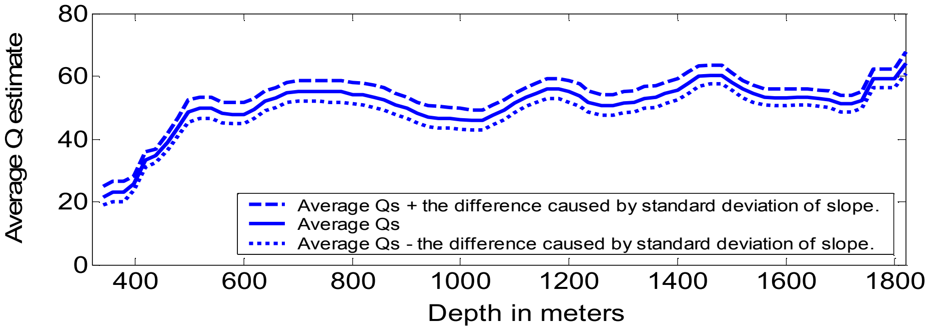

Figure 5.4 Average Q estimate and the error in the Q estimate caused by the error in the slope of the fitted straight line.

The attenuation from Q estimates can be applied back to the reference wavelet (the wavelet at shallowest level) to generate a group of simulated wavelets. By comparing these simulated wavelets with the wavelet estimates, we can assess the accuracy of the Q estimates. Figure 5.5 shows the wavelet estimates and simulated wavelets alternately in subplot (a), and their corresponding amplitude spectra in subplots (b). Similarity between the simulated wavelets and wavelet estimates implies that our average Q estimates are reasonable. This is also shown by comparing the amplitude spectra.

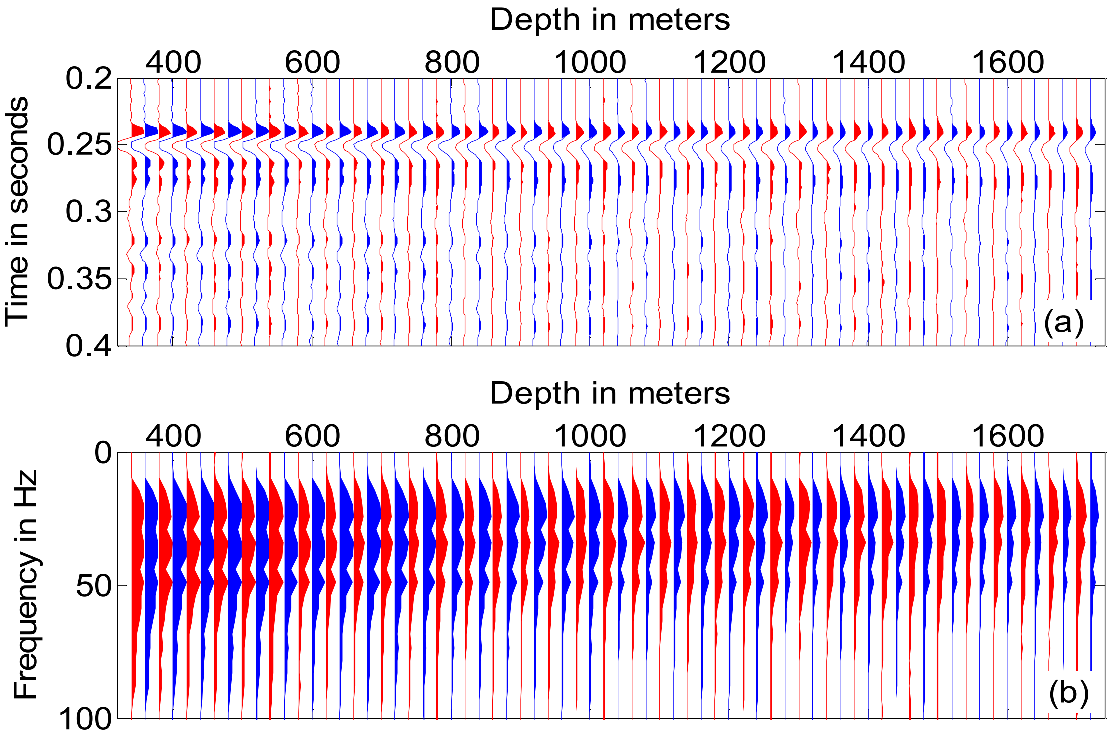

Figure 5.5 (a) Wavelet estimates and simulated wavelets plotted alternately. The red one is the estimated wavelet and the blue one is the simulated wavelet in each wavelet pair. (b) Fourier amplitude spectra corresponding to the wavelets shown in (a).

5.3 **Comparing wavelet estimates from the synthetic VSP and surface data**

In chapter two, we have simulated both VSP and surface wavelets from the same horizontal layered model and source signature, as shown in figures 2.2 (a) and 2.7. Since the effects of reflection, transmission and spherical divergence are not included in the synthetic data, any differences between the wavelets are due to the attenuation effect.

Equation (5.8) was used as a Q filter to match the VSP wavelets to surface wavelets. In this case, t_1 and t_2 are directly measured from the synthetic seismograms and average Q was calculated by

$$Q_a(n) = \frac{\sum_{i=1}^{n} \Delta t_i}{\sum_{i=1}^{n} \Delta t_i / Q_i}, \tag{5.19}$$

where Q_a and Q_i are average Q and given interval Q (shown in Table 2.1). Δt and n are interval traveltime and the number of layers.

To carry out the wavelet comparison, at first we chose the VSP wavelets received at the depth level of two reflectors, corresponding to the fifth and fourteenth traces shown in Figure 2.7, then design forward Q filters at different horizontal offsets using equations (4.1) and (5.8), and finally apply these filters to selected VSP wavelets. Figure 5.6 shows a qualitative comparison of Q-filtered VSP wavelets and wavelets received on the surface. The top six wavelets are three Q-filtered VSP wavelets received at 500 m depth and the other three wavelets reflected from the first reflector and received on the surface. The bottom six wavelets consist of three Q-filtered VSP wavelets received at 1500 m depth and three wavelets reflected from the second reflector. Both Q-filtered VSP wavelets and surface wavelets are consistent in wave shape although there are small differences with increasing horizontal offsets.

Figure 5.7 shows the amplitude spectra of the Q-filtered VSP wavelets have similar db down to these of simulated wavelets on the surface at the same frequency.

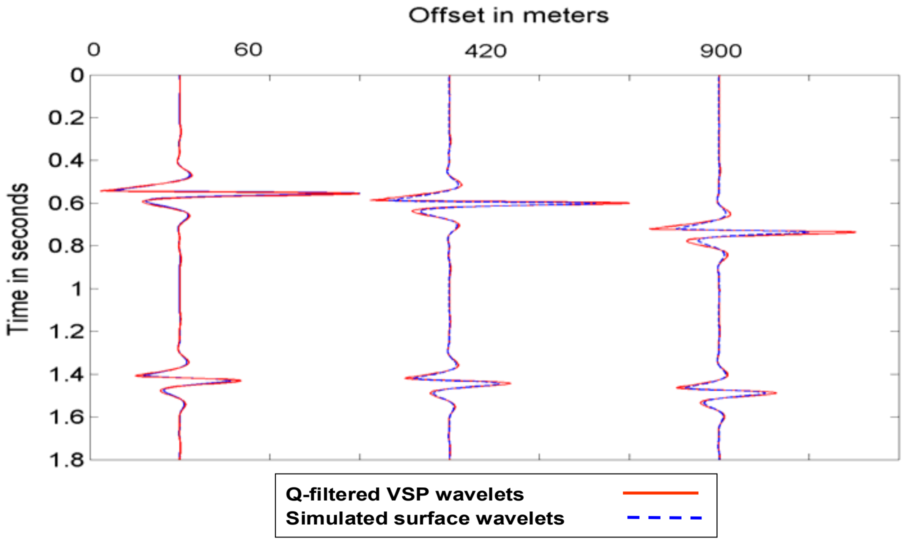

Figure 5.6 Comparison of Q-filtered synthetic VSP wavelets to synthetic surface wavelets.

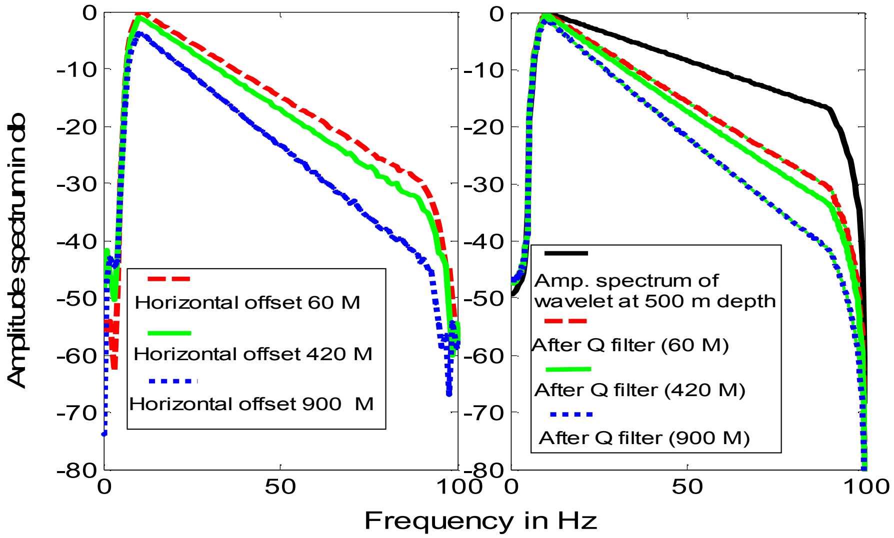

Figure 5.7 Amplitude spectrum simulation at 60, 420 and 900 m horizontal offset from borehole (left) and amplitude spectra of the Q-filtered wavelet from 500 m depth (right).

We can also simulate the VSP wavelet by inverse Q filtering of surface wavelet. Since equations (1.9) and (1.14) are equivalent when Q is assumed to be independent of frequency, equation (1.9) can be transferred into an inverse Q filter by simply changing the sign of the terms within the parentheses and letting

$$\frac{\vec{b}\cdot\vec{x}}{v_{ref}} = t_2 - t_1 = \Delta t \; . \tag{5.20}$$

Then we can relate the simulated surface wavelet to the VSP wavelet by

$$\hat{w}_{vsp}(t_{1,}\omega) = \hat{w}_{sur}(t_2,\omega)\exp\left\{\Delta t\omega\left[\frac{\operatorname{sgn}(\omega)}{2Q} - \frac{i}{\pi Q}\ln\left|\frac{\omega}{\omega_{ref}}\right|\right]\right\}\exp(i\Delta t\omega), \tag{5.21}$$

Figure 5.8 shows the VSP wavelet (most left trace) received at the first reflector and inverse Q filtered surface wavelets reflected from the same reflector. The waveforms of the VSP wavelet and inverse Q filtered surface wavelet are nearly the same. Figure 5.9 shows the amplitude spectra corresponding to the wavelets shown in Figure 5.8. Again the amplitude spectra of inverse Q filtered surface wavelets are consistent with that of the VSP wavelet.

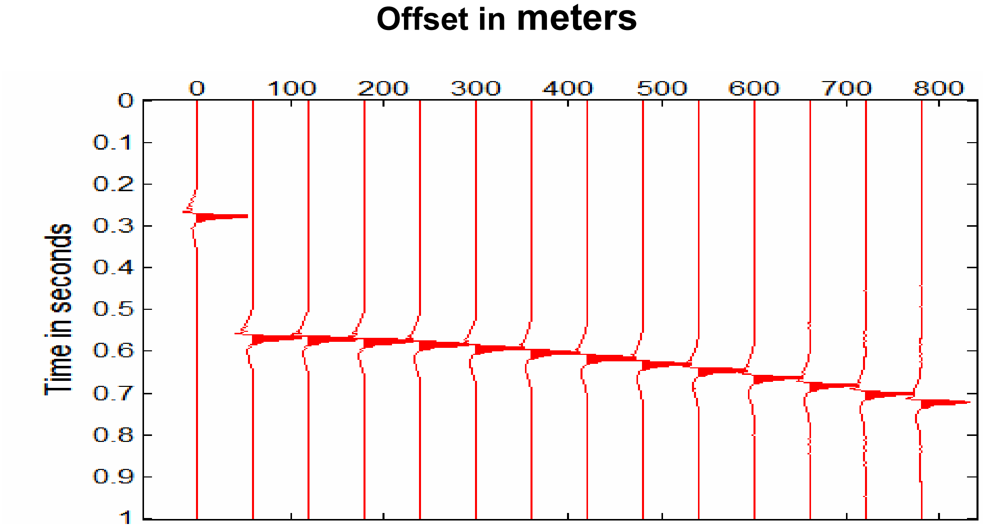

Figure 5.8 VSP wavelet (the most left pulse) and inverse-Q-filtered wavelets simulated on the surface.

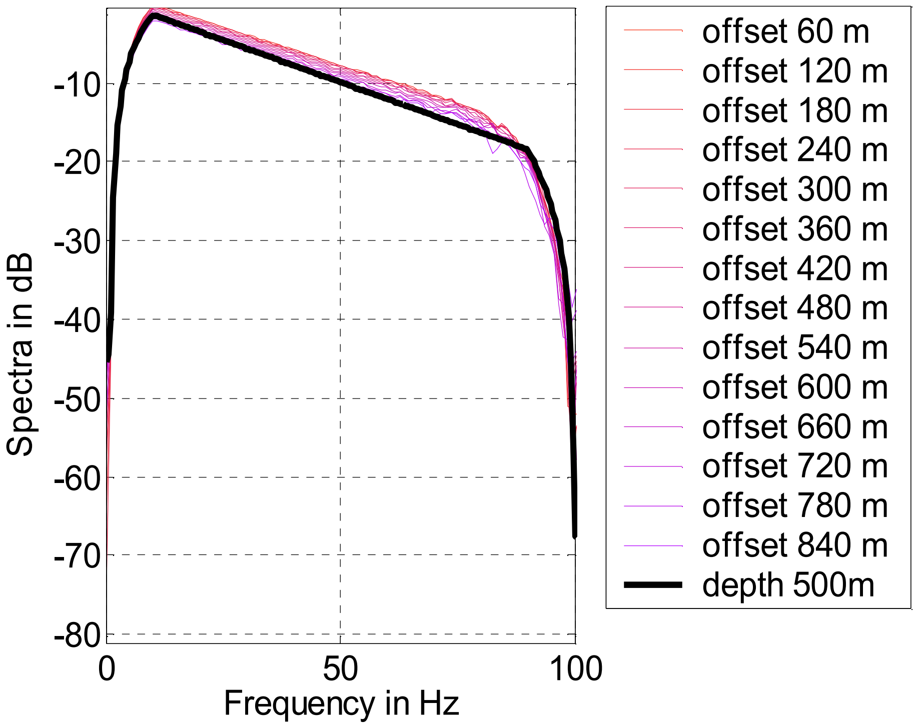

Figure 5.9 Amplitude spectrum of the VSP wavelet (thick curve) and amplitude spectra of inverse-Q filtered wavelets simulated on the surface.

In conclusion of this section, wavelets simulated both in the well and on the surface can be transformed into each other by the forward Q filtering or the inverse Q filtering if only the constant-Q attenuation is included in the wavefield propagation.

5.4 Comparing wavelet estimates from real VSP and surface data

Up to now we have estimated the nonstationary wavelets from the surface and VSP data, and also estimated Q values from VSP wavelet estimates. Similar to what was done on the simulated wavelets in Section 5.3, we will now compare the wavelet estimates from the real data.

5.4.1 Forward-Q filtering for wavelet comparison

Since VSP wavelets travel a much shorter distance compared to the corresponding surface wavelet estimates, VSP wavelets experience less attenuation than those from surface data. Therefore, it is necessary to filter the VSP wavelet estimates for comparison of the VSP wavelets and surface wavelets. The *Q* estimates, VSP traveltime picked from real VSP data and the two-way surface traveltime were used to design forward-Q filters from equation (5.8). These filters were then applied to VSP wavelet estimates to make them comparable to the wavelet estimates from the surface data.

Figure 5.10 shows the VSP wavelet estimates and their Q-filtered counterparts (every eighth wavelet was shown for display purpose). Figure 5.11 shows the amplitude spectra of VSP wavelet estimates and Q-filtered VSP wavelets. After Q filtering, the high frequency components were obviously attenuated and dominant frequencies shifted toward low frequency direction with increasing traveltime.

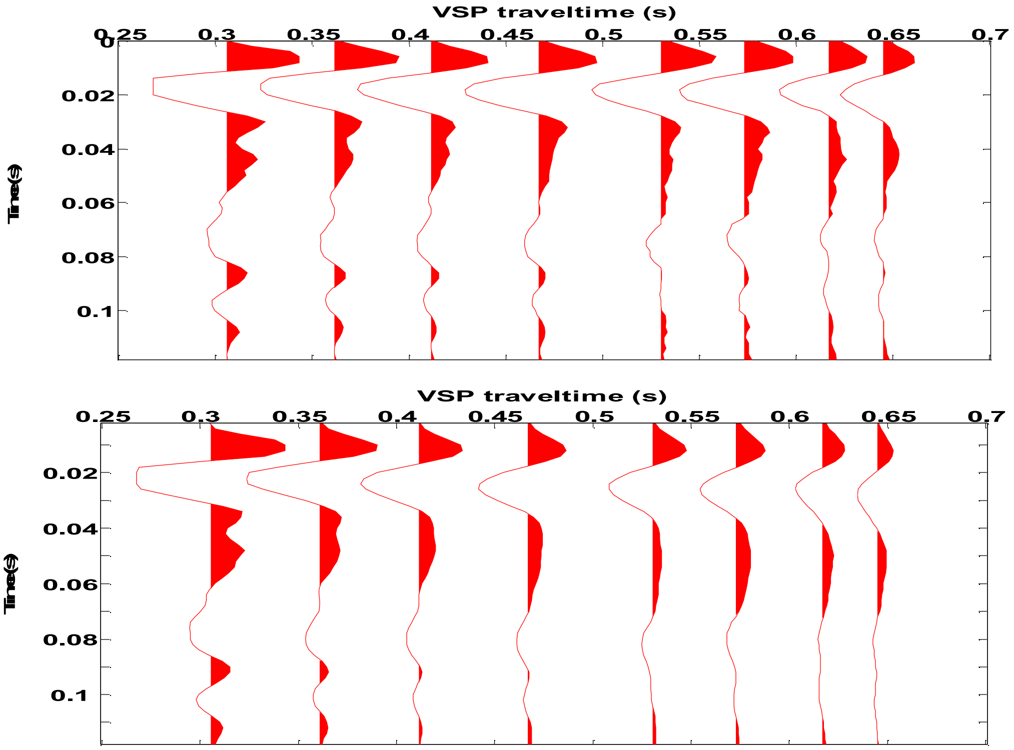

Figure 5.10 VSP wavelets (top) and Q-filtered VSP wavelets (bottom).

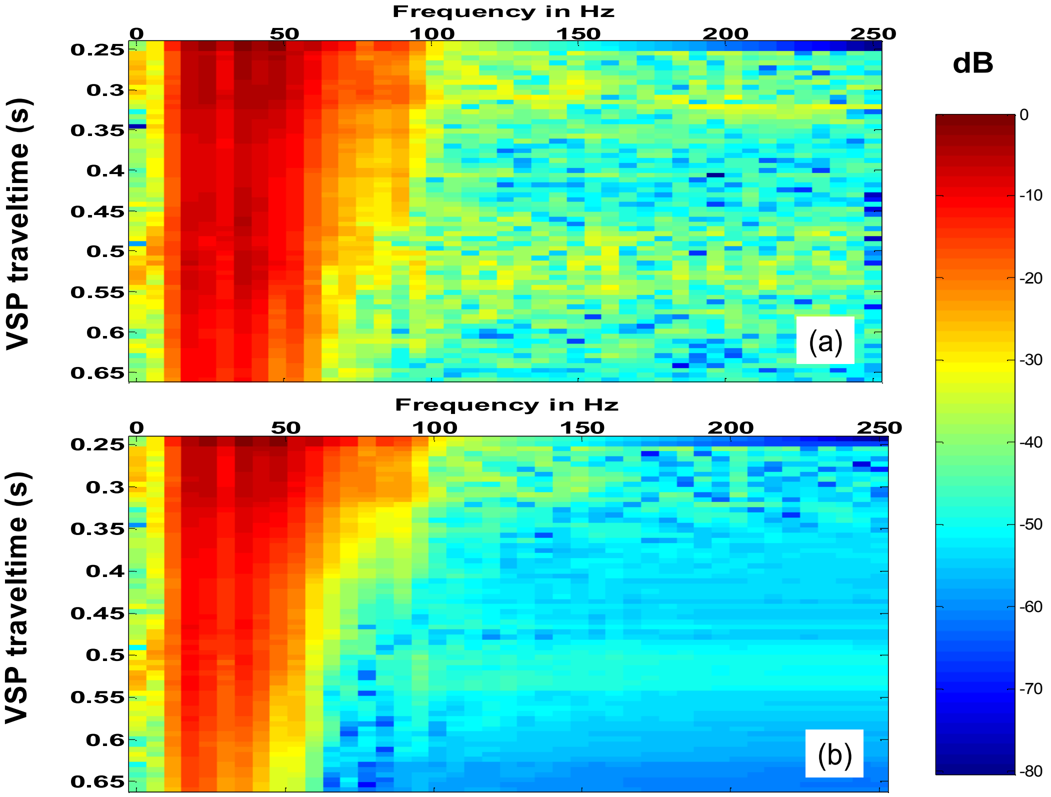

Figure 5.11 Amplitude spectra of the VSP wavelets (a) and amplitude spectra of Q-filtered VSP wavelets (b).

5.4.2 Comparison of wavelet estimates from surface data and forward-Q filtered VSP wavelets

We follow standard practice to estimate wavelets by the Wiener deconvolution approaches. At first, a 0.1 s length AGC was applied to the pre-processed seismic data, then the wavelet was estimated on the gained data in a 0.2 s length boxcar window that moved down the trace in an increment of 0.02 s. Finally, the wavelet estimates located at the surface traveltime corresponding to each VSP traveltime were selected for comparison with the Q-filtered VSP wavelets. Figure 5.12 shows the wavelet estimates by both time-domain and frequency-domain Wiener deconvolution methods. Only every eighth wavelet was shown. The wavelets from both approaches are very similar except that the wavelets from the later method are more consistent with each other after the boxcar smoother with the width of 10 Hz was applied. Apparently, the gain in the wavelet estimates doesn't agree with that in Q-filtered VSP wavelets since the conventional Wiener methods can not exactly estimate the gain function. Figure 5.13 shows Fourier amplitude spectra of the wavelets by Wiener approaches. The dominant frequency decreases with the increasing traveltime but the band pass doesn't change with the traveltime, which is different from the band pass of the Q-filtered VSP wavelet estimates.

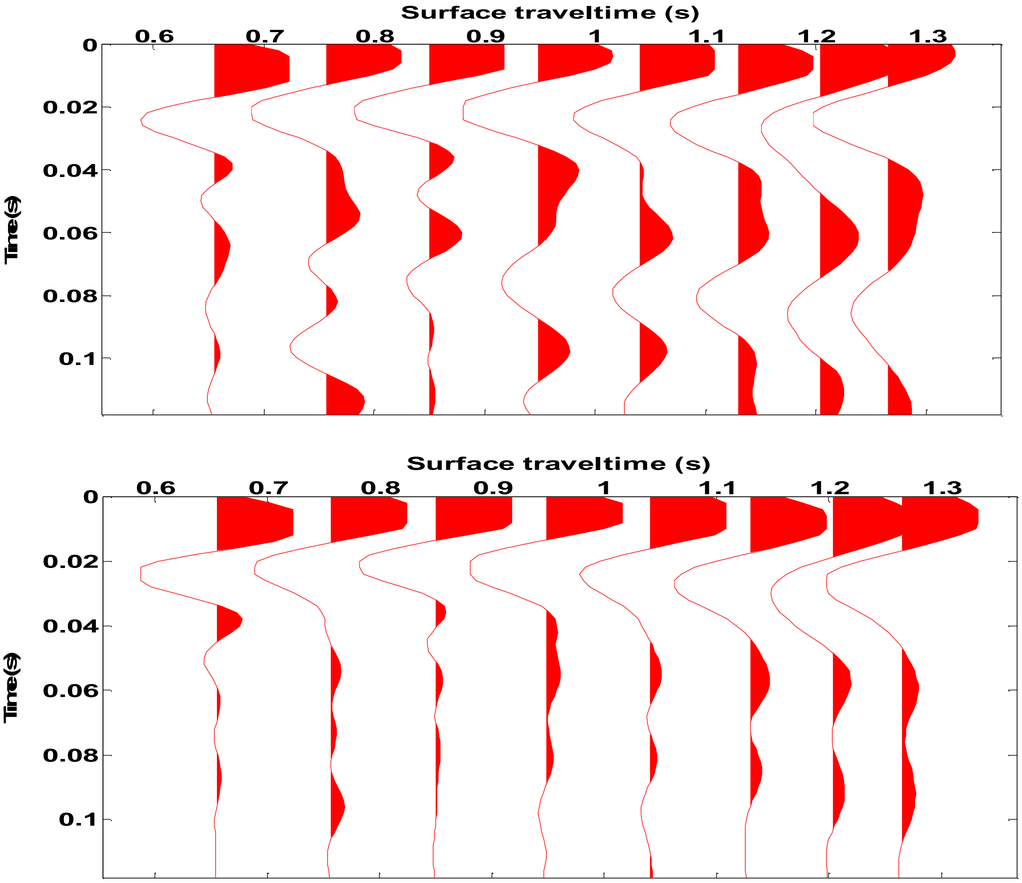

Figure 5.12 Wavelet estimates by time-domain Wiener deconvolution (top) and frequency-domain Wiener deconvolution (bottom).

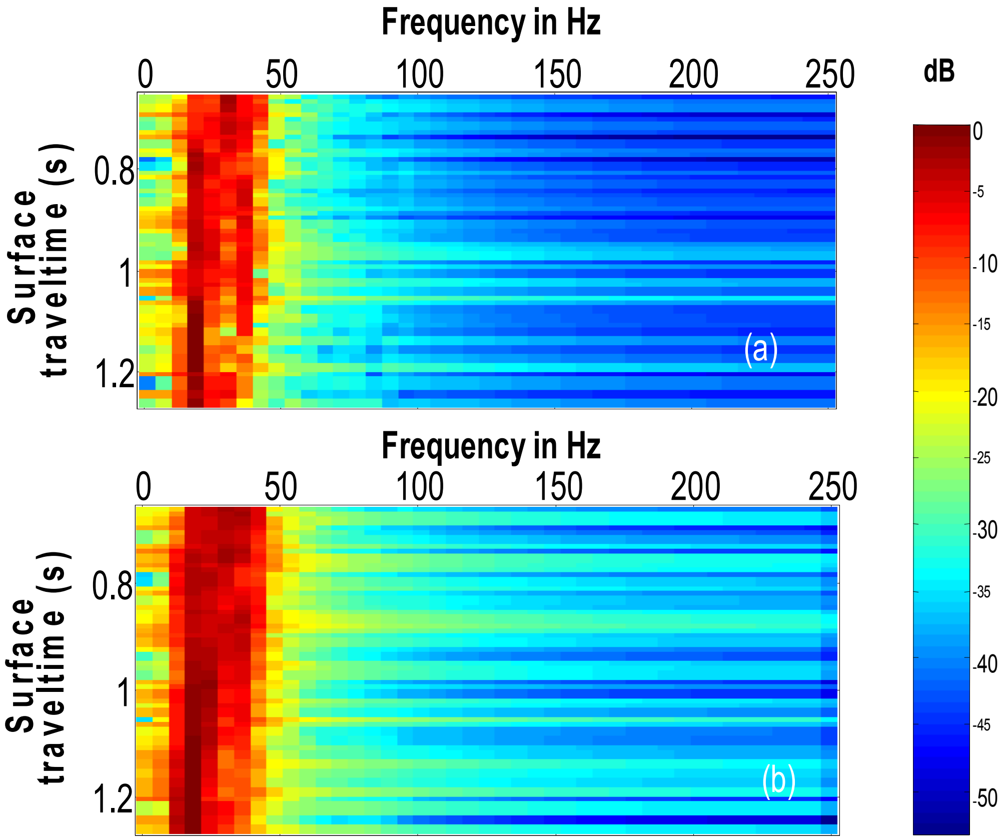

Figure 5.13 Fourier amplitude spectra of the wavelet estimates by the time-domain Wiener deconvolution (a) and the frequency-domain Wiener deconvolution (b).

Gabor wavelets were estimated on the pre-processed seismic data without any gain applied, with both the boxcar and the hyperbolic smoother. The procedure of the wavelet estimation is the same as we described in Section 3.5.2. A temporally short Gaussian window with half length of 0.2 s was used in Gabor method with the hyperbolic smoother. The same window was applied in Gabor approach with a time-frequency boxcar smoother of 10 Hz long and 0.3 s wide. Figure 5.14 shows the Gabor wavelet estimates with the boxcar smoother (top) and the hyperbolic smoother (bottom). The waveform of the wavelet estimates agree quite closely with that of the Q-filtered VSP wavelet estimates. Figure 5.15 shows the amplitude spectra of the Gabor wavelet estimates with two different smoothers. The features of the amplitude spectra with the hyperbolic smoother, such as dominant frequency variation and the band pass change with the increasing traveltime, are very consistent with those of the Q-filtered VSP wavelet estimates. Therefore we conclude that the wavelet estimates by the Gabor deconvolution with the hyperbolic smoother are the most accurate among all the wavelet estimates.

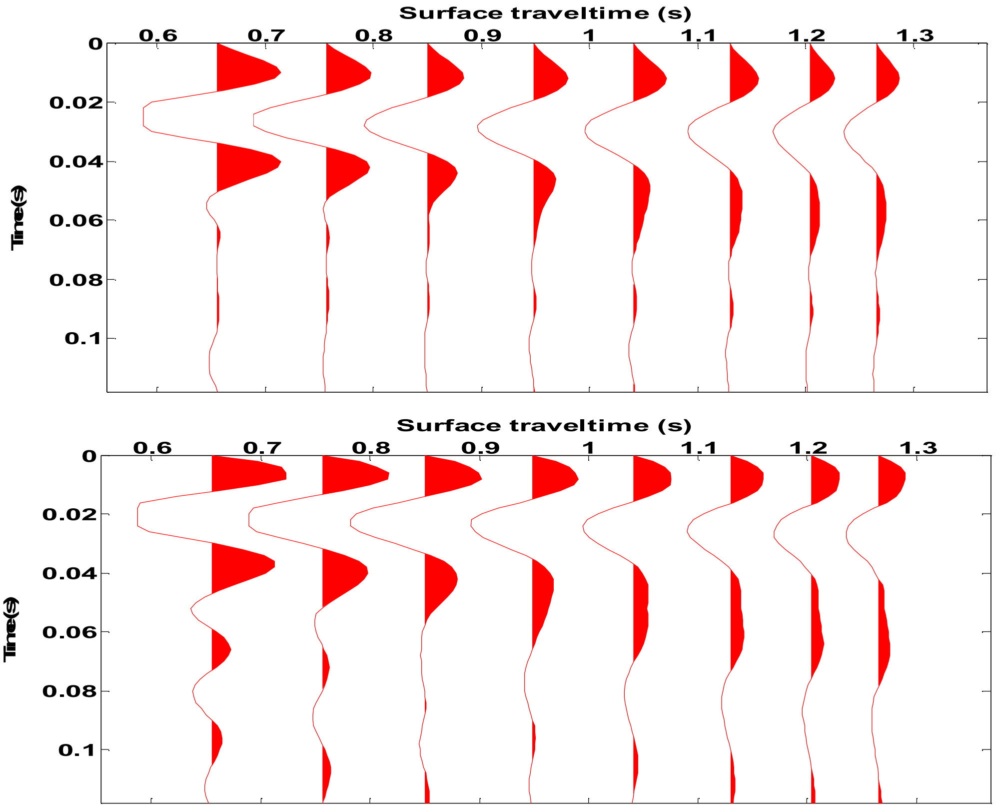

Figure 5.14 Wavelet estimates by Gabor deconvolution with the time-frequency domain boxcar smoother (top) and hyperbolic smoother (bottom).

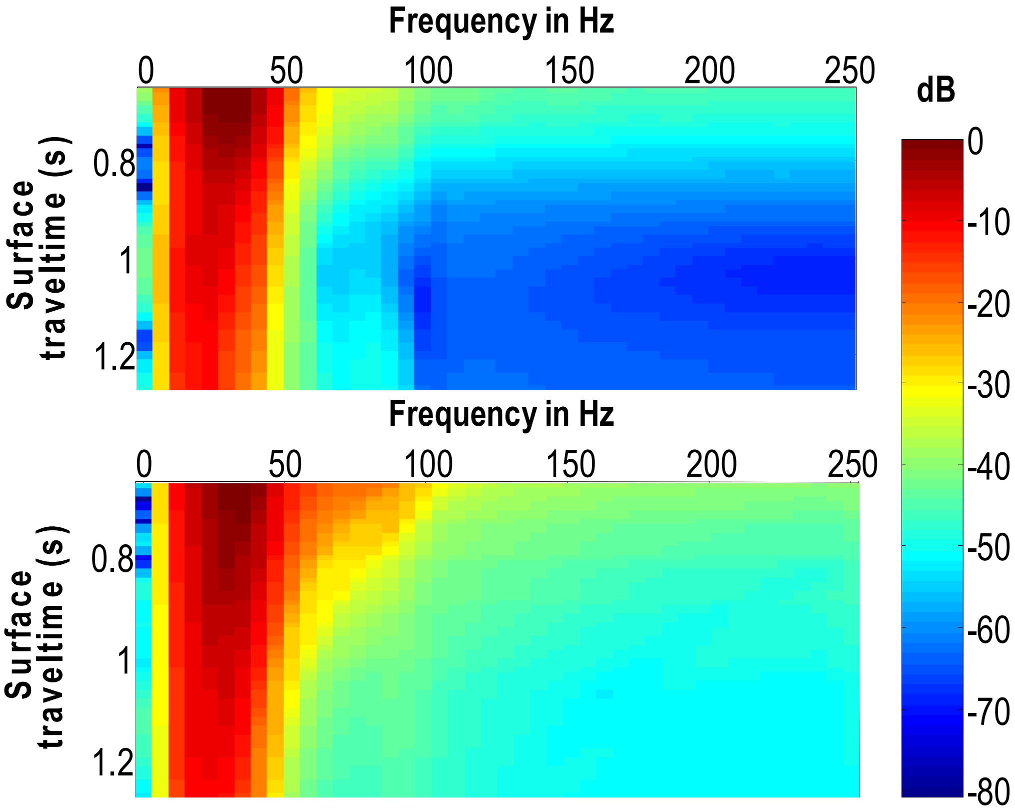

Figure 5.15 Fourier amplitude spectra of the wavelet estimates by Gabor deconvolution with the boxcar smoother (a) and with the hyperbolic smoother (b).

Figure 5.16 shows the maximum values of normalized crosscorrelation between wavelet estimates by four methods and Q-filtered VSP wavelets. From the figure, we observe that the wavelets from Gabor deconvolution using hyperbolic smoother apparently win out especially at a later time.

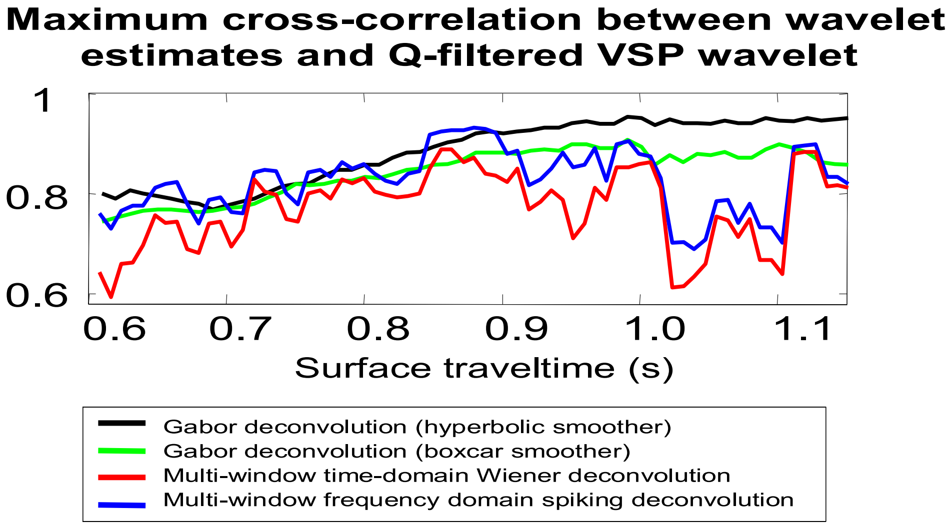

Figure 5.16 Maximum crosscorrelation of the wavelet estimates and the Q-filtered VSP wavelets.

5.4.3 Comparison of wavelet estimates from VSP data and inverse-Q filtered surface wavelet estimates

Contrary to application of the forward-Q filter to VSP wavelets, we also can process the wavelet estimates from surface data by inverse-Q filtering and then compare them with VSP wavelet. This inverse-Q filter is designed by equation (5.21).

Figure 5.17 shows the inverse-Q filtered wavelets from surface data. The top figure shows the wavelets by Gabor deconvolution with the boxcar smoothing and the bottom one shows the wavelets by Gabor deconvolution with the hyperbolic smoothing. Comparing the wavelets in Figure 5.17 to the corresponding wavelets shown on the top in Figure 5.10, the dominant frequency and the peak amplitude of the surface wavelet with the hyperbolic smoothing is closer to the VSP wavelet.

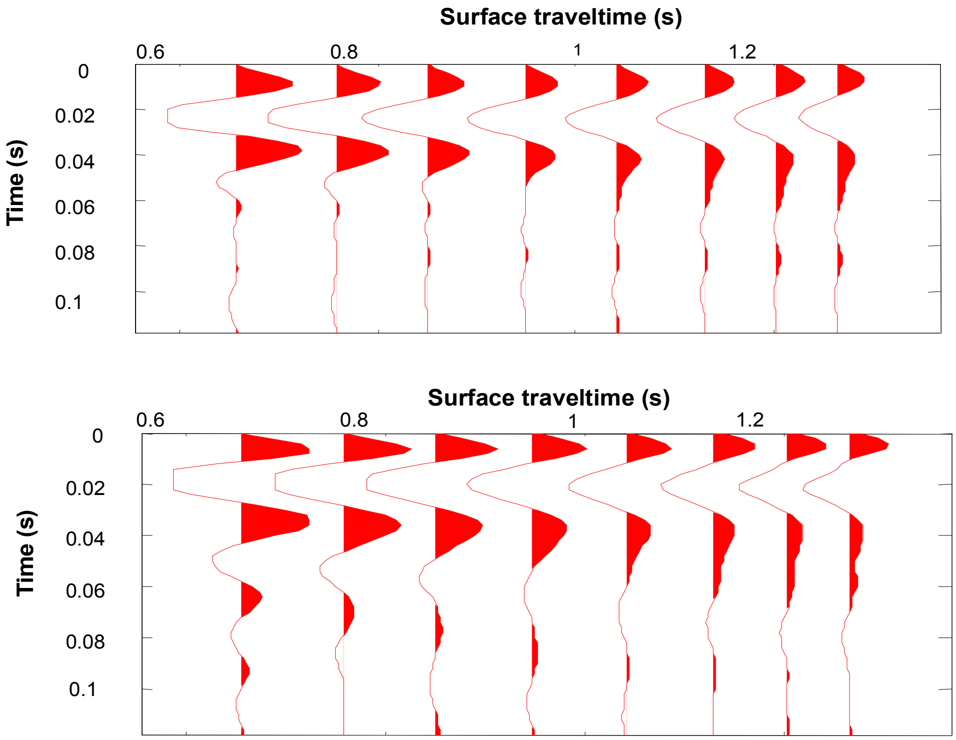

Figure 5.17 Inverse-Q filtered wavelet estimates from Gabor deconvolution with boxcar smoothing (top) and hyperbolic smoothing (bottom).

Figure 5.18 shows inverse-Q filtered amplitude spectra of the surface wavelets. The amplitude spectra shown on the top of Figure 18 are calculated from the wavelets estimated by Gabor deconvolution with the boxcar smoothing and the bottom spectra are from Gabor deconvolution with the hyperbolic smoothing. Comparing Figure 5.18 to Figure 5.11 (a), we find that the amplitude spectra after hyperbolic smoothing are more consistent with the spectra of VSP wavelets.

Figure 5.19 shows the maximum crosscorrelation between the inverse-Q filtered surface wavelets and VSP wavelets (top), and the lags of the maximum crosscorrelation coefficients. It is obvious that the surface wavelets from Gabor deconvolution with the hyperbolic smoothing are closer to VSP wavelets than those with the boxcar smoothing. The lag curves show that there is no phase shift between the wavelets with hyperbolic smoothing and VSP wavelets.

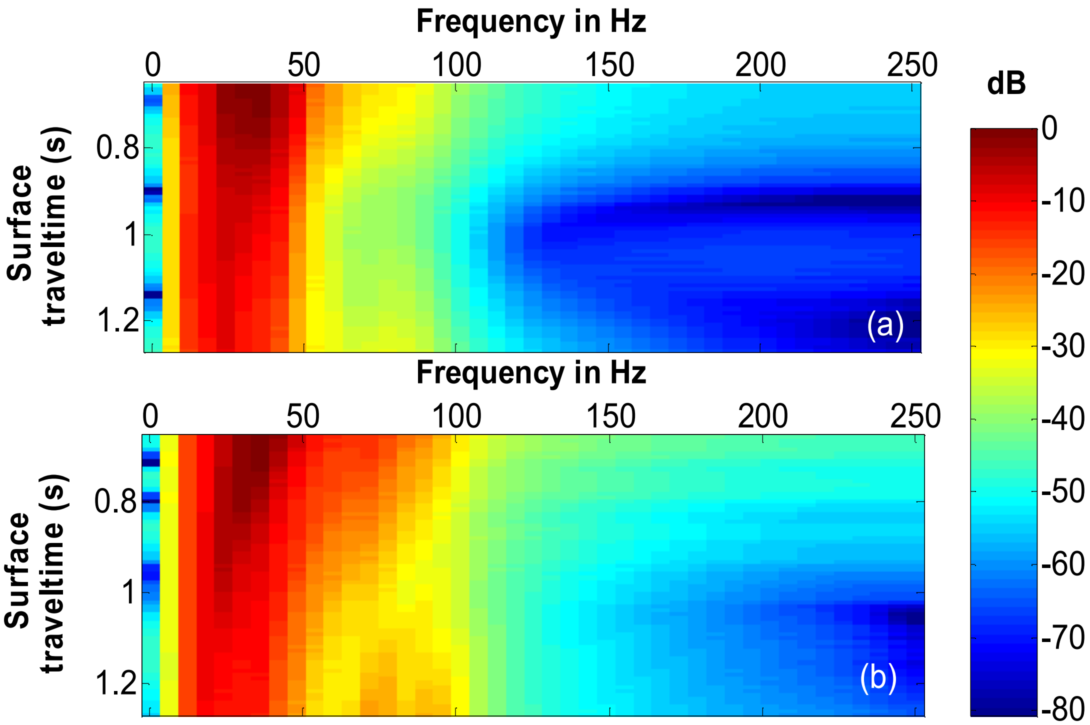

Figure 5.18 Inverse-Q filtered amplitude spectra of the wavelets by Gabor deconvolution with boxcar smoothing (a) and hyperbolic smoothing (b).

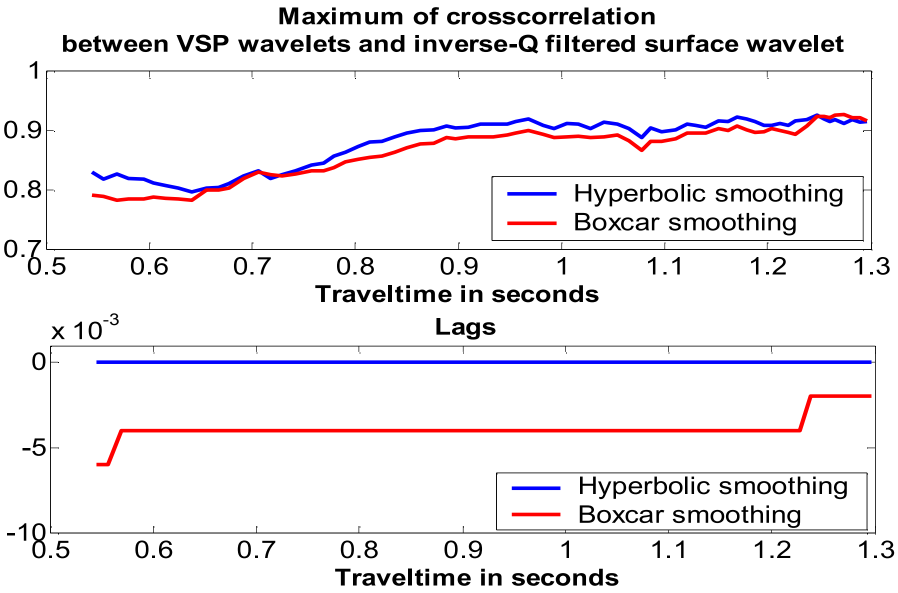

Figure 5.19 Maximum crosscorrelation between VSP wavelets and inverse-Q filtered surface wavelets (top), and lags of the maximum crosscorrelation coefficients (bottom).

5.5 Chapter summary

First the simulated VSP wavelets and surface wavelets were compared each other. This comparison shows that the VSP wavelets can be quite close to the surface wavelets after either forward-Q filtering the former or inverse-Q filtering the latter. This result suggests that the wavelet estimates from VSP data can be used to evaluate the wavelet estimated from the surface data. Then we estimated Q values from the VSP downgoing wavelets and compared the forward-Q filtered VSP wavelets to the surface wavelets that were estimated by four different methods described in Chapter 3. Finally we compared the VSP wavelets with the inverse-Q filtered surface wavelets. Our results are consistent with the hypothesis that Gabor deconvolution can accurately estimate the nonstationary wavelets embedded in real seismic records. Gabor deconvolution is superior to a multi-window Wiener or frequency domain spiking deconvolution. Therefore, the Gabor deconvolution is validated by comparison of the wavelet estimates from VSP and surface data.

The accuracy of Q estimates depends on the slope of the least-square-fitted straight line. The result of the error analysis in this chapter is consistent with White's statement (1992) that the error in Q estimates decreases with increasing depth.

CHAPTER 6 GENERAL CONCLUSIONS AND POSSIBLE EXTENSIONS

6.1 Conclusions and discussions

In this thesis, we first simulated the nonstationary VSP and surface wavelets using complex ray approaches. We found that the surface wavelets quite closely resemble the forward-Q filtered VSP wavelets and also the VSP wavelets were very similar to the inverse-Q filtered surface wavelet. This result suggests that the accuracy of the nonstationary wavelet estimate can be verified by comparison of wavelet estimates from surface and VSP data. Then we extracted wavelets from a simultaneously recorded VSP and surface data provided by EnCana and compared the VSP and surface wavelet estimates using the same approach as that for the simulated wavelets. The result shows that the nonstationary wavelet estimated from Gabor deconvolution agrees more closely with Q-filtered VSP wavelets than that from the conventional Wiener deconvolution methods. Since the nonstationary wavelet is directly recorded in VSP downgoing waves, the agreement between wavelet estimates from surface data and VSP wavelets shows that Gabor deconvolution can accurately estimate the nonstationary wavelet.

The second validation is based on the synthetic seismic data which were the convolution between the simulated nonstationary wavelet and the reflectivity estimated from real log data. The wavelet estimates from the synthetic data by Gabor deconvolution are quite close to the simulated nonstationary wavelet. Therefore, the accuracy of the Gabor deconvolution is verified by synthetic data also.

In addition to Gabor deconvolution, conventional time-domain and frequency-domain multi-window Wiener deconvolution were also applied in nonstationary wavelet estimation. Our results suggest that Gabor deconvolution is superior to Wiener methods.

Gabor methods include a gain correction which can affect the amplitude of the nonstationary wavelet estimates. The parameter testing in wavelet estimation shows that the amplitude of the wavelet estimates changes with the window length. A wider window will yield less amplitude decay.

We also examined the phase property of the real VSP observations from the vibroseis source by the time-domain Wiener deconvolution. It is surprising that VSP observations did not require a phase rotation to agree with the minimum phase assumptions of the deconvolution algorithms. Although the wavelet estimates from the vibroseis recordings may be a little bit of departure from minimum phase assumptions, this research shows that they can be quite accurately extracted by Gabor deconvolution methods.

In this thesis, we developed several approaches in nonstationary wavelet simulation including the methods for the nonstationary VSP wavelet simulation by complex ray tracing, zero-offset VSP seismogram with attenuation by 1-D wavefield extrapolation, and extended 2-D frequency-space domain 45-degree wave equation from an acoustic medium to a viscoacoustic medium. Each approach in the wavelet simulation has its own advantages and weak points. Complex ray tracing method is the most accurate because it is a theoretic solution for the plane wave propagating in the horizontally layered anelastic medium, but this method doesn't always guarantee the convergence in the complicated medium model. 1-D wavefield extrapolator for zero-offset VSP downgoing and upcoming waves is a numeric solution of the 1-D and two-way wave equation for a plane compressional wave propagating in the horizontally layered anelastic medium. This approach always gives the solution no matter how many layers the model has. As a numerical solution, it is less accurate than complex ray methods. 2-D frequency-space domain 45-degree wave equation can simulate the nonstationary wavelet in more complicated medium with the constant-Q attenuation, but it works slowly if we use the finite difference method.

6.2 Possible extensions

Q filtered wavelet estimates from VSP data can be used for shaping the wavelet estimates from surface data by a match filter, especially in the case of the joint VSP and surface acquisition since the wavelet estimates from surface and VSP data are much more comparable. Shaped wavelet estimates can possibly improve the accuracy of the nonstationary deconvolution.

Gabor deconvolution can be implemented in a surface consistent manner based on the wavelet estimates from multi-trace gather such as wavelet stacking used in this research. It is possible to increase the lateral consistency of the deconvolved trace by using the average wavelets estimated from more than one trace. On the other hand, this approach can further suppress the noise effect on wavelet estimates. Lateral nonstationarity caused by attenuation versus offset can be controlled by the spatial window length.

The wavefield extrapolator including constant-Q attenuation factor can easily be used in seismic migration to obtain more accurate migration amplitude.

Bibliography

Aki, K. and Richards, P. G., 1980, Quantitative Seismology: Theory and Methods, 2, W. H. Freeman and Company.

Baeten, G. and Ziolkowski, A., 1990, The vibroseis source, Elsevier Science Publishing Company INC. New York, U.S.A.

Bickel, S. H., 1982, The effects of noise on minimum-phase vibroseis deconvolution: Geophysics, 47, 1174-1184.

Bickel, S. H., and Natarrajan, R., R, 1985, Plane-wave Q deconvolution: Geophysics, 50, 1426-1439.

Brittle, K. F., 2001, Vibroseis deconvolution: frequency-domain: M.Sc. thesis, University of Calgary, AB.

Brötz, R., Marschall, R. and Knecht, M., 1987, Signal adjustment of vibroseis and impulsive source data: Geophysical Prospecting, 35, 739-766.

Carcione, J. M., 1993, Seismic modeling in viscoelastic media: Geophysics, 58, 110-120.

Claerbort, J. F., 1976, Fundamentals of geophysical data processing, Blackwell Scientific, CA, USA.

Dey, A. K., 1999, An analysis of seismic wavelet estimation: M. Sc. thesis, University of Calgary.

Draper, N. R. and Smith, H., 1981, Applied regression analysis: John Wiley & Sons, Inc.

Foster M. S., Nunn, K.R., Lewis, S.A. and Reynolds, D.J., 1997, Zero-phasing seismic data without wells in offshore West Africa: reducing uncertainty and variability of the wavelet: Geophysics, 62, 352-361.

Futterman, W. I., 1962, Dispersive body wave: the Journal of Geophysical Research, 67, 5279-5291.

Ganley, D. C., 1981, A method for calculating synthetic seismograms which include the effects of absorption and dispersion: Geophysics, 46, 1100-1107.

Gibson, B., and Larner. K., 1984, Predictive deconvolution and the zero-phase source: Geophysics, 49, 379-397.

Grossman, J. P., Margrave, G. F., Lamoureux, M. P., and Aggarwata, R., 2002, Constant-Q wavelet estimation via a Gabor spectral model: CSEG 2002 Annual Meeting, Calgary, Alberta.

Hale, D., 1981, An inverse-Q filter: Stanford Exploration Project, 26, 231-243.

Hargreave, N. D., and Calvert, A. J., 1991, Inverse-Q filtering by Fourier transform: Geophysics, 56, 519-527.

Hearn, D. J. and Krebes, E. S., 1990, On computing ray-synthetic seismograms for anelastic media using complex rays, Geophysics, 55, 422-432.

Iliescu, V. and Margrave, G. F., 2002, Amplitude restoration in Gabor deconvolution: CESG 2002 Annual Meeting, Calgary, Alberta.

Kjartansson, E., 1979, Constant Q-wave propagation and attenuation: the Journal of Geophysical Research, 84, 4737-4748.

Krebes, E. S., 1984, On the reflection and transmission of viscoelastic waves, some numerical results, Geophysics, 49, 1374-1380.

Lee, M. W., and Suh, S. Y., 1985, Optimization of one-way wave equations: Geophysics, 50, 1634- 1637.

Leinbach, J., 1996, Wiener spiking deconvolution and minimum-phase wavelets: a tutorial, Deconvolution 2, Geophysics Reprint Series, No. 17.

Lines, L. R. and Ulrych, T. J., 1977, The old and the new in seismic deconvolution and wavelet estimation: Geophysical Prospecting, 25, 512-540.

Margrave, G. F., 1996, qmatrix.m: matlab code, CREWES project.

Margrave, G. F., 1998, Theory of nonstationary linear filtering in the Fourier domain with application to time-variant filtering: Geophysics, 63, 244-259.

Margrave, G. F., 2001, Methods of seismic data processing, Geophysics 657 Course Lecture Notes, University of Calgary.

Margrave, G. F., and Lamoureux, M., P., 2001, Gabor deconvolution, 2001 CREWES Annual Research Report, Calgary, Alberta.

Margrave, G. F. at el, 2003, Gabor deconvolution, extending Wiener's method to nonstationarity: Recorder, Vol. 28, No. 10, 5-12.

O'Connell, R. J. and B, Budiansky, 1978, Measures of dissipation in viscoelastic media: Geophysical Research Letters, 5, 5-8.

Porsani, M. J. and Ursin, B., 1998, Mixed-phase deconvolution: Geophysics, 63, 637-647.

Robinson, E. A., and S. Treitel, 1980, Geophysical signal analysis: Prentice–Hall.

Ross, W.S., and Shah, P.M., 1987, Vertical profile reflectivity: ups over downs: Geophysics, 52, 1149-1151.

Schoepp, A. R. 1998, Improving seismic resolution with nonstationary deconvolution: M.Sc. thesis, University of Calgary.

Schoepp, A. R. and Margrave, G. F., 1998, Improving seismic resolution with nonstationary deconvolution: Improving seismic resolution with nonstationary deconvolution: 68th Annual Internat. Mtg., Soc. Expl. Geophys., Expanded Abstracts, 1096-1099.

Sheriff, R. E., 1991, Encyclopedic dictionary of exploration geophysics: Society of Exploration Geophysicists, Tulsa, Oklahoma.

Sheriff, R. E. and Geldart, L. P., 1982, Data-processing and interpretation, Vol.2. Cambridge University Press.

Smith, G. D., 1978, Numerical solution of partial differential equation: finite difference methods, Oxford: Oxford University Press.

Tonn, R., 1991, The determination of the seismic quality factor Q from VSP data: a comparison of different computational methods: Geophysical Prospecting, 39, 1-27.

Tygel, M. and Bleistein, N., 2000, An introduction to this special section, The Leading Edge, 19, 37.

Wang, Yanghua, 2002, A stable and efficient approach of inverse-Q filtering, Geophysics, 67, 657-663.

Ursin, B., and Arntsen, B., 1985, Computation of zero-offset vertical seismic profiles including geometrical spreading and absorption: Geophysical Prospecting, 33, 72-96.

White, R. E., 1992, The accuracy of estimating Q from seismic data: Geophysics, 57, 1508-1511.

Yilmaz, O., 1987, Seismic Data Processing: Society of Exploration Geophysicists, Tulsa, Oklahoma,

Ziolkowski, A., 1991, Why don't we measure seismic signature? Geophysics, 56,190-201.